

Preferred grain orientation quantification in Mars analogue conditions using wind tunnel experiments

Andreas Zafropoulos

Delft University of Technology

Preferred grain orientation quantification in Mars analogue conditions using wind tunnel experiments

by

Andreas Zafiropoulos

Thesis committee:	Dr. S.J. (Sebastiaan) de Vet	Thesis supervisor
	Dr. S.M. (Stéphanie) Cazaux	Examiner
	Prof. dr. L.L.A. (Bert) Vermeersen	Chair

Cover: Researcher at work in the Aarhus Wind Tunnel Simulator II,
Denmark

Abstract

Saltation is one of the main aeolian transport methods of sand and its physics has been studied extensively both on Mars and Earth. Most studies focused on the particle dynamics of individual particles, the determination of the saltation threshold or on describing the sediment.

This study aims to further research the effect of the aerodynamic environment, specifically the pressure and shear velocity, on the degree of preferred orientation of saltated grains in the sediment. Wind tunnel experiments at various pressures and shear velocities have shown that the fabric strength increases with increasing pressure for higher shear velocities. For lower shear velocities the same is seen at higher pressures, but at low pressures, the fabric strength is increased again. At low pressures impacting grains are thought to induce splashing, randomizing the orientation of grains in the sandbed. This effect is more pronounced at high velocities and low pressures, while at high pressures the airborne streamlining of grains while in flight has a stronger influence at higher velocities, due to the increased air density. In 70% of the experiments, the microscope images of the sediment could be used to determine the wind direction with an accuracy of 10° , if data from multiple images in the same area are combined. Individual images offer less reliable results as small-scale disturbances become more pronounced.

These findings offer a new perspective on the ongoing discussion about saltation on Mars by mapping the effects of pressure and shear velocity. Further experiments at low gravity can offer a more complete understanding of the saltation process on the red planet. In the meantime, the Object Based Image Analysis technique used in this research, offers another method of estimating the wind direction on Mars, based on microscope images taken by the rovers.

Preface

You are reading the thesis "Preferred grain orientation quantification in Mars analogue conditions using wind tunnel experiments". This is a very specific study requiring a broad basis. Planetary sciences meet aerodynamics, sedimentology and image analysis to study individual grains that have been transported by wind. This research was carried out under the supervision of Sebastiaan de Vet as part of the master's program Aerospace Engineering with specialization in Planetary Sciences and Space Exploration at Delft University of Technology.

At the recommendation of professor Stéphanie Cazaux I contacted Sebastiaan in February of 2023 inquiring for a thesis project that had to do with Planetary Sciences and hopefully would have some experimental part attached to it. After a few meetings and discussions Sebastiaan told me he also had a different project that required wind tunnel experiments. Funnily enough I had seen the project pass by a few times on Brightspace but it sounded so exciting that I thought it had already been chosen by a different student. The combination of different fields together with the prospect of conducting experiments really attracted me to this project and I am happy I stuck with it to the end.

I struggle to find the words to describe how intense the journey has been this last year and a half. It was exciting, terrifying, funny, exhausting but above all, worth it. Looking back at how I was in my first year makes me smile. I did not get my BSA and almost had to leave the program. If someone would have told me then how far I'd come, both academically and personally, I don't think I would have believed them. I am immensely proud of my time at TU Delft and of the time I spent on this research project. I hope you will enjoy reading about it, as much as I enjoyed playing with sand.

First and foremost, I would like to thank Sebastiaan, my supervisor, for your endless enthusiasm on the subject provided a boost even in the darkest of times. I really enjoyed our talks and how relaxed we could discuss ideas, findings and conclusions. Throughout the project you really introduced me to the world of research, visiting the VU with me, joining me in Denmark, inviting me to a conference and getting our hands dirty shoveling sand on a specifically cold December morning.

Jon Merrison and Jacob Iversen, thank you for your time, expertise and banter in the basement of the Department of Physics and Astronomy at Aarhus University in Denmark. Our week in Aarhus is one I will never forget. Your hands-on approach and practical thinking saved me from many a blunder and your guidance was very welcome.

I would also like to thank people who supported me here. Martine Hagen and Maarten Prins of the Department of Earth Sciences at the VU in Amsterdam, I am very grateful for your council and for allowing me to use your lab. Cristina Panez and Ron Penners, thank you for helping me through broken sieves and non-functioning ovens to find a way to dry and sieve my sand.

To my friends who have withstood all my moods from ecstasy to desperation: we made it! Thank you for *strijding* with me in Pulse all these months Alex, Hidde, Thomas and Jeroen. I don't know what I would have done without you. Thank you Niv, for being there for me, always reigniting my confidence as well as my delulu.

I would like to thank my family for their support and especially my mother, Olga, who for as long as I can remember has been someone I have looked up to. You are one of the strongest and smartest people I know, and your determination has inspired me to push myself. For a long time, it was just the two of us, but I never really felt like I was missing out on something. Being adult(ish) now I can't imagine how challenging it must have been. Thank you for providing me with endless opportunities and the lovely time we have had together so far.

Lastly, I would like to thank Govert, my boyfriend, for your unwavering support. When we got together you had just graduated so for the longest time our lives have been a bit out of sync. That has not stopped you from being my rock, staying up late with me if I had yet another deadline, hearing my rants and cuddling until all was well again. I do not know how I could have done this without you and thankfully we never have to find out. I love you.

This work was supported by Transnational Access grant 20-EPN2-094 of thesis supervisor S.J. de Vet, which was awarded by the Europlanet 2024 RI that has received funding from the European Union's Horizon 2020 Research Innovation Programme under Grant Agreement No. 871149.

I hope you enjoy reading this thesis.

Andreas Zafiroopoulos
Delft, March 2025

Contents

Abstract	i
Preface	iii
List of Figures	vii
List of Tables	xi
1 Introduction	2
1.1 The effect of saltation on the orientation of particles in the sandbed	2
1.2 Research questions and thesis outline	3
2 Background information	4
2.1 Saltation: A physics and a sedimentology point of view	4
2.1.1 The physics of blown sand	4
2.1.2 Sand grains and their fabric	8
2.1.3 Saltation and preferred orientation	13
2.2 Previous wind tunnel experiments	14
2.2.1 Materials	14
2.2.2 Wind tunnel settings	15
2.2.3 Instrumentation	16
2.3 Image and data analysis methods	18
2.3.1 Object based image analysis	18
2.3.2 Image pre-processing techniques	20
3 Materials and Methods	26
3.1 Material	26
3.1.1 Choice of material	27
3.1.2 Collection of material	29
3.1.3 Preparation of material	30
3.2 Wind tunnel experiments	32
3.2.1 Experimental setup	32
3.2.2 Experimental procedure	32
3.3 Image and data analysis	34
3.3.1 Pre-processing	35
3.3.2 Segmentation and classification	36
3.3.3 Post-processing and data analysis	43
3.3.4 Analysis pipeline	45
4 Results	46
4.1 Grain orientations	47
4.2 The effects of pressure and velocity on fabric strength	50
4.3 Grain shape parameters	51
4.4 Validation of results	52
5 Discussion	54
5.1 The effects of grain elongation on fabric strength	54
5.2 Threshold shear velocity and implications for Mars	55
5.3 The effect of gravity on the threshold shear velocity on Mars	57
5.4 Recommendations for future research	59
6 Conclusion	62

References	64
A Experiments supplementary information	72
B Results settings optimization	74
C Duplicate detections removal procedure	85
D Windroses of each image	87
E Total windroses of each experiment	98
F Box plots of number of grains and fabric strength	100

List of Figures

2.1	From Nickling and McKenna Neuman (2009), Schematic of the different modes of aeolian transport.	5
2.2	From Kok <i>et al.</i> (2012), Schematic of the forces acting on a stationary sand particle resting on a bed of other particles. Forces are denoted by thick arrows, and their moment arms relative to the pivoting point P are indicated by thin arrows. When the moment of the aerodynamic lift and drag forces exceeds that of the gravitational and interparticle forces, the particle will be entrained into the flow by pivoting around P in the indicated direction.	6
2.3	From Bagnold (1941), Variation of the threshold velocity with grain size for air. On the vertical axis the threshold velocity and on the horizontal axis the grain size.	9
2.4	From Boggs (2009), Grain images for estimating the roundness of sedimentary particles (Powers, 1953).	11
2.5	Microscope image of quartz	20
2.6	Microscope image of quartz showing different filters. A: Original image, B: Sharpened image, C: Image smoothed using localized median filter, D: Image opened using structuring disks. Images processed using MATLAB.	21
2.7	Microscope image of quartz Using different contrasts and inverted grayscale values. A: Original image, B: Inverted grayscale, C: Reduced contrast, D: Increased contrast. Images processed using MATLAB.	22
3.1	Microscope image of the sample from Bedaf and the segmented grains.	27
3.2	Grain size distributions of the Bedaf and Texel samples using microscope images.	28
3.3	Grain size distributions of the Bedaf and Texel samples using dynamic image analysis.	28
3.4	The Bedafse Bergen	29
3.5	Sand collection at the Bedafse Bergen.	30
3.6	Mass of sand in each container excluding the mass of the container, before and after drying.	31
3.7	Mass loss at each sand treatment step. The removal of 3295 grams of moisture due to drying and 7000 grams of material due to sieving result in 65020 grams of dry sand.	31
3.8	Schematic views of the experimental setup in the AWTSII-II. A) The test section opened. B) The inside of the narrow insert, showing the microscope setup looking upwind. C) Top view of the wind tunnel showing on the left the fans and on the right the sandbed. The blue arrow indicates the flow direction. D) Side view of the wind tunnel. The blue arrows indicate the flow direction.	33
3.9	View of the sandbed and the lasersheet through the sideways looking webcam. On the left, the sandbed without movement. In the middle, two saltating grains. On the right, permanent saltation. The flow direction is right to left.	34
3.10	Close-up of the two focus stacking methods. On the left using Adobe Photoshop and on the right using Helicon Focus 8. Note the lines on top of the left image and the increased blur on the right of the left image.	36
3.11	<i>The scheme of the PADM algorithm.</i> (Kozakiewicz, 2018)	37
3.12	Overview of the segmentation and classification steps of PADM for medium sized grains. a) Input image f . b) Opening of f , $g_1 = \gamma_{19}(f)$. c) Sharpening of g_1 , $g'_1 = SH_9(g_1)$. d) Binarization of g'_1 , $h = BIN_{otsu}(g'_1)$. e) Markers MS (Note the small white dots). f) Gradient of g'_1 , SF . g) Markers MS with SF contours. h) Segmented image. i) Detected particles.	39
3.13	Comparison of output results of PADM, with on the left the MATLAB implementation and on the right the Python implementation developed for this research.	40
3.14	Number of detected grains for different opening and sharpening radii combinations for medium grains.	42

3.15	Determination of long-axis and corresponding width for a detected sand grain. a. The original grain contour. b. The long-axis in red. c. The grain rotated over the long-axis orientation so the long-axis becomes vertical. d. The width perpendicular to the long-axis in green.	44
3.16	High-level block diagram of the grain detection tool.	45
4.1	Segmented and classified grains from the experiment at ambient pressure and 150% u_{*t} . The blue, red and green colors indicate the large, medium and small grain sizes, respectively.	46
4.2	Windroses for each size class. Note the smaller range for the large and small grains, which was decreased for better visibility. n and R indicate the number of grains and fabric strength, respectively. The red line indicates the preferred orientation.	47
4.3	Grid of windroses of the experiment under ambient pressure at 150% u_{*t} . Each windrose describes the orientations in one image, with the grid corresponding to the physical grid of images taken in the wind tunnel. The red line coincides with the determined preferred orientation. N and R are the number of grains and the fabric strength, respectively.	48
4.4	Windrose of the experiment under ambient pressure at 150% u_{*t} . This figure shows the combined orientations of all 21 measurements. The red line coincides with the determined preferred orientation. N and R are the number of grains and the fabric strength, respectively.	49
4.5	In the top image, the average fabric strength over all images for each experiment, for an elongation of 1.1 and higher. In orange at 120% of the threshold shear velocity and in blue at 150% u_{*t} . In the lower image, box plots of the fabric strength of every image for each experiment, for an elongation of 1.1 and higher. For better readability the box plots are placed next to each other, with the squares indicating the respective average values as seen in top image.	50
4.6	Overview of the particle elongation and equivalent diameter for all detected grains, 143530 in total. The gray cells in the heatmap indicate that no grains were detected. The red dashed lines coincide with the boundaries between the grain size classes, small, medium and large. All grains with an equivalent diameter larger than $390 \mu\text{m}$ were added to the rightmost column and all grains with an elongation greater than 1.6 were added to the top row.	51
4.7	Histogram of detected particle sizes for ImageJ, QICPIC and PADM measurements. The upper and lower boundaries for grain sizes were set at the upper and lower boundaries of PADM to keep the range the same.	52
4.8	Fluid threshold for the sediment at different pressures, along with 120% u_t and 150% u_t	53
5.1	Average fabric strength over all images, for each experiment and for various elongations. The circles indicate 120% of the threshold shear velocity and the squares 150% u_{*t} . The colored areas only serve as a visual aid to highlight the datapoints that belong together. The yellow area corresponds to Figure 4.5.	55
5.2	Box plots of the number of grains and fabric strength of the experiment under ambient pressure at 150% u_* , for 21 images. On the left, in blue, the number of detected grains per lower limit setting for the elongation, and on the right, in orange, the fabric strength.	56
5.3	From Kok <i>et al.</i> (2012), <i>Predictions of the fluid and impact thresholds on Mars</i>	58
5.4	Expected wind speeds on Mars for the different conditions used in the experiment. These wind speeds were determined using real Martian conditions, so a CO_2 atmosphere, basalt as the material and Martian gravity. The left dotted line indicates the smallest particles detectable in this research. The right dotted line indicates the maximum diameter for which the estimated coefficients are definitely valid (Merrison <i>et al.</i> , 2007).	59
5.5	On the left, close-up by the Curiosity Mars Hand Lens Imager, MAHLI, on sol 1241, approximately 400×400 pixels. Note that the grains were passed through a $150 \mu\text{m}$ sieve (The Plantery Society, 2025). On the right, excerpt of wind tunnel image, approximately 1900×1900 pixels.	60

A.1	In white, grid of images taken using the microscope. The images were taken at 2 <i>cm</i> intervals, with the size of each image encompassing approximately 1.1 by 0.8 <i>cm</i> of the sandbed. Top view, the flow direction is right to left. On the left, the imprint left in the sand is that of the sand trap.	73
B.1	Number of detected grains for different opening and sharpening radii combinations for large grains.	75
B.2	Number of detected grains for different opening and sharpening radii combinations for medium grains.	76
B.3	Number of detected grains for different opening and sharpening radii combinations for small grains.	77
B.4	Number of detected grains for different lower and upper thresholds of canny edge detection for large grains.	78
B.5	Number of detected grains for different lower and upper thresholds of canny edge detection for medium grains.	78
B.6	Number of detected grains for different lower and upper thresholds of canny edge detection for small grains.	79
B.7	Number of detected grains for different σ of Gaussian blur and aperture sizes of the Canny edge detection step for large grains.	79
B.8	Number of detected grains for different σ of Gaussian blur and aperture sizes of the Canny edge detection step for medium grains.	79
B.9	Number of detected grains for different σ of Gaussian blur and aperture sizes of the Canny edge detection step for small grains.	80
B.10	Number of detected grains for Binarization thresholds for large grains.	80
B.11	Number of detected grains for Binarization thresholds for medium grains.	80
B.12	Number of detected grains for Binarization thresholds for small grains.	80
B.13	Number of detected grains for different <i>kernel sizes</i> and σ of the Gaussian Filtering step for large grains.	81
B.14	Number of detected grains for different <i>kernel sizes</i> and σ of the Gaussian Filtering step for medium grains.	82
B.15	Number of detected grains for different <i>kernel sizes</i> and σ of the Gaussian Filtering step for small grains.	83
B.16	Number of detected grains for different h-values of the extended maxima step for large grains	84
B.17	Number of detected grains for different h-values of the extended maxima step for medium grains.	84
B.18	Number of detected grains for different h-values of the extended maxima step for small grains	84
C.1	Microscope image of experiment at Mars equivalent pressure (14 mbar) 120% threshold after reaching maximum rippling, row 2, position -3, before removing duplicates	86
C.2	Microscope image of experiment at Mars equivalent pressure (14 mbar) 120% threshold after reaching maximum rippling, row 2, position -3, after removal of 6 duplicates. . . .	86
D.1	Grid of windroses of the experiment at 1000 mbar and at 120% u_{*t} . Each windrose describes the orientations in one image, with the grid corresponding to the physical grid of images taken in the wind tunnel. The red line coincides with the determined preferred orientation. N and R are the number of grains and the fabric strength, respectively. . . .	88
D.2	Grid of windroses of the experiment at 1000 mbar and at 120% u_{*t} . Each windrose describes the orientations in one image, with the grid corresponding to the physical grid of images taken in the wind tunnel. The red line coincides with the determined preferred orientation. N and R are the number of grains and the fabric strength, respectively. . . .	89
D.3	Grid of windroses of the experiment at 720 mbar and 120% u_{*t} . Each windrose describes the orientations in one image, with the grid corresponding to the physical grid of images taken in the wind tunnel. The red line coincides with the determined preferred orientation. N and R are the number of grains and the fabric strength, respectively.	90

D.4	Grid of windroses of the experiment at 720 mbar and 120% u_{*t} . Each windrose describes the orientations in one image, with the grid corresponding to the physical grid of images taken in the wind tunnel. The red line coincides with the determined preferred orientation. N and R are the number of grains and the fabric strength, respectively.	91
D.5	Grid of windroses of the experiment at 480 mbar and 120% u_{*t} . Each windrose describes the orientations in one image, with the grid corresponding to the physical grid of images taken in the wind tunnel. The red line coincides with the determined preferred orientation. N and R are the number of grains and the fabric strength, respectively.	92
D.6	Grid of windroses of the experiment at 480 mbar and 150% u_{*t} . Each windrose describes the orientations in one image, with the grid corresponding to the physical grid of images taken in the wind tunnel. The red line coincides with the determined preferred orientation. N and R are the number of grains and the fabric strength, respectively.	93
D.7	Grid of windroses of the experiment at 240 mbar and at 120% u_{*t} . Each windrose describes the orientations in one image, with the grid corresponding to the physical grid of images taken in the wind tunnel. The red line coincides with the determined preferred orientation. N and R are the number of grains and the fabric strength, respectively. . . .	94
D.8	Grid of windroses of the experiment at 240 mbar and 120% u_{*t} . Each windrose describes the orientations in one image, with the grid corresponding to the physical grid of images taken in the wind tunnel. The red line coincides with the determined preferred orientation. N and R are the number of grains and the fabric strength, respectively.	95
D.9	Grid of windroses of the experiment under Martian pressure at 120% u_{*t} . Each windrose describes the orientations in one image, with the grid corresponding to the physical grid of images taken in the wind tunnel. The red line coincides with the determined preferred orientation. N and R are the number of grains and the fabric strength, respectively. . . .	96
D.10	Grid of windroses of the experiment under Martian pressure at 150% u_{*t} . Each windrose describes the orientations in one image, with the grid corresponding to the physical grid of images taken in the wind tunnel. The red line coincides with the determined preferred orientation. N and R are the number of grains and the fabric strength, respectively. . . .	97
E.1	Windroses of the experiment at 1000 and 720 <i>mbar</i> , combining 21 measurements. The red line coincides with the determined preferred orientation	98
E.2	Windroses of each experiment at 480, 240 and 14 <i>mbar</i> , combining 21 measurements. The red line coincides with the determined preferred orientation	99
F.1	Box plots of the number of grains and fabric strength for each lower limit on grain elongation for the experiments under ambient pressure.	101
F.2	Box plots of the number of grains and fabric strength for each lower limit on grain elongation for the experiments at 720 mbar and one at 480 mbar.	102
F.3	Box plots of the number of grains and fabric strength for each lower limit on grain elongation for the experiments 240 mbar and one at 480 mbar.	103
F.4	Box plots of the number of grains and fabric strength for each lower limit on grain elongation for the experiments at 14 mbar.	104

List of Tables

2.1	Previously conducted experiments on sand transport on Mars. "?" indicates that no information is provided. <i>a</i> : Using a grain size of 100 μm , <i>b</i> : Using a grain size of 200 μm .	14
2.2	Otsu thresholds determined using MATLAB for each part of the cropped image as is and using a smoothing disk or radius 40 pixels. The four cropped images represent quadrants A,B,C and D as seen in the other figures of this section. The threshold for the full image is shown in the right column.	22
2.3	Comparison between different OBIA methods.	23
3.1	Overview of considered materials for the wind tunnel experiments.	26
3.2	Overview of sand container masses prior and after drying, excluding the mass of the container, in grams. For container 12, the mass of the wet sand lower than expected due to an error during the weighing.	30
3.3	Overview of material size caught in each bucket and the vertical structure of the sieves.	31
3.4	Overview of the ten experiments that are part of this research.	35
3.5	Number of detections for different focus stacking settings of Helicon Focus, using the Watershed segmentation method in the MATLAB version of PADM with its default settings.	36
3.6	Grain size classes.	41
3.7	Overview of used settings for the Watershed segmentation method.	41
3.8	Overview of the shape parameters that are the output of the PADM algorithm.	43
3.9	Number of correctly contoured grains by each grain class settings for four images.	43
4.1	Overview of data obtained from Figure 4.1.	47
5.1	Difference between major axis and minor axis in pixels for an ellipse of different elongations and equivalent diameters.	56
5.2	Environmental and material properties on Mars and in the wind tunnel.	57
A.1	Overview of all performed experiments and their settings. "-" indicates it was not performed, "x" indicates that it was performed and "?" indicates that it was not documented.	72
C.1	Determination of correctness for overlapping contours.	85

1

Introduction

When asked to describe sand, most people would think of the sand in the desert or on the beach and focus on the material aspect. However, in the world of sedimentology, sand is a term used to describe material of a certain size, varying roughly from $63\ \mu\text{m}$ to $2\ \text{mm}$ (Wentworth, 1922a). Sand is created when larger entities, such as rocks and boulders, continuously break into smaller parts due to weathering. Most sand on Earth is quartz, or silicon dioxide, but there are also other forms of sand, such as broken sea shells and flint (Bagnold, 1941).

Sand is transported in multiple ways by water and air. Fluvial and aeolian transport are similar in that there is a medium that exerts a force on sand grains, which are moved via rolling, hopping or are suspended in the medium (Nickling & McKenna Neuman, 2009). Saltation is the process during which sand grains hop over the sandbed, often after first rolling and gaining momentum (de Vet, 2013). This hopping movement of sand grains can over time transform flat surfaces into ripples and dunes. On Mars, saltation is responsible for creating large dune formations (Almeida *et al.*, 2008). While saltation has never been directly observed on the red planet, the formation of dunes and ripples, their movement as seen from satellite images and the accumulation of sand on landers and rovers over time, all are indirect observations of saltation (Greeley & Iversen, 1985; Kok *et al.*, 2012). While it has not been determined how saltation takes place in the extremely thin atmosphere, there have been several theories trying to explain the process (Kok, 2010a; Andreotti *et al.*, 2021).

1.1. The effect of saltation on the orientation of particles in the sandbed

Most studies on saltation focus on the determination of the saltation threshold through theory, experiments or computational models (Greeley *et al.*, 1974, 1980; Iversen & White, 1982b; Greeley & Iversen, 1985; Shao & Lu, 2000; Almeida *et al.*, 2008; Kok *et al.*, 2012; Andreotti *et al.*, 2021). Simplified, this refers to the wind speed at a specific air density needed to initiate saltation. These studies try to connect forces and momentum to wind speed, air density and trajectory of individual sand grains, while also taking into account the effects of grains impacting the surface, splashing new grains into saltation (Rice *et al.*, 1995; Beladjine *et al.*, 2007; Ammi *et al.*, 2009; Kok & Renno, 2009). These studies have focused on the movement of a grain and once it settles on the ground the study is usually over.

On the other hand, looking at settled grains one can gain a different perspective. It is known that transport direction can be deduced from, for example, lithified cross-beddings, dunes and ripples. Moreover, on a grain scale level, it has been shown that grain orientation can be used to gain information about the wind direction. On one hand Dapples and Rominger (1945) showed that the long axis of sand grains tends to align itself with the direction of movement during aeolian transport. Rusnak (1957) performed wind tunnel experiments that agreed with this theory. It was confirmed by Schwan (1989) who analyzed thin sections of sandbeds where wind directions were fairly constant over long periods of time and who also performed wind tunnel experiments. de Vet (2013) confirmed this theory again using thin sections of sediment that underwent transportation under known wind direction. Furthermore, the study was expanded to microscope pictures of the sandbed on Mars, where it showed that rolling

about the long axis is a more common occurrence than on Earth. Rolling was also witnessed by Dapples and Rominger (1945), who argued that it was an inherent trait of aeolian transport, more so than in fluvial transport.

While these studies have made a start to understanding the effect of different atmospheric conditions on particle orientation in the sandbed, the information is limited mostly to Earth, with much left unknown for Martian and other low-pressure conditions. This study aims to further the research into preferred orientation of particles by conducting wind tunnel experiments at varying pressures and velocities, and quantifying the preferred orientation using images of the sandbed taken with a microscope, in an attempt to evaluate the effects of pressure and wind speed on the grains in the sandbed.

1.2. Research questions and thesis outline

In order to structure the research and set boundaries, the following research question was formulated:

"To what degree does preferred orientation occur at different air pressures and velocities?"

The following sub-questions can be formed to help answer the main research question:

- What is the influence of pressure and shear velocity on the fabric strength?
- How large is the effect of grain orientation randomization due to impacting grains at different pressures and velocities?
- How well does the preferred orientation align with the wind direction in wind tunnel experiments?

First, background information is presented to introduce the process of saltation and the effects of saltation on the sandbed, along with a brief overview of previously used image analysis tools. Next, the design, preparation and execution of the wind tunnel experiments will be discussed, followed by an overview of the image and data analysis methods. The results and discussion will be presented afterwards. Finally, the conclusions will be given.

2

Background information

After the previous introduction to saltation and sand grains, this chapter presents a summary of relevant literature for this research. The background information aims to highlight gaps in understanding the link between saltation and grain orientation in the sandbed while also exploring potential methods to bridge this knowledge gap.

First, the concepts of saltation and grain orientation in the sandbed will be introduced, covering the physics of saltation, the behavior of sand grains both individually and collectively, and the interactions between them. Next, an overview of similar past experiments will be provided, with a focus on materials, wind tunnel settings, and instrumentation. Finally, different image analysis methods for processing the microscope images taken during the experiments will be compared.

2.1. Saltation: A physics and a sedimentology point of view

Sand can be transported in many ways. The most common are aeolian and fluvial transport. Aeolian transport is named after the Greek god of wind, Aeolus, and refers to different types of sand migration due to wind (Kok *et al.*, 2012). Fluvial transport refers to the flow of water, thus representing movement of sand grains by water, such as a river or a current near the seabed (Ashton *et al.*, 2002)

Saltation is one of the modes of aeolian sand transportation that has been studied extensively. As this project aims to further research into saltation, this will be the principle transport mode that will be expanded upon in this section. First, the physical process of saltation will be introduced to understand the movement of individual grains. Following the physics aspect, a summary of sedimentology will be presented to understand how the individual grains form part of a sandbed. This will highlight the missing link between the two aspects and showcase the need for further research on the intersection of the two fields. Lastly, the knowledge of the two sections will be combined in an attempt to connect the grains of a sandbed to the environmental conditions during transport.

2.1.1. The physics of blown sand

Wind initiates different types of transport depending mostly on the grain size of the sediment. There are four main modes of transport called suspension, saltation, creep and reptation (Bagnold, 1941; Nickling & McKenna Neuman, 2009). The four modes can be seen in Figure 2.1 and will now be further explained in order of increasing grain size.

Suspension occurs when particles are light enough, typically of size below $70 \mu\text{m}$, to be suspended in the air for an extended period of time (Nickling & McKenna Neuman, 2009). The duration of suspension for the particles depends on the settling velocity, which is a function of the particle size, and on the velocity and turbulence of the flow (Tsoar & Pye, 1987). Long term suspension is clearly present on Mars as smaller dust storms occur regularly and larger dust storms annually.

For larger particles, ranging from $70 \mu\text{m}$ up to $500 \mu\text{m}$ grain size, saltation occurs. Saltation refers to the movement of grains through the air for a shorter duration than suspension. It is the predominant mode when it comes to the total mass of sand transport, estimated to contribute up to 95% of the total transport on Earth (Nickling & McKenna Neuman, 2009). Saltation can occur directly due to the forces

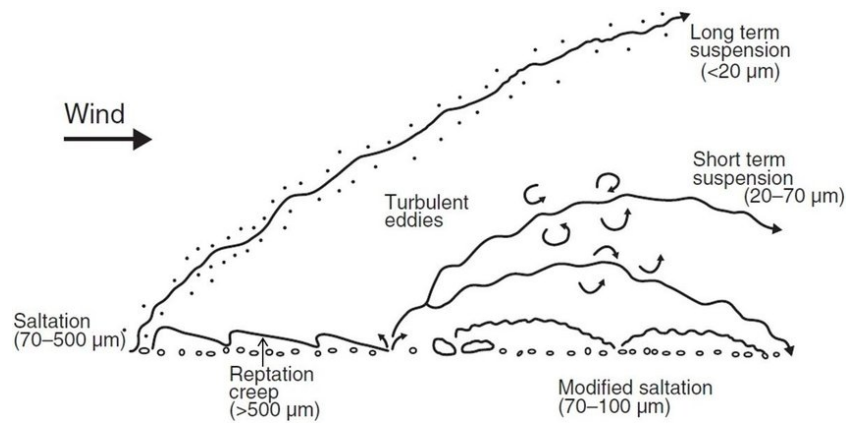


Figure 2.1: From Nickling and McKenna Neuman (2009), Schematic of the different modes of aeolian transport.

of the wind as will be explained in this section but also due to impacts of other particles. It has been found that when grains are already saltating, a lower wind speed is required to make new grains enter saltation. Grains that impact the surface transfer part of their momentum to the grains in the sandbed that, in turn, saltate with the help of the wind (Bagnold, 1937; Anderson & Haff, 1991; Ammi *et al.*, 2009; Kok *et al.*, 2012). If the process of initiation is repeated by impacting particles, sustained saltation is achieved. Saltation on other solid-surface planetary bodies has been studied as well. Particularly saltation on Mars is of interest to better understand the formation of geological features such as dunes.

Particles with diameters generally greater than $500 \mu\text{m}$ experience reptation or creep. The aerodynamic forces are not strong enough to lift these larger grains off the ground for a longer period of time, but are strong enough to induce other types of movement. Reptation refers to grains performing a small jump of usually a few mm , while creep is another term for rolling (Nickling & McKenna Neuman, 2009; Kok *et al.*, 2012).

To understand how saltation takes place, a single grain will be studied before, during and after flight. Sustained saltation will be examined and then the effect of impact of a grain on the surface will be presented. Lastly, saltation in different atmospheres will be compared.

Initiation of saltation

Before entering flight, a grain lies on the bed on top and between other grains. The grain is subjected to forces in its environment, with the forces induced by the medium, the wind, responsible for initiation of motion. This is unless the grain is splashed into the air by a different particle, which will be further explained later on. A force balance model of such a grain in rest is shown in Figure 2.2. First, an overview of the relevant forces will be given, followed by an explanation of the fluid threshold.

The four forces indicated in Figure 2.2 are - starting from the top and going in clockwise direction - the lift force, the drag force, the gravitational force and one of the interparticle forces.

The gravitational force, which is a combination of the pure gravitational acceleration and the buoyancy force is given by Equation 2.1 (Kok *et al.*, 2012). In the equation, the densities of the particle and the medium are given by ρ_p and ρ_a , while D_p denotes the equivalent diameter of the grain. The equivalent diameter is equal to the diameter of a sphere with the same density and volume as the natural grain.

The drag force on a grain is given by Equation 2.2, where K_d is a dimensionless coefficient and u_* is the shear velocity (Greeley & Iversen, 1985). The shear velocity is defined as shown in Equation 2.3 (Bagnold, 1941) and is proportional to the vertical change in velocity parallel to the surface (F. White, 2006). In the equation, τ represents the wind shear stress on the grain. The shear velocity can be determined using Equation 2.4, where u is the free-flowing velocity of the wind, k is the height above the sandbed and z is the roughness of the sandbed. The roughness parameter z depends on the size of the particles. Using these equations, the drag on a grain can be determined both while in rest and while

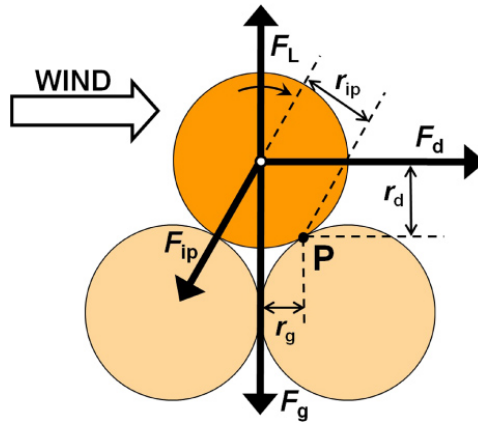


Figure 2.2: From Kok *et al.* (2012), Schematic of the forces acting on a stationary sand particle resting on a bed of other particles. Forces are denoted by thick arrows, and their moment arms relative to the pivoting point P are indicated by thin arrows. When the moment of the aerodynamic lift and drag forces exceeds that of the gravitational and interparticle forces, the particle will be entrained into the flow by pivoting around P in the indicated direction.

in flight. The last equation also illustrates that there is a gradient in the wind speed, with lower wind speeds occurring very near the surface.

The interparticle forces are a combination of all the forces particles exert on each other. These can be van der Waals and normal forces (Castellanos, 2005), but also electrostatic forces (Zheng *et al.*, 2006). Van der Waals forces and normal forces depend on the material properties and the grain sizes while electrostatic forces depend on the differences in charges of neighboring particles. Lastly, humidity can also introduce interparticle forces (Nickling & McKenna Neuman, 2009).

$$F_g = \frac{\pi}{6} (\rho_p - \rho_a) g D_p^3 \quad (2.1)$$

$$F_d = K_d \rho_a D_p^2 u_*^2 \quad (2.2)$$

$$u_* = \sqrt{\frac{\tau}{\rho_a}} \quad (2.3)$$

$$u = 5.75 u_* \ln \frac{z}{k} \quad (2.4)$$

A slightly different model is used by Merrison *et al.* (2007). Instead of only taking into account the drag force, in their description a torque is added by multiplying the drag force by a value depending on the diameter of the particle. This torque is an effect of the vertical gradient of horizontal velocity of the medium, which, in the previous model, affected the lift force. In the second model, the velocity gradient results in a larger drag force exerted on the part of the grain furthest from the sandbed, resulting in a moment trying to induce rolling (Merrison *et al.*, 2007). Clearly, in both models the vertical velocity gradient introduces a positive effect on motion. In the first model, the effect is upwards and in the second model it is horizontal in the direction of the flow of the medium. However, in both cases, if one were to use Figure 2.2 as a reference, the effect would introduce a clockwise moment around the pivoting point P.

When the moment of the aerodynamic forces exceeds the moment created by the interparticle and gravitational forces as seen in Figure 2.2, the grain will rotate around point P and will either roll over the grain or, if the aerodynamic forces are great enough, be expelled into the air to saltate. When the shear velocity is high enough to initiate such movement, the so called fluid threshold has been surpassed (Bagnold, 1941).

Looking at a more simplified force balance model than pictured in Figure 2.2 if one were to neglect the lift and interparticle forces, the moment generated by the drag force would have to overcome the moment generated by the combined gravity and buoyancy forces. Assuming the angle between the

downwards force and the vector from the center of the grain to the pivoting point P is α° , the moments created by the two forces are shown in Equation 2.5 and Equation 2.6.

$$M_g = \frac{\pi}{6} (\rho_p - \rho_a) g D_p^3 \cdot \sin(\alpha) \quad (2.5)$$

$$M_d = K_d \rho_a D_p^2 u_*^2 \cdot \cos(\alpha) \quad (2.6)$$

$$u_{*t} = A_{*t} \sqrt{\frac{\rho_p - \rho_a}{\rho_a} g D_p} \quad (2.7)$$

Equating the two moments and reorganizing leads to an expression for the shear velocity required to initiate saltation, as can be seen in Equation 2.7. The wind speed of the medium can then be determined using Equation 2.4. This expression then depends on a number of factors. Environmental factors such as the density of the air, the gravitational acceleration and partly the coefficient K_d , which is included in the constant A_{*t} play a role but also material and structural factors such as the density, size and shape of the grain influence the fluid threshold speed, further denoted as u_{*t} . The fluid threshold is the shear velocity at which saltation starts occurring. Different values have been determined for the constant A_{*t} , with the simplest being 0.10 if indeed the interparticle and lift forces are neglected and if the Reynolds number of the flow is not taken into account (Bagnold, 1941). However, other expressions exist which are also based on wind tunnel experiments (Iversen & White, 1982a; Shao & Lu, 2000).

While the fluid threshold is a nice method to indicate at which wind speeds saltation occurs, it is not indicative of when movement is initiated. Below the threshold grains start to vibrate. Furthermore, grains that are more exposed to the medium will be subject to more drag and will saltate earlier than more imbricated grains (Nickling, 1988). As the wind speed from well below the fluid threshold increases and nears it, grains start to vibrate and rolling may occur. Individual, more exposed grains, may start saltating. The rolling grains can gain enough momentum themselves to start saltating. All these processes can happen below the fluid threshold has been surpassed (Nickling, 1988; Merrison *et al.*, 2007). However, the fluid threshold is still a well established method to indicate the required conditions for the initiation of saltation.

Once the fluid threshold is surpassed, the sand grain enters an almost ballistic flight. Trajectories of grains have been determined using simulations (Kok & Renno, 2009). Impacts of grains and the splashing of new grains have also been simulated. Grains that enter flight are assumed to instantaneously align their principal axis with the direction of the flow (Schwan, 1989).

Grains that saltate can experience an increase in momentum due to the wind speed, resulting in a higher impact velocity than the speed at which the grain left the sandbed. If the momentum becomes high enough, when the grain impacts the surface it can hop into a new saltation arc or splash new grains into saltation arcs (Bagnold, 1941; Pähtz *et al.*, 2020). It is possible that a grain experiences several hops with increases in momentum, based on the wind speed, local turbulent effects, the impact angle and the sandbed itself.

Ammi *et al.* (2009) deduced that for incidence angles between 10° and 90° the number of ejected particles depends on the kinetic energy of the impacting grain and the ejected grains. An expression for the number of ejected particles based on the impact speed is given below in Equation 2.8

$$\overline{N_e} = n_0 \left(1 - \bar{e}^2\right) \left(\frac{v_i}{\zeta \sqrt{gd}} - 1\right) \quad (2.8)$$

A different expression has been developed by (Kok & Renno, 2009), shown in Equation 2.9, based on numerical simulations and using conservation of momentum, with a a proportionality constant.

$$N = a \frac{m_{imp} v_{imp}}{m_{spl} \sqrt{gD}} \quad (2.9)$$

Both Ammi *et al.* (2009) and Beladjine *et al.* (2007) determined that the distribution of the horizontal velocity of ejected particles follows a normal distribution. In the downwind direction, the median is slightly positive, indicating that most movement happens in the downwind direction. In the transverse direction, the median is near zero, indicating that the sideways distribution of grains is equal on both sides.

The impact threshold, or dynamic threshold, the shear velocity for saltation to take place due to impacting particles, is lower than the fluid threshold required to initiate saltation. The value is around 80% of the fluid threshold for particles in ambient earth atmosphere (Bagnold, 1937). However, on Mars it is estimated that the dynamic threshold is much lower. Some estimates place it as low as 10% of the fluid threshold (Kok, 2010a; Kok *et al.*, 2012), while others place it near 45% (Almeida *et al.*, 2008). This lower impact threshold allows for saltation to continue even if the wind shear velocity drops below the fluid threshold after saltation has been initiated. It is assumed that the transfer of momentum to the grains in the sandbed to initiate new saltation is done mostly by impacting sand grains and less by the wind itself (Bagnold, 1937; Anderson & Haff, 1991).

Saltation on Mars

Besides on Earth, saltation occurs on other solid-surface planetary bodies as well. The process is thought to occur on Venus, Mars and Titan (Greeley & Iversen, 1985; Kok *et al.*, 2012). While the conditions for Earth have been well established, particularly on Mars questions remain about how saltation takes place.

The largest problem is that the fluid threshold does not seem to be reached as wind speeds and air pressure are very low. The process of saltation has never been directly observed, but the effect of aeolian transport of sand has. For example, ripples and dunes are formed and landers and rovers on the surface have detected changes in the coverage of sand on their parts by taking selfies (Almeida *et al.*, 2008; Charalambous *et al.*, 2021; Baker *et al.*, 2022).

While it was believed that wind speeds do not acquire enough speed to initiate saltation on Mars, Baker *et al.* (2022) believes that a combination of faulty theories, assumptions and methods led to this belief. First, the assumption that no saltation can occur below the fluid threshold is an assumption that may not be entirely correct as shown by Merrison *et al.* (2007) and Nickling (1988). Below the fluid threshold, movement is possible in the form of rolling and reptation. As mentioned before, the medium transfers momentum to moving grains. This can lead to saltation below the fluid threshold as it is currently defined. Moreover, the laminar layer close to the sandbed is estimated to be five times thicker than on Earth. This layer is formed due to viscous forces and it is large enough to fully cover grains on the surface, prohibiting the turbulent effects from initiating direct saltation (F. White, 2006; Kok *et al.*, 2012). This enhances the belief that saltation on Mars occurs more often by rolling grains than by the wind directly. Sullivan and Kok (2017) agree with this in a way, stating that climate models used to simulate the wind speed were too coarse to capture the small scale effects that might be at play. Furthermore, they argued that there might be much larger surface relief and that grains likely move sporadically while the friction velocity is under the fluid threshold, initiating saltation with their impacts. Apart from this, while the fluid and impact threshold are generally accepted as the lower bound of when saltation can occur, their relationship to the sand flux is not well understood (Andreotti *et al.*, 2021). More importantly, the connection of experimentally determined fluid and impact thresholds to naturally occurring aeolian processes is not well explored either. It may be easier to achieve saltation in nature than in wind tunnels due to boundary layers of higher thickness (Päntz *et al.*, 2018; Cameron *et al.*, 2020).

While indeed it is theorized that saltation occurs more rarely on Mars than on Earth, due to the much lower gravity, grains are thought to achieve much higher saltation arcs (Almeida *et al.*, 2008). The increased height results in more time in the medium resulting in greater acceleration of the grains. This in turn, results in a smaller impact threshold, even as low as 10% of the fluid threshold, as mentioned before, compared to the 80% that has been found on Earth (Kok, 2010a). Thus, while in theory it may be more difficult to initiate saltation solely by wind, once grains start impacting the surface, it is easier to sustain saltation.

2.1.2. Sand grains and their fabric

Sedimentology refers to the study of sedimentary rocks and the processes of their formation, rocks formed by lithification and dunes. Sedimentary rocks are rocks that are formed by accretion or deposition of material (Wolff & Benedict, 1964). There are four types of sedimentary rocks. Siliclastic rocks consist mostly of silicates such as quartz. Examples in this category are sand and clay. Carbonate rocks contain carbon, for example calcium carbonate or dolomite. Evaporites are minerals that are left after evaporation of water such as gypsum and halite. Then there are other chemical and biochemical sedimentary rocks that do not fall in these categories (Boggs, 2009). Quartz sand, which will be used in the experiments belongs to the first category, the siliclastic rocks.

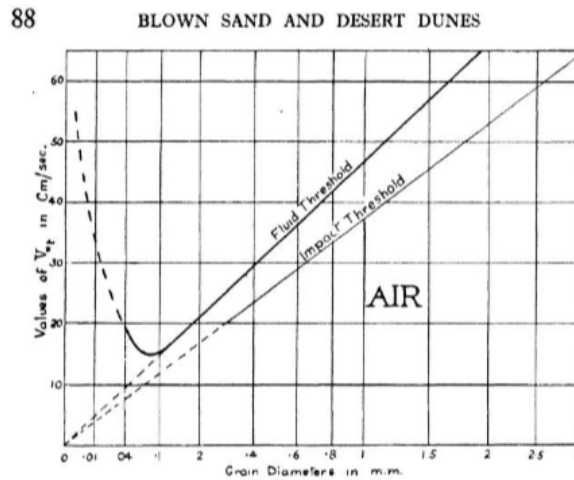


Figure 2.3: From Bagnold (1941), Variation of the threshold velocity with grain size for air. On the vertical axis the threshold velocity and on the horizontal axis the grain size.

While sedimentology is a well evolved field of science, this subsection aims to provide a summary necessary to understand the influence of moving particles on a sandbed. If a more in-depth understanding of sedimentology is desired, books such as Boggs (2009) and Carver (1971) can provide a deeper understanding. To that end, first grain sizes will be described, followed by grain-forms. Lastly, the overarching concept of fabric will be introduced focusing mostly on the determination of grain orientations in the fabric.

Grain size

The size of grains is the most common method to describe a sediment and it influences how the sediment behaves in multiple ways. For example, the size distribution of an aggregate, a collection of sedimentary material, has influence on the porosity and permeability of the sediment. Moreover, grain size is an important parameter of sediment transport. Figure 2.3 shows the relationship between grain size, and the fluid threshold and the impact threshold. For the fluid threshold it can be seen that larger grain sizes require a higher shear velocity, since the mass of an object increases at a higher rate than its effective surface area, per Equation 2.1 and Equation 2.2. However, when the grain size reduces below a certain point, interparticle forces and the effect of the viscous layer near the surface dominate the drag force, thus increasing the threshold again (Bagnold, 1941).

It is believed by some that grain size holds information about the depositional environment (Boggs, 2009). However, others have often failed to use this property to correctly deduce the environmental conditions (Jordan *et al.*, 1981). Instead, the size of grains has been used for other goals such as to interpret coastal stratigraphy, trace glacial sediment transport and understand seafloor sediment better (Syvitski, 1991).

Naturally occurring particles range in size from clay to boulders. The main categories according to the Udden-Wentworth grain-size scale are mud, consisting of clay and silt, sand and gravel, increasing with size. Wentworth (1922a) compared previous methods of classification and proposed their own method, which has been widely used ever since.

The standardization this scale provides has been used, among others, for the development of standard sieve meshes, the Tyler Standard Sieves, and for a uniform method of referencing grain sizes (Tyler, 1967; Carver, 1971; Boggs, 2009).

Different methods exist to determine the size of grains. For loose sediment, manually measuring the diameter can be of use for large particles such as boulders or cobbles. For sand-sized grains, sieving, settling-tube analysis and different image analysis methods can be of use. For lithified sedimentary rocks, thin-sections can be made and image analysis can be used to determine the grain size.

Sieving is a straightforward method where material is passed through a sieve with known size. The result is a collection of grains smaller than the size of the holes in the sieve. Depending on the purpose of the sieving, the material can be prepared. Methods for removal of unwanted particles such

as carbonates and organics are presented by Carver (1971). In order for the material to be sievable, it usually needs to be dried so the individual grains do not stick together. A settling tube can also be used to determine the grain size by measuring the fall time of particles through water (Carver, 1971).

Grain shape

There are three grain-form parameters. Most authors agree that shape or form and roundness are two of them. However, some see pivotability, the degree of rolling (fast to slow indicating round to tabular shapes) that a grain undergoes on a slope (Carver, 1971), and some see surface texture as the third parameter (Boggs, 2009). Carver (1971) does not take into account surface texture, while Boggs (2009) neglects pivotability. In this review the pivotability will be included in the shape section and surface texture will be briefly highlighted as the third parameter. This way the parameters are going from larger to smaller scale.

Shape refers to the global form of the grain. Qualitatively a grain can be spherical, elliptical, irregular and multiple other shapes. Quantitatively a grain shape can be expressed in terms of sphericity, flatness ratio, roundness ratio and elongation index (Barrett, 1980; Illenberger, 1991). The shape of grains has influence on the transport rate of sand (G. Williams, 1964; Willetts *et al.*, 1982).

The sphericity was introduced by Wadell (1932) using the surface area and volume of a grain. As these are difficult to measure, a number of different expressions for the sphericity were developed. Wadell (1935) introduced the Wadell's working sphericity, Krumbein (1941) the Krumbein's Intercept Sphericity and Sneed and Folk (1958) the maximum projection sphericity. The first method uses a projection of the area of the grain while the latter two determine the three principal axes of a grain and use their sizes to determine the sphericity. Zingg (1935) introduced a method similar to sphericity to classify the shape of grains, also based on the ratio of the smaller two axes a grain to the largest axis. The categories are disk, spheroid, blade and prolate, also called a roller. Later two more categories were added, the planar and acicular shapes (Brewer, 1965). Illenberger (1991) introduced the Corey shape index, also based on the ratio between the axes of a grain, as a measure for the sphericity.

When only two-dimensional data is available, for example in thin sections or photographs, (Riley, 1953) deduced a method based on the ratio of the diameters of the largest possible circle that can be drawn inside the grain's contour and the smallest possible circle drawn outside the grain's contour.

The roundness and flatness ratios are different methods of describing the shape of a grain based on the length, breadth and thickness of a particle. They are simpler expressions than the ones used for the sphericity (Wentworth, 1922b). Expressions for the elongation index and the oblateness depend on the ratio between the greatest width and greatest length measurable for a particle (Carver, 1971).

Pivotability is a parameter introduced by Shepard *et al.* (1961). It is the measure of rolling that a grain undergoes while moving down a slope due to gravity. The pivotability is determined based on the velocity of the grain (Glezen & Ludwick, 1963).

Lastly, and most importantly for this research, elongation refers to ratio of the length of a grain to its width. Multiple slightly different expressions exist, but in this case the elongation is defined as the long-axis, the longest possible line that can be drawn through the grain, divided by the width, the widest possible measurement perpendicular to the long-axis. An overview of how this was computed for this research is shown later in Figure 3.15.

Roundness describes the degree of sharpness of corners on the surface of the grain. The parameter is measured in two dimensions, so different angles of observation may lead to different results.

Qualitatively, the roundness can be determined visually and classified from very angular to well rounded (Russell & Taylor, 1937; Powers, 1953; Schneiderhöhn, 1954). Quantitatively, the roundness of a grain depends on the curvature radius of each individual corner in a particle compared to the radius of the largest possible circle that can be drawn inside the boundaries of the grain (Wadell, 1933). As it is difficult to determine the curvature radii of each corner of every grain manually, Fourier techniques to analyze the roundness have been introduced by Diepenbroek *et al.* (1992), who also summarizes all definition of roundness. The Fourier technique recreates the shape of the particle using a series of harmonic expressions for the radii of the grain.

The concept of surface texture will very briefly be touched upon as it is a scale too small for this research. The surface texture of grains can help identify the environment that the particle is found in based on a large number of microfeatures. Studying the surface of the particle can lead to information

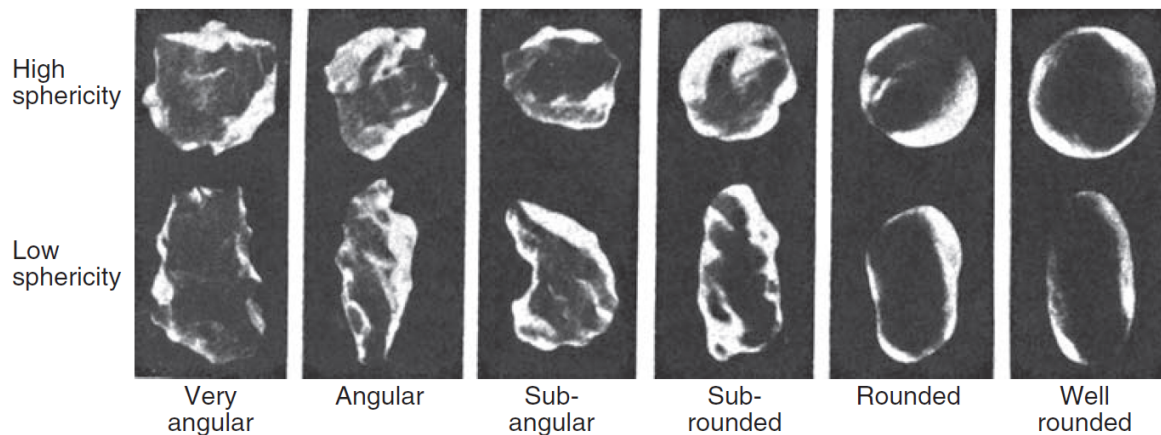


Figure 2.4: From Boggs (2009), Grain images for estimating the roundness of sedimentary particles (Powers, 1953).

that Fourier analysis is too coarse to determine. As quartz grains keep markings on the surface for a long period, it can be possible to determine the environments that grains have experienced in the past (Boggs, 2009).

While much research has been performed into the determination of different parameters that describe the shape of a grain, Boggs (2009) argues that the parameters do not offer reliable information on the transport history of clastic sediment, due to the many other variables that play a role in the process. Moreover, the existing methods to determine the form of grains are subject to observational bias and it is difficult to clearly determine the axes of each grain (Barrett, 1980).

The Fourier analysis method is much more reliable to determine the shape of a particle. However, the resulting data is in the form of amplitudes instead of an actual representation of the parameters of a grain. This makes the comparison between different grains difficult (Boggs, 2009).

The shape of a particle does play a role in the settling speed of particles. Furthermore, the shape is of great importance to the ability of the grain to be transported, as is described by Carver (1971) as pivotability. Both found that rounder shapes such as rollers are transported with greater ease than flatter shapes such as disks (Swanson, 1972; Mazzullo *et al.*, 1992).

While there have been attempts to correlate the grain shape with the grain size, there is no clear general relationship. However, it may be possible to find relationships within a specific population. This can enable the researcher to pick a certain range of grain sizes by sieving that have the desired shape (Das & Ashmawy, 2007).

Fabric

While the grain size and grain form parameters describe individual grains, fabric applies to a collection of grains, called an aggregate. The fabric describes the way an aggregate looks and how grains in an aggregate are positioned relative to each other (Boggs, 2009). It is expressed in two ways, the packing and the orientation. Packing refers to the way that grains are arranged and spaced in the sediment and depends on the shape and size of the particles as well as the physical and chemical processes in the bed after deposition (Bates & Jackson, 1980). Packing is quantitatively described by the contact index and tight packing index, referring to the average number of particles each grain is touching and the average number of long, concavo-convex and sutured contacts each grain has, respectively. Grain orientation, on the other hand, mostly depends on the processes during deposition, but can be altered after deposition (Dapples & Rominger, 1945; Rusnak, 1957; Schwan, 1989; Boggs, 2009; de Vet, 2013).

Grain orientation is usually defined as the angle between the longest axis of a particle and the direction of the flow of a depositional medium or a datum in the plane parallel to the bed, so it is a measurement of the two dimensional projection of the particle onto the sandbed. Rusnak (1957) determined that the orientation depends mostly on elongation of particles, velocity of fluid flow,

distribution of eddies in fluid flow, roughness of the bottom, individual eddies due to adjacent particles, packing of the adjacent particles, rate of sediment supply. However, the grain orientation is also thought of as a textural property of the sediment (Pettijohn, 1942).

Experiments have shown that grains moving through a fluid acquire a preferred orientation with the ab-plane parallel to the direction of the flow (Krumbein, 1942; Dapples & Rominger, 1945; Davies, 1947; Kunkel, 1948; McNown & Malaika, 1950; Rusnak, 1957). More elongated grains tended to align better with the direction of the flow than the other particles and the orientation of deposited grains can be used to determine the flow direction of a fluid (Dapples & Rominger, 1945; Rusnak, 1957). Forces of the fluid on the grains may influence particle orientation or induce movement such as rolling and pivoting (Hunzicher, 1930; Lane & Carlson, 1954).

Dapples and Rominger (1945) described three methods for the determination of the direction of an individual particle; the long-dimension elongation, least-projection elongation and center-of-area elongation. The three methods are described below:

1. Long-dimension elongation uses the orientation of the longest line, or the long-axis, one can draw through a grain. It is easy to determine but for irregularly shaped grains this method may not yield the best result.
2. For the least-projection elongation two parallel lines are drawn tangent to the surface on opposite sides of the grain. The lines are drawn with the smallest possible distance between them. The direction of the perpendicular lines is the orientation of the grain.
3. For the center-of-area elongation method, the longest possible line is drawn through the center of the area of the particle. It is the most theoretically sound method since it lies near the center of mass but it may be difficult to determine the center of the area, especially for grains with irregular shapes.

Methods 1 to 3 increase in scientific soundness but also in complexity. In their experiments Dapples and Rominger (1945) used least-projection elongation since long-dimension elongation does not result in a good determination of the end position, the side of the grain along the long-axis that is largest, while least-projection elongation does. Center-of-area elongation was not examined as least-projection elongation provided adequate results.

For the experiments conducted in an aeolian environment grains moved directly in place and others saltated and rolled. A greater standard deviation and smaller kurtosis than in fluvial environment was discovered so a lesser degree of preferred orientation was found. A secondary mode of orientation was identified almost perpendicular to the primary mode and is probably due to rolling, this can be used to see the difference between aeolian and fluvial environments. About 55% of the grains had their larger ends towards the source as was expected, which is quite a low percentage to reliably determine the direction of flow between two possibilities (Dapples & Rominger, 1945).

Once the individual grain orientations are determined, statistical methods can be implemented to determine the orientation of the overall fabric also called the central tendency. In order to measure the preferred orientation of sand grains on the sandbed, a metric called fabric strength is used (Schwan, 1989; de Vet, 2013). To indicate how much preferred orientation occurs in a sample, the mean resultant length is used, which has a value between 0 and 1, with higher values indicating a larger amount of preferred orientation. Two similar but slightly different methods are implemented by Carver (1971) and Schwan (1989) to determine the resultant grain orientation in a population. In both cases i intervals are created of the same width in degrees. The central tendency is determined using the ratio of the sums of the number of particles in each segment multiplied by the sine or cosine of the median angle of that segment. In the case of Schwan (1989), the median of the segment is multiplied by two. Schwan (1989) uses a larger number of smaller intervals of 10° , while Carver (1971) uses intervals of 30° . Schwan (1989) also only use intervals from 0 to 180 degrees, since they consider the line on which the preferred orientation lies, which can be $\pm 180^\circ$. Lastly, the definition of the fabric strength differs from one method to the other. Carver (1971) did not directly call it fabric strength, but rather the consistency factor, estimated by dividing the resultant vector of all grains by the total number of particles.

Since Schwan's method has been successfully used in the past for aeolian environments, while Carver's method has been mostly used for glacial environments, the Schwan method will be used

going forward. Therefore, this method will be briefly explained more extensively. As mentioned before, the fabric strength uses the unit mean resultant length R , which is described in the set of equations below (Equation 2.10, Equation 2.11 and Equation 2.12). Sections of 10° are made and each long-axis of a particle is classified under one of the sections. The angle α_i is the angle from the North-facing line to the middle of the i -th section, clockwise positive. Variable f_i is the number of grains whose long-axis direction is in the i -th section. Then, the direction of preferred orientation lies along the line oriented in the direction given by Equation 2.13.

$$R = \sqrt{\left(\frac{C}{n}\right)^2 + \left(\frac{S}{n}\right)^2} \quad (2.10)$$

$$C = \sum_{i=1}^{18} f_i \cos(2\alpha_i) \quad (2.11)$$

$$S = \sum_{i=1}^{18} f_i \sin(2\alpha_i) \quad (2.12)$$

$$\bar{x} = 0.5 \tan^{-1}(S/C) + K \cdot 90^\circ, \text{ with } K = 0 \text{ or } 1 \quad (2.13)$$

The fabric of a sandbed can yield information about current and previous depositional directions. Division of grain orientations in segments enables the creation of rose diagrams, as was done by de Vet (2013). While indeed it was shown by multiple researchers that the preferred orientation can be used to determine the wind direction during deposition (Dapples & Rominger, 1945; Schwan, 1989; de Vet, 2013), if the wind direction is known the preferred orientation of the sediment can illustrate the effect of orientation randomization due to the impacts of saltating grains.

2.1.3. Saltation and preferred orientation

Now that the physical process of a saltating grain and an introduction to sedimentology have been introduced, it is the goal to bring these two together and understand how saltation affects the orientation of grains in the sandbed.

Saltation is initiated when the fluid threshold or impact threshold is exceeded, either directly by the wind or due to other particles that impact the surface and eject other particles into saltation. The grains, while in flight, are assumed to instantaneously align their principal axis with the direction of motion and gain momentum from the wind. After a short trajectory they impact the surface with increased momentum and may rebound or eject new grains. If this process becomes continuous, this is called sustained saltation. While the trajectories of ejected and rebounding grains can be approximated numerically, it is difficult to model the effect on the orientation of all the particles that make up the sandbed.

The orientation of the grains in the bed depends on a great number of parameters such as roughness of the bed and packing of adjacent particles. However, the orientation also depends on the elongation of the particles and the velocity of the fluid flow. Methods have been developed to estimate the direction of the medium based on the orientation of sand grain in the sand bed. The degree of which elongated sand grains align themselves with the direction of the wind is expressed as the fabric strength. It is a measure of preferred grain orientation.

While it is known from both fields that indeed particles orient their principal axis along the direction of the medium, both in flight but also when deposited in the sandbed, it is unclear how impacting grains influence the orientations on the sandbed, especially at high impact energies such as are expected on Mars.

Further research could focus on determining the influence of impacting grains in the sandbed on the orientation of particles in the bed. In other words, to what degree does an impacting grain introduce randomness of particle orientation of the particles that already lay in the bed. This would help understand the randomization of particle orientation in unidirectionally aeolian deposited sediments. Furthermore, it would provide an estimate of the reliability of the method used to determine the orientation of the medium based on the orientation of particles on the bed. Performing this research for Martian environment may enable the use of these methods with data acquired from landers and rovers on the surface of Mars. This could introduce new information in the debate about how it is possible that saltation takes place on Mars under conditions assumed to be below the fluid threshold.

2.2. Previous wind tunnel experiments

With the concepts of saltation and preferred orientation introduced, the next step is to investigate how similar studies have been conducted. Specifically, similar wind tunnel experiments were studied, in order to determine the type of material, wind tunnel settings and required instruments.

Numerous experiments to study sand transport have been performed in the past century, starting with research performed by Bagnold (1941) on processes on Earth. After the first data of Viking 1 and Viking 2 were acquired in the seventies, studies aiming to quantify the fluid threshold for saltation expanded to Mars (Greeley *et al.*, 1976; B. White, 1979; Iversen & White, 1982b). While the experiments on Earth were conducted using sand, for the experiments studying saltation on Mars other, lower density, materials were sometimes used. An overview of some of the conducted experiments is given in Table 2.1. The overview was selected giving priority to simulations using sand, so some using other materials were excluded, such as Swann *et al.* (2020). The experiments will be further highlighted in the chapter when discussing different materials, settings and measurement methods.

Table 2.1: Previously conducted experiments on sand transport on Mars. “?” indicates that no information is provided. *a*: Using a grain size of 100 μm , *b*: Using a grain size of 200 μm .

Source	Material	d_p [μm]	ρ_p [kg/m^3]	Gas	P_a [Pa]	ρ_a [kg/m^3]	u_* [m/s]
Greeley (2002)	Sand (silica)	100	2400-3000	air	Ambient	?	?
		100			10		?
		200			Ambient		2.4
		500			10		3.0
Merrison <i>et al.</i> (2007)	Glass spheres	25 to 220	2700	air	30	0.035	2.06 to 2.50
			600				?
			150				?
de Vet <i>et al.</i> (2014)	Volcanic glass	<63 to 300	2330	air	250	0.3	0.85
					500	0.6	0.65
					920	1.1	0.45
					1000	1.2	0.40
Andreotti <i>et al.</i> (2021)	Sand	125	2640	air	13.8	0.0166	1.9
Greeley <i>et al.</i> (1976)	Walnut shells	20-700	1100	air	5.3	?	4
					6.5		3.2
					7.9		2.7
					10.5		2.3 $d_p = 100 \mu\text{m}$
Greeley <i>et al.</i> (1980)	Walnut shells	23-800	1100	CO ₂	5	?	2.0 ^a
					10		1.5 ^a
					20		1.0 ^a
					50		0.6 ^a
					5		2.7 ^b
					10		1.9 ^b
20	1.2 ^b						
50	0.8 ^b						
Iversen and White (1982b)	Sand	154	2650	air	580-101300	0.007-1.213	?
B. White (1979)	Glass spheres	208	2000-3000	air	23	0.086	?

This section aims to give an overview of previously performed experiments and studies that are relevant to understand the limitations, options and opportunities of experimentally determining the preferred orientation of grains in a sandbed. The focus will lie on experiments concerning saltation on Mars, but if there is insufficient information available, other studies on saltation or the martian atmosphere and surface will be explored. Furthermore, a brief comparison between the previously used environments and instruments, and the available settings and equipment will be given.

2.2.1. Materials

In previous aeolian transport experiments aimed to simulate Martian conditions, a number of different materials have been used depending on the needs and available resources of the research. Substitutes can be chosen depending either on their physical or geochemical properties (de Vet *et al.*, 2014). In this case, the physical properties are of interest, so characterizing shape, density and grain size are of great

importance.

The composition of the martian surface is a mixture that depends on the location on the planet. The dune fields in the northern hemisphere, for example, consist of volcanic glass (de Vet *et al.*, 2014). Generally, the surface consists primarily of silicates, such as olivine pyroxene and plagioclase but also feldspars phyllosilicates. Iron oxides and specifically haematite on the surface give the planet its red color. Less abundant minerals include sulfur and sulfates, and carbonates (Chevrier & Mathé, 2007). Densities ranging from 2900 to 3570 kg/m^3 were estimated with larger densities for larger grains in Meridiani Planum (Kozakiewicz *et al.*, 2023). Often values between 2700 and 3000 kg/m^3 are used (Greeley *et al.*, 1976; Andreotti *et al.*, 2021).

Grain sizes on Mars have been determined visually using microscopic images. In the aeolian environment of Gale Crater, larger ripples tend to consist of relatively larger sand grains than smaller ripples, with the larger ripples consisting of grains with sizes 200 to 500 μm , the medium ripples of 100 to 300 μm and the small ripples of 80 to 300 μm (Gough *et al.*, 2021). Other studies of the images taken near the Bagnold Dunes report grain sizes varying from 50 to 350 μm with an average grain size of 103 μm (Ewing *et al.*, 2017) but the volumetrically largest group has sizes from 50 to 150 μm (Weitz *et al.*, 2018). A study summarizing results of multiple studies of the Namib dune at the edge of Gale Crater found that grain sizes ranged from 50 to 350 μm with the most 125 μm being the most common size. The elongation of grains at Gale Crater (defined as "aspect ratio") varies from 1.10 to 1.25. For the samples with median grain size between 100 and 200 μm , the median elongation is 1.20 (Weitz *et al.*, 2018).

Kozakiewicz *et al.* (2023) analyzed images from Meridiani Planum detecting over 70,000 grains, of which about 40,000 were in the range of 100 to 200 μm . The mean aspect ratio of grains at each sampled location ranged from 0.66 to 0.92, with standard deviations of 0.16 and 0.11, respectively. The aspect ratio is defined as the minor axis divided by the major axis, so it is the inverse of the elongation, with smaller values for aspect ratio indicating more elongated grains, so the elongation ranges from 1.09 to 1.52.

When it comes to conducting experiments in wind tunnels on Earth, a number of possible substitutes exist, each suitable for different purposes.

Sand high in silica is readily available. Typically the density is around 2650 kg/m^3 and the grain sizes vary greatly. For experiments on saltation, aeolian deposits of sand are rounder and offer the most similarity to what one might expect to find in an aeolian environment on Mars. The density of this material is somewhat similar to what is found on Mars.

Volcanic glass has been deposited on the surface by volcanic activity. The density of this material is around 2330 kg/m^3 for grain sizes ranging from smaller than 63 μm to 1190 μm . The material is often less round than sand (de Vet *et al.*, 2014).

Mars simulants are combinations of materials found on earth that together resemble the minerals found on Mars. The grain sizes are known beforehand. The simulants are relatively expensive and focus more on the chemical similarity than on the physical similarity (Cannon *et al.*, 2019; The Martian Garden, 2023).

Ground walnut shells have been used in Martian aeolian experiments since their density is about a third of the mass of the material found on Mars at 1100 kg/m^3 . Since the gravity on Earth is about a third of the gravity at Mars, this relationship allows for a more realistic approximation of the saltation trajectory of particles (Greeley *et al.*, 1976). A downside of using ground walnuts is that their shape is very angular, like volcanic glass.

Glass spheres have been used in experiments as well. This is a manufactured material which allows for more precise determination of the density. By using hollow spheres, the density can be changed. However, this material is expensive (B. White, 1979; Merrison *et al.*, 2007).

2.2.2. Wind tunnel settings

The AWSTII is a closed circuit environmental wind tunnel. It is a large capsule that is 10 m long and has an inner diameter of 2.1 m . The cross section of the test section has a width of 1.8 m and a height of almost 1 meter (Iversen, 2023). Wind flow is achieved by two fans at the downwind end of the tunnel that blow wind over and under the test section so that it can re-enter the test section upwind. The temperature can be regulated from 213 to 333 K and available gasses include air, CO₂, Helium and Nitrogen. The humidity of the air can also be controlled. Tests involving dusts can be performed and also experiments using sand can be done using the narrow test section, which has a cross section of 0.4

by 0.8 m (width x height). Below is an overview of previously used settings in similar studies and a comparison between the settings and the environment encountered on Mars (Holstein-Rathlou *et al.*, 2014; Iversen, 2023).

The atmosphere of Mars varies from one location to another due to the large range in altitude. Most missions have landed in lower regions of the planet where the pressure is higher. Values used density are generally around 0.02 kg/m^3 , while values for the pressure vary more. The pressure is found to vary from 4 to 8.7 mbar with about 6.35 mbar being the pressure at the altitude corresponding to the mean radius of the planet, which is the martian equivalent to sea-level. The temperature varies greatly from 140 to 300 K, with the average temperature being 218 K. The composition of the atmosphere is about 95% CO₂, with lesser amounts of Nitrogen, Argon, Oxygen and trace gasses (The European Space Agency, 2023; D. Williams, 2024).

In order to obtain representative results for saltation on Mars, the gas, pressure and temperature in the wind tunnel must be chosen so that the dynamic environment is similar. It has been found that air at ambient temperature lowered in pressure to around 10 mbar, generates the same dynamic environment as a very cold CO₂ environment as 6.5 mbar (Greeley, 2002). While this would generate similar aerodynamic forces, the gravity in the wind tunnel remains about three times as much as what is encountered on Mars, which is why in some experiments other materials such as walnut shells have been used. Andreotti *et al.* (2021) uses a different method by keeping the density ratio of particle to fluid similar to what is found on Mars. This is achieved by using ambient air at 13.8 mbar, resulting in a particle to fluid density of $1.59 \cdot 10^5$.

The shear velocity, u_* , relates the velocity of the medium to the stress it exerts on the sand grains based on the density of the fluid. u_* is determined by measuring the velocity of the fluid at different heights very close to the surface of the sandbed, up to about 10 cm using pitot static tubes. At around 10 cm, depending on the pressure, the flow is no longer influenced by the sandbed (Merrison *et al.*, 2008; Creyssels *et al.*, 2009; Andreotti *et al.*, 2021). A few different methods exist to estimate u_* from here. What they have in common is that they aim to find u_* and the surface roughness to fit an equation for the wind velocity profile through the data points collected at different heights above the sandbed (Bagnold, 1937; Merrison *et al.*, 2008; Andreotti *et al.*, 2021). This estimation resulted in a relationship of the wind tunnel fan frequency, a user input, to the shear velocity. The relationship depends on the pressure inside the tunnel, with increasing fan frequency required for lower thresholds (Andreotti *et al.*, 2021). In general, the threshold of a sediment can be determined qualitatively by establishing at which fan rotation speed saltation happens. This can be seen using a webcam and a lasersheet. Then, the shear velocity is computed from the fan frequency and the air pressure.

Little information is provided on the duration of the experiments done on Martian saltation other than Merrison *et al.* (2007), who ran the experiment for about two minutes, which was the time needed for most of their material to be removed.

Other experiments studying the mass flux due to saltation ran for 15 to 400 seconds depending on the grain diameter to ensure enough grains were collected (Rasmussen & Sørensen, 2008). A different investigation used less than 200 seconds to counteract the formation of ripples which was undesirable for this specific experiment (Rasmussen *et al.*, 2009). Carneiro *et al.* (2015) first used 2-3 minutes runs. These produced poor results so instead runs of 20 minutes were used. On the other hand, Iversen and Rasmussen (1999) used runs of 4 to 7 minutes to determine the effect of wind speed and bed slope on the sand mass flux. A study on the particle concentration and speed in the saltation layer used run times of several minutes (Carneiro *et al.*, 2015). Lastly, Rasmussen and Sørensen (1999) used runs of 45 minutes in the field, not in a wind tunnel. The experiment aimed to research mass transport at conditions where saltation should generally be not possible due to wind speeds being below the threshold. According to Rasmussen and Sørensen (2008) longer runs can remove bias by short term variations in the flow. Measurements should be taken for a time period at minimum longer than the time it takes the flow to move through the wind tunnel.

2.2.3. Instrumentation

Many different instruments can be used to measure the sand flux, determine if saltation is achieved, estimate the velocity of particles or take images. This subsection aims to give an overview of the possible relevant options.

One of the most common instruments for science missions to other celestial bodies is a visible wavelength camera. The first landers on Mars were all equipped with cameras. Mars 3, the Soviet Union lander transmitted part of an image before failing and the Viking 1 and 2 missions were both equipped with cameras having a resolution of about 25 mm per pixel. While these were the first pictures taken from the surface, microscopic images of a much higher resolution are needed to detect individual sand grains (Stryk, 2021; NASA, 2022, 2024).

Since then, NASA has used a number of microscopic imagers for her rovers. The Microscopic Imager (MI) on the Spirit and Opportunity rovers were the first cameras of adequate resolution. These images were used in a similar study about fabric strength (de Vet, 2013). Later, the Mars Hand Lens Imager (MAHLI) was developed with similar resolution but a lower possible working distance. This resulted in a higher possible resolution (Edgett *et al.*, 2012). The Wide Angle Topographic Sensor for Operations and eNginneering (WATSON) is based highly on MAHLI but has an even lower possible working distance, again resulting in a higher possible resolution (Edgett *et al.*, 2019). The first rover developed by ESA, the Rosalind Franklin, will use the Close-UP Imager (CLUPI) to take the highest resolution images yet, but this rover is yet to be launched (Josset *et al.*, 2017).

To compare images taken of the sandbed in the wind tunnel with images taken by current rovers on Mars, microscopic images with at least a resolution of 13.1 μm must be taken. A higher resolution would allow for more pixels per grain, making it easier to distinguish grains and their shape. At the AWSTII digital microscopes are available with a maximum resolution of 1.75 μm (Celestron, 2023; Iversen, 2023). This resolution is good enough to reproduce the results obtained from close up images of sand on Mars.

In the past, particle trajectories were determined using high-speed photography. However, recently, laser-based methods have gained traction. Laser sheets have been used in combination with cameras to determine the speed of particles in the flow and the speed of the flow itself. For the first application, laser sheets are usually beamed vertically down onto the sandbed with the long-axis pointing parallel to the flow and a camera positioned on the side of the experimental field pointing perpendicular onto the laser sheet to obtain pictures where the flow moves from one side to the other on the image. For the second application, very small particles that obtain the same flow properties as the medium or colored gas are injected into the stream. The light of the laser is scattered and the camera can visualize the flow of the particles.

Laser Doppler Anemometry (LDA or LDV) and imaging techniques such as Particle Image Velocimetry (PIV) and Particle Tracking Velocimetry (PTV) have been used to measure the speed of grains in the saltation layer, but PIV was found to be less accurate than PTV (Creysseles *et al.*, 2009).

For PTV and PIV a strong laser pulsates while beaming vertically to the ground to generate a vertical laser sheet. The particles are illuminated by the laser and a camera takes pictures at a very high frequency (Rasmussen *et al.*, 2015). PIV underestimates the velocity of saltating particles since it can not distinguish between ascending and descending particles. This is because PIV uses correlation between particles. PTV is preferred since it tracks individual particles and it can measure close to the bed. LDV struggles with measurements close to the bed, especially below 2-3 mm. Lasers can also be used to quantify the volume flux of sand moved (Rasmussen *et al.*, 2015). If the density of the sand is known, this can then produce a second measurement for sand mass flux.

While PTV seems the most accurate method of particle velocity determination, it is difficult to use in a setting where such a high number of particles are present such as in the planned experiment, instead LDV might be a better option due to its simpler setup than PIV (Dracos, 1996). A horizontal laser sheet in combination with a high speed camera can be used to determine if saltation takes place by illuminating the grains so they become visible for the camera (Andreotti *et al.*, 2021).

Sand traps can be used to determine the mass of sand grains passing through a certain volume in a specified amount of time. As sand traps are objects placed in the medium, they disrupt the flow by default. Therefore, they give an approximation of the mass flux. Different types of sand traps exist, as they have evolved through the past century. Important changes include the reduction of flow interference.

Multiple approaches exist to simulate the aeolian environment on Mars. Most commonly low pressure ambient air is used in combination with sand. A digital microscope can be used to take high resolution images of the sandbed to extract grain orientations using image analysis, while a laser sheet in combination with a high speed camera can be used to track individual grains and determine if saltation

takes place. In the next section tools to extract individual grains and their properties from an image will be compared.

2.3. Image and data analysis methods

To determine if preferred orientation due to saltation takes place and to quantify the degree of preferred orientation, microscope images need to be taken of the sandbed to determine the orientation of individual grains.

This part of the background information aims to summarize the available methods to extract grain properties and grain orientations from images from a software point of view and illustrate possible image pre-processing techniques to improve the ability of the software to extract information. First, Object Based Image Analysis will be introduced, followed by a summary and comparison of the available techniques. Following the comparison, different image processing techniques will be explained. Finally, the results of the comparison and the chosen methods will be presented.

2.3.1. Object based image analysis

Object Based Image Analysis, from now called OBIA, is a method to extract individual objects and information about the objects from an image, often containing multiple objects. In this case, the image is a microscope image of the sandbed and the objects are the grains in the bed.

The method has been used to segment grains and their properties in multiple studies both on Earth and Mars (Heilbronner, 2000; Li *et al.*, 2008; de Vet, 2013; Kozakiewicz *et al.*, 2023). While each of these methods use different software, they have in common that they detect grain edges in an image and make an object of the grain that has shape properties.

OBIA consists of two main concepts, image segmentation and object classification. Image segmentation is the process of clustering grid pixels into homogeneous groups called objects based on the values of the pixels in the image. Each image can be represented as 3D array with the rows and columns representing the height and width of the image in pixels and the depth representing the number of color channels. A black and white image only has one channel, indicating the grayscale value from 0 to 255. A colored image typically has three channels, representing the red, green and blue (RGB) colors, with each value ranging from 0 to 255 (Sagar *et al.*, 2023).

Object classification is categorization based on: object statistics, shape properties or topological relationships between objects (GISGeography, n.d.). In this case, classification is of lesser importance, as all objects are grains. For this step to be successful, the segmentation needs to deliver an image where each object has a clear boundary.

Before the progression of digital image analysis methods, grain shape properties were determined by hand. Grain boundaries would be traced by hand and using a ruler properties such as the long and short axes would be determined. This was a time consuming operation but can still be useful to verify the correctness of new software and to validate the results obtained in studies using digital methods.

The Particle Detection and Measurement Algorithm (PADM) has multiple segmentation techniques for different types of images. Every technique starts with the determination of the background and determination of the relationship of grains to the background in terms of particle size and brightness. The image is recreated using discs of a grayscale corresponding to the pixels under the disc. For the actual segmentation, there are three options, Binarization, Canny edge detection and the Watershed technique (Kozakiewicz, 2018).

For binarization the image is binarized, so every grayscale pixel is made either white or black, based on a threshold. Usually Otsu's threshold is used, which is determined by the program. Otsu's threshold is determined by trying different values and choosing the value that maximizes the variance between the white and black pixels (Otsu, 1979; MathWorks, 2023). This method is best used for objects that are not touching as the technique often groups them together into one object. Canny edge detection constructs edges where the values of neighboring pixels vary above a certain threshold (Canny, 1986). The edges are then dilated to include objects that would not have been included due to the lines not meeting or small gaps being present in the edges due to local values below threshold. The resulting outlines of grains are filled in and the result is the detected grains. Lastly, the Watershed technique combines the two previous techniques with the Watershed method. Firstly, the image consisting of disks is sharpened by subtracting a blurred version of the image from the original. Then, canny edge

detection and binarization are applied in parallel. The binarized image is used to determine the distance of each pixel within an object to the edge of the object and Gaussian filtering is used on the image to smooth the resulting image. The point in each object where the distance to the edge of the object is largest is determined and marked as a max distance point. The output of the canny edge detection is combined with this image and the combined image is subjected to Watershed segmentation using the Meyer method (Meyer & Beucher, 1990). Finally, the image is binarized to obtain the final result. Watershed can be used for images with grains that are touching. This procedure is very similar to the one introduced by Butler *et al.* (2001).

PADM has been used to extract grain sizes of thousands of grains on images of Mars taken by MI (Kozakiewicz *et al.*, 2023). However, the software does require manual input of multiple thresholds, settings for the Gaussian filter and opening and sharpening radii with very little documentation available (Ventola, 2022).

ImageJ is software to process images, based on NIH image (NIH, n.d.). ImageJ can also be used for non-geoscience purposes such as astronomy or bio-imaging (ImageJ, n.d.). Both programs can perform similar operations which are often performed using macros to automate processes, allowing for quick analysis of many images.

Both ImageJ and NIH Image can process images by changing contrast, smoothing, sharpening and applying edge detection. Furthermore, they can determine area, distance and angles. Due to its ability to accept macros and plugins it is highly customizable, but that also means the tool is not ready to use for most analyses and it requires customization to be used.

ImageJ can be used to segment images of non-touching grains primarily but has also been used to segment images taken by MAHLI (Weitz *et al.*, 2018). However, the segmentation was performed by hand. NIH has been used to automatically segment images of grains, but the images were taken of thin sections, resulting in well defined edges (Heilbronner, 2000). It uses a segmentation method that is similar to Canny, but also simpler.

A GIS is a program used mostly for remote sensing. Classification of buildings, bodies of water and agricultural land are some of its uses. Segmentation has been done in two ways using this software. On one hand, segmentation by hand has been done on microscope images of sand on Mars. This included drawing a polygon around a grain and estimating the grain properties using tools such as "minimum bounding geometry" (Gough *et al.*, 2021). On the other hand, Li *et al.* (2008) designed an elaborate model in arcGIS to automate the process of segmentation and classification. ArcGIS is one of many GIS applications. The model segments the image using the sobel edge detection method. The power of arcGIS shows in the ability of the program to open images in three color channels and perform the segmentation in parallel, then combining the result. Furthermore, once the analysis is performed, the user is left with a GIS database which also includes the location of grains on the image, next to the grain shape parameters found in other software as well. The downside to this software is that it is very complex to use and especially to automate. It is a useful tool to validate other automatic or semi-automatic software.

eCognition is software developed by Trimble (Trimble, 2024). It is designed for image analysis, specifically Object Based Image Analysis and is often used for aerial pictures or satellite images. eCognition constructs objects by merging pixels together sequentially based on the maximum allowed object size, the current shape of the object and the similarity of nearby objects that it is trying to merge. In the first round, every pixel is an object and the pixels are merged with their most similar neighbor. This process continues if there are very similar objects adjacent to the current object and if the combined object does not exceed the allowed size (Trimble, 2019a; Staengel, 2021).

It has been used to segment images of sand grains on Mars. The multi-resolution segmentation as described above was used. Then, classification of grains took place to remove the background noise and have only grains remaining. The grains were resegmented with a larger allowed object size to include grains that were segmented into smaller objects. Lastly, erroneously identified objects were removed by setting a filter on the roundness (de Vet, 2013).

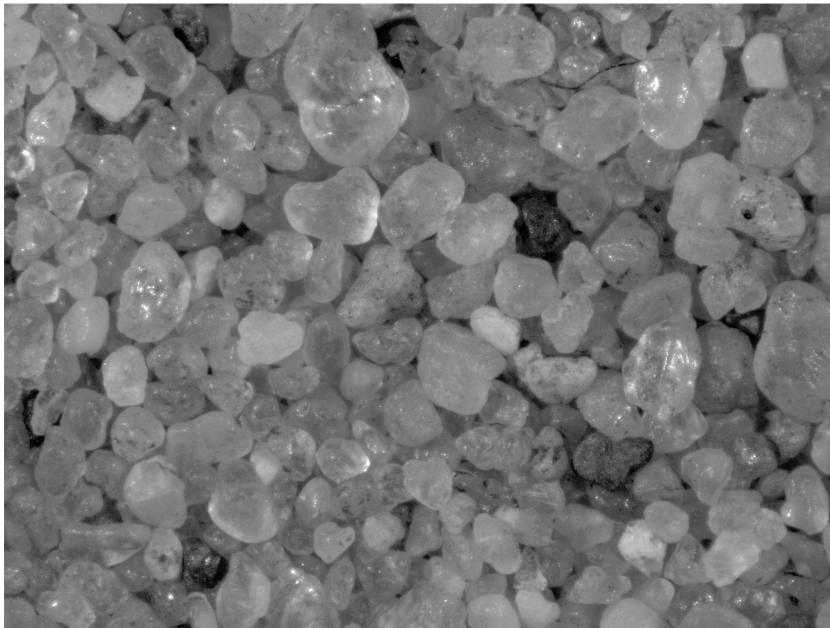


Figure 2.5: Microscope image of quartz

2.3.2. Image pre-processing techniques

In order to enhance the segmentation and classification processes described above, multiple pre-processing and intermediate processing steps can be applied. This subsection aims to highlight some of these available methods that have been used in similar studies. Possible techniques include changing of colors, brightness, contrast, sharpness and focus, and cropping. Throughout the section, the effects of each processing technique will be showcased on a microscope image of sand shown in black and white in Figure 2.5.

Different types of filters can be used to change the image and make it easier for software to distinguish individual grains. Three different filters along with the original image are shown in Figure 2.6.

Sharpening is used to increase the detail in an image. It does not inherently increase the number of pixels but it enhances local differences by subtracting a blurred version of the image from the original. This can reduce background noise and can be used to better analyze images with low resolution such as some MI images (Kozakiewicz, 2018).

Smoothing can aid in removing features that are smaller than grains but trigger edge detection. One of the methods to smooth an image is to use a localized median filter. Each pixel in the image is constructed by taking the median of the pixels in a user-determined neighborhood around the pixel. This filter has been applied in combination with the Canny edge detection to segment grains with sizes ranging approximately from 0.1 to 10 mm (Li *et al.*, 2008; Sulaiman *et al.*, 2014).

Another smoothing operation can be performed by representing an image using a structuring element. For example, disks of the same diameter can be used to represent sand grains, especially more rounded aeolian grains, which can reduce very local details that might trigger edge detection. The disk representation has been used on images of sand on Mars (Kozakiewicz, 2018).

One more smoothing method that can be used after edge detection is using a threshold for the size of a detected edge. This removes any edges that are detected inside grains due to highlights or shadows but keeps the larger edges, which are the size of grains (Li *et al.*, 2008).

A colored image is often saved as an RGB image. RGB stands for red, green and blue, and an image consists of an array of size equal to the pixels in the image in each of the color channels. For example, a 2560x1920 pixel colored image, can be represented as a 2560x1920x3 array. In one study, edge detection was performed separately for each color channel and the detected edges were combined in one image. Each channel had some unique edges that were determined. The advantage of this method is that edges can be detected that would be too weak to determine in black and white (Li *et al.*, 2008).

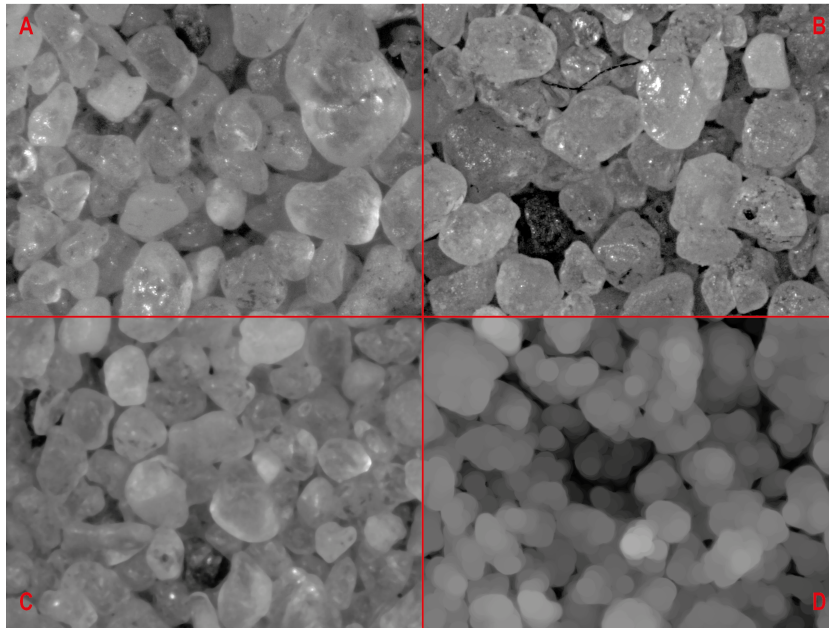


Figure 2.6: Microscope image of quartz showing different filters. A: Original image, B: Sharpened image, C: Image smoothed using localized median filter, D: Image opened using structuring disks. Images processed using MATLAB.

Inversion of the grayscale values is shown in Figure 2.7. In the case of this image, it appears that originally the background was dark and the grains were light. The inverted image of the original has been used to segment images in ImageJ using the Watershed method (Sulaiman *et al.*, 2014). Furthermore, it can be seen that most of the inverted image is very light gray with the highlights being black. In Figure 2.7 it can be seen that the majority of pixels in the original image are relatively dark. Most grains in the original grayscale image have pixel intensities that are relatively similar. This indicates that the majority of grains have a very similar shade of gray. This can make it more difficult to segment grains that are touching. On the other hand, even if grains are of similar color, edges may be well defined due to for example shading.

Changing the contrast so that there is a more uniform variation can have both positive and negative effects on segmentation. On one hand, edges can be defined more clearly but on the other hand the noise may increase significantly (Gonzalez, 2009). In the lower contrast image in Figure 2.7 it can be seen that the noise due to highlights is significantly less, but there is also less distinction between the grains. In the higher contrast image, while there is a greater difference between the grains and the background, there is much introduced noise within grains.

Since every segmentation technique requires at least some user inputs, such as binarization threshold or lower and upper thresholds for canny edge detection, it can be beneficial to crop images so that the thresholds can be optimized locally, then combining the results of the cropped images. A disadvantage of this method is that grains on the border of an image are generally removed from the analysis, thus possibly fewer grains are analyzed. Table 2.2 shows the Otsu threshold for the unedited A,B,C and D quadrants as shown in Figure 2.7. While the absolute magnitude has changed, the differences between the total threshold and the individual threshold remains fairly the same with the exception of quadrant B. Overall, the local threshold varies by up to 0.02 from the total threshold for both cases and the maximum difference in local thresholds is 0.03.

Local differences in focus can make it difficult for software to correctly segment images (Kozakiewicz, 2018). Ideally, the entire image should be in focus, but depending on the hardware and location of imaging, there could be a difference in height of the bed or the microscope might not be capable of focusing the entire field of view. In this case focus stacking can be used to combine the parts of the images that are in focus into one image that is in focus (Hovden *et al.*, 2011). This technique can be used in Adobe Photoshop, ImageJ (with plugins) and in Wolfram Mathematica.

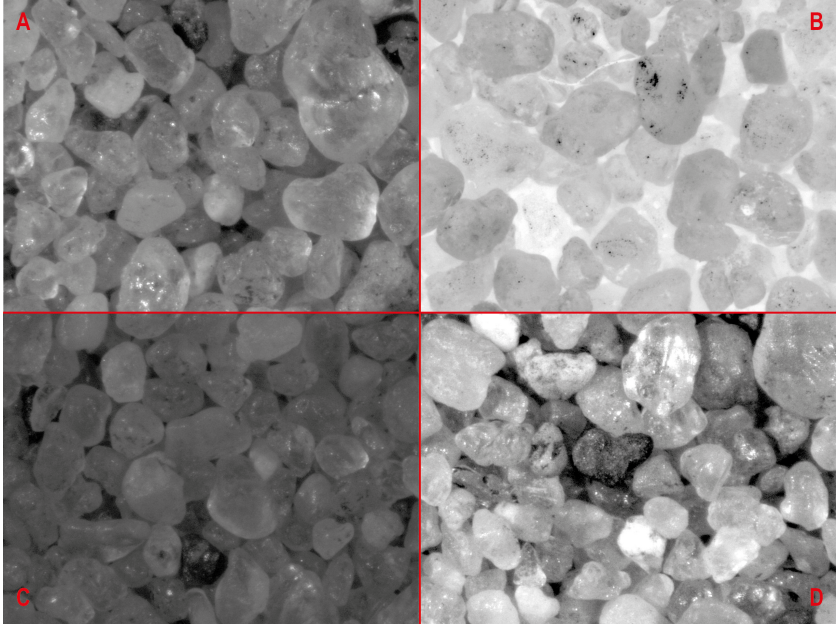


Figure 2.7: Microscope image of quartz Using different contrasts and inverted grayscale values. A: Original image, B: Inverted grayscale, C: Reduced contrast, D: Increased contrast. Images processed using MATLAB.

Table 2.2: Otsu thresholds determined using MATLAB for each part of the cropped image as is and using a smoothing disk or radius 40 pixels. The four cropped images represent quadrants A,B,C and D as seen in the other figures of this section. The threshold for the full image is shown in the right column.

Crop number	1	2	3	4	Full image
Otsu threshold	0.32549	0.29804	0.32157	0.29804	0.30588
Otsu threshold smoothing disk	0.24314	0.24706	0.25882	0.22745	0.23922

Multiple preprocessing techniques exist to improve the performance of the image analysis software. Typically smoothing or sharpening is used to remove noise, highlights and unwanted shadows while increasing the contrast between the grains and the background. Performing the segmentation over different color channels and combining the result may increase the performance of the software. Cropping of the image can improve the local result by optimizing thresholds for each cropped image. Focus stacking allows for analysis of samples that would be partly out of focus.

Table 2.3: Comparison between different OBIA methods.

Method	Benefits	Disadvantages
PADM	Specifically designed for this Implementable in any coding language	Many settings little documentation
ImageJ / NIH Image	Simple to use Elaborate documentation	Not suitable for touching grains
GIS	Highly customizable	Not used for this purpose before Not developed for this use
eCognition	Proven usage for this purpose	Requires license

There are multiple methods to determine grain properties. Object Based Image Analysis offers a method to segment images and generate objects from the grains. These objects can then be analyzed to extract information such as size, area and orientation. Four of the most used methods are binarization, edge detection, the watershed technique and object merging. Binarization and canny edge detection generally work best for well separated grains, while watershed and object merging have been successfully used for images with touching grains. There are many programs that can be used for OBIA. ImageJ and NIH Image are very similar and have been used to segment both touching and not touching grains. While they can be customized extensively for a specific use case, customization is required to provide usable results. PADM was specifically designed to extract grain information from images. The advantage of using this program is that the user can use three of the four segmentation methods, can customize the program and remove artifacts easily. The disadvantage is that there are many settings the user can change due to the complexity of the algorithm and there is very limited documentation. GIS have been used to analyze images of grains in thin sections. They have very extensive libraries of tools but usually require a license and are much more complicated to use than the previously mentioned software. In all uses of the software on images of Mars the grains were hand traced instead of the process being automatic. While GIS can perform segmentation, it was not specifically designed for it, so it is a small part of what the software was made for. eCognition by Trimble is similar to a GIS and also requires a license to use. However, this application is designed specifically for high level image processing and OBIA (Trimble, 2019b). This program has been used to segment images of Mars sand using the object merging technique. Table 2.3 shows a summary of the above described discussion.

PADM was chosen as the method to use for this research. Its proven use for segmentation of touching grains photographed with a microscope on Mars, coupled with the fact that it is freely available make it the most suitable candidate. The other options are either not suitable for touching grains, have not been used for the required purpose before or require a license making them not a viable option. The next chapter will explain how PADM works and provide a more detailed discussion of its use in this research.

In conclusion, saltation occurs when the fluid or impact threshold is exceeded, either directly through wind forces or particle impacts that eject grains into motion. During flight, grains are thought to align their long-axis with the direction of movement, gaining momentum before colliding with the surface, where they may rebound or dislodge additional grains. While numerical models can approximate the trajectories of ejected and rebounding grains, predicting their orientation within the sandbed remains challenging. Grain orientation is influenced by factors such as bed roughness, particle elongation, and shear velocity, with the degree of preferred orientation quantified by fabric strength R . Although it has been shown that grains align their long-axis with the wind, the extent to which high-energy impacts influence sandbed orientation, particularly under Martian conditions, remains an open question. In

the past, different materials, settings and instruments have been used when studying saltation or other forms of detachment. Quartz sand seems like a good material to use due its availability, somewhat similar density to the basalt found on Mars and its natural grain shape. Images of the sand bed in the wind tunnel can be taken using a microscope. Object Based Image Analysis, specifically the PADM algorithm can subsequently be used to extract individual grain orientations for further analysis and to determine the preferred orientation and fabric strength.

3

Materials and Methods

In order to answer the research questions, a set of wind tunnel experiments was designed and executed. A suitable wind tunnel had already been selected prior to the start of the project, but the sand, equipment, experimental procedure and data analysis methods were still to be determined.

The selected wind tunnel, the Aarhus Wind Tunnel Simulator II (AWTSII), is a closed circuit environmental wind tunnel. This means that there is no air coming in or out of the tunnel during an experiment, but rather the air is recirculating. More information on the specific wind tunnel can be found in chapter 2. The experiments consisted of inducing saltation at various friction velocities and pressure combinations. Images of the sandbed were taken using a microscope to determine the orientation of the grains and determine the influence of the wind tunnel settings on the particle orientation.

This chapter presents the methodology used to answer the research questions. It encompasses the preparation and execution of the wind tunnel experiments and the processing of the data obtained in the experiments.

3.1. Material

For the wind tunnel experiments, a large quantity of material was needed to create a sandbed on which grains could saltate. It was advised for the planned experiments in the specific wind tunnel to provide at least 50 kg of quartz sand. As stated in chapter 2, there were multiple possible options. Since the goal of the experiment was to understand the effect of pressure and velocity on the preferred orientation of saltating grains, specifically also at martian pressures, the material was chosen with a preference for similarity with martian sediment in active aeolian environments. An overview of the materials that were considered is shown in Table 3.1.

The choice was made to use quartz sand since it is widely available and material from active aeolian deposits can be easily collected. As stated in Table 3.1, volcanic glass and ground walnut shells are more angular than sand, even more so compared to sand found in aeolian deposits which tends to have

Table 3.1: Overview of considered materials for the wind tunnel experiments.

Material	Benefits	Disadvantages	Sources
Quartz sand	Readily available Round shape	Little control over shape	Greeley, 2002 Andreotti <i>et al.</i> , 2021
Volcanic glass	Resemblance to Mars	Angular	de Vet <i>et al.</i> , 2014
Ground walnut shells	Simulates Mars' gravity	Angular Different interparticle forces	Greeley <i>et al.</i> , 1976 Greeley <i>et al.</i> , 1980
Glass spheres	Adjustable size Adjustable density	Expensive	B. White, 1979 Merrison <i>et al.</i> , 2007
Mars simulants	Realistic composition	Expensive	Cannon <i>et al.</i> , 2019 The Martian Garden, 2023

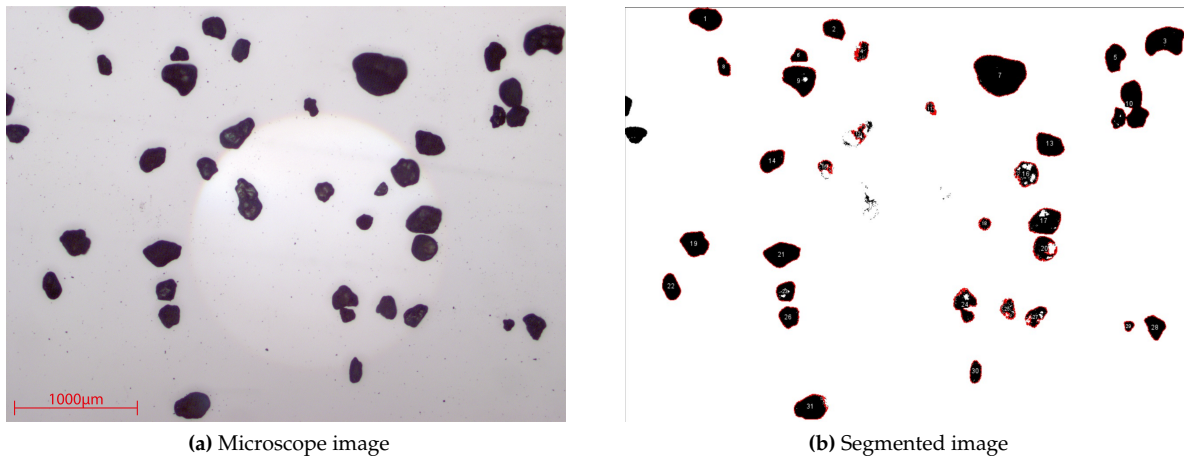


Figure 3.1: Microscope image of the sample from Bedaf and the segmented grains.

a rounder shape due to continuous movement of, and friction between grains. Glass spheres and mars simulants would have to be manufactured specifically for the experiment, which was not possible given the large quantity of material needed.

3.1.1. Choice of material

Two options were considered for quartz sand, material from the Bedafse Bergen and sand from the dunes of Texel. The dune of Bedaf is an aeolian deposit. Due to the excessive removal of vegetation, the sandy upper layer of the soil has been subject to aeolian processes for hundreds of years (Den Bosch Region, 2024; Gemeente Maashorst, n.d.). The sand from Texel consists of material that has washed up from the sea, likely containing larger concentrations of calcium than material from Bedaf.

Samples that were already available from both these deposits were compared using a microscope to determine their grain size distributions. For each sample, three glass microscopy slides were prepared. A small quantity of grains was deposited onto the glass slides, taking care to minimize overlapping or touching of grains. The slides were then studied using dark-field microscopy. The slide was placed underneath the objective and the lower light source was used. For the Bedaf sample, 16 images were taken and for the Texel sample 15. Figure 3.1 shows one image of the Bedaf sample.

Subsequently, ImageJ, an image processing program, was used to segment the image and classify the grains (ImageJ, n.d.). As mentioned previously, image segmentation is the process of clustering grid pixels into homogeneous groups called objects based on the values of the pixels (Sagar *et al.*, 2023). Object classification is categorization based on object statistics, shape properties or topological relationships between objects (GISGeography, n.d.). Each resulting classified image, as shown in the right image of Figure 3.1 was examined by hand and false positives, such as the cluster of three grains in the top right corner, numbered 10, were removed. Using this method, 426 grains were identified for Bedaf and 284 for Texel. Their grain size distributions are shown in Figure 3.2. Note that only grains with an equivalent diameter of 25 to 525 μm were taken into account since larger grains usually do not saltate.

It can be seen that the sample from Bedaf contains relatively smaller grains and that the population is slightly more spread out. Since the minimum of the fluid threshold for Mars typically lies between 100 and 200 μm (Greeley *et al.*, 1980; Iversen & White, 1982a; Greeley & Iversen, 1985; Shao & Lu, 2000), and the impact threshold between 50 and 100 μm (Claudin & Andreotti, 2006; Kok, 2010a, 2010b), the choice was made to use the sand from Bedaf. Furthermore, as this is material from an aeolian deposit, it is expected that the grains are more rounded and resemble the shape of aeolian deposits of Mars better than sand from Texel.

Furthermore, the grain size distributions found on Mars, resemble the sample from Bedaf more than the sample from Texel. Kozakiewicz *et al.* (2023) found that most sand-sized grains (with a diameter of at least 100 μm) had a diameter ranging from 100 to 300 μm with most grains having a diameter of 110 to 150 μm . A different study with a much smaller sample size of around 1000 grains ranging from 64 to 320

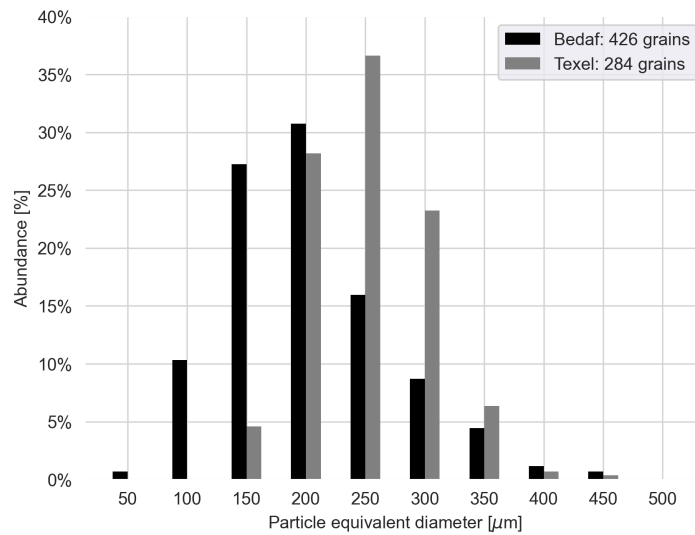


Figure 3.2: Grain size distributions of the Bedaf and Texel samples using microscope images.

μm found that 70% of the grains had a diameter between 88 and 152 μm (Sullivan & Kok, 2017). Both these studies support the decision to use the material from Bedaf, as the grains from Texel are larger.

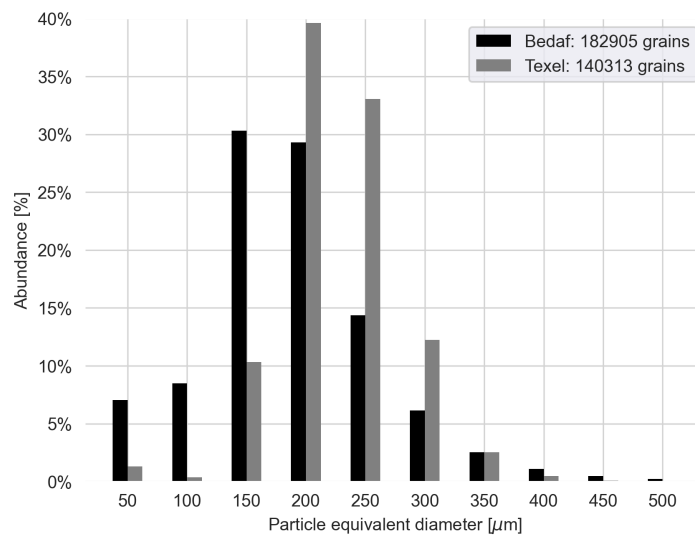


Figure 3.3: Grain size distributions of the Bedaf and Texel samples using dynamic image analysis.

Validation of material choice

Due to time constraints, the choice of which material to use and its collection were made and done before an in-depth analysis could be performed to compare the two samples. Only a brief comparison was done using a microscope, as described above. In order to validate this decision, a more elaborate analysis was performed, as described below.

Samples from both deposits were compared using a dynamic imaging analyzer. At the laboratory for sedimentary research of the Vrije Universiteit Amsterdam (VU), a combination of an image analyzer and a wet disperser was used to take images of both samples. The image analyzer called QICPIC, takes images using a high-speed camera and pulsing light, allowing for binary images to be taken to ensure a clear distinction between object and background (Sympatec GmbH, 2024a). The wet disperser, SUCCELL, suspends the particles of the sample in water to guide them through the QICPIC (Sympatec GmbH, 2024b).

Both samples were prepared for analysis by adding the specimen and tetrasodium pyrophosphate, $\text{Na}_4\text{P}_2\text{O}_7$, to a beaker in a 2:1 ratio. A micro laboratory spoon was used to add a heaping spoonful of sediment to the beaker. Then, about half this amount of tetrasodium pyrophosphate was added, along with 100 ml of demineralized water. Each mixture was brought to a boil in a beaker and left to cool again. $\text{Na}_4\text{P}_2\text{O}_7$ improves the dispersion of the grains in the medium and reduces the chance of them sticking together, which would create false shapes for the image analyzer (Abdulkarim *et al.*, 2021).

After cooling down, each sample was added to the wet dispenser, along with more demineralized water, to suspend the particles. The QICPIC-SUCCELL combination ran for a few minutes and took 7500 images of each sample. For the Bedaf case, 382156 particle shapes were determined, and for Texel 228002. The significant difference in number of detections is likely an effect of inaccurate determination of the sample size. However, a difference in grain size distribution can also be responsible as a spoonful of larger grains contains fewer particles. The resulting grain size distribution can be seen in Figure 3.3. Note that only grains with an equivalent diameter of 25 to 525 μm were taken into account. Much like in Figure 3.2, it is clear that the sample from Bedaf overall consists of smaller grains than the sample from Texel, and the distribution of the Bedaf sample is more spread out than the one from Texel. It was concluded that material from Bedaf was indeed the better choice.

3.1.2. Collection of material

After the determination of which material to use, it was time to collect the material for the experiments. Permission from the municipality was granted and a suitable spot on the dune in Bedaf was chosen to gather the sand. An image of the dune is shown in Figure 3.4



Figure 3.4: The Bedafse Bergen

The dune called Bedafse Bergen was formed in the Middle Ages (Doorenbosch & van Mourik, 2016). The sand itself was deposited during the Last Glacial Period, originating from glaciers. Due to the sparse vegetation, large areas of Northern Europe were covered by these sands, which experienced aeolian activity. This decreased when vegetation coverage increased during the Holocene (Van Mourik *et al.*, 2012). These sands can still be found in areas in, among others, Drenthe, the Veluwe and the Maashorst. The sandy areas were mostly covered by forests and heaths, which were used for shepherding. Due to increased deforestation during the 11th century, the settled sands experienced a surge in aeolian activity. Farmers used coppice hedges, semi-natural hedges made from trees that were cut low to the ground so that they would grow multiple stems, combined with branches to protect their farmland from the blown sands. Over time, the prevailing South-Western winds, which are typical for the Netherlands, collected increasing quantities of sand against the coppice hedges, forming the dunes of the Bedafse Bergen (Doorenbosch & van Mourik, 2016; Wallinga *et al.*, 2019). Thus, the formation of the dunes is a result of deposition during the last ice age and anthropogenic activities such as deforestation and the placing of coppice hedges.

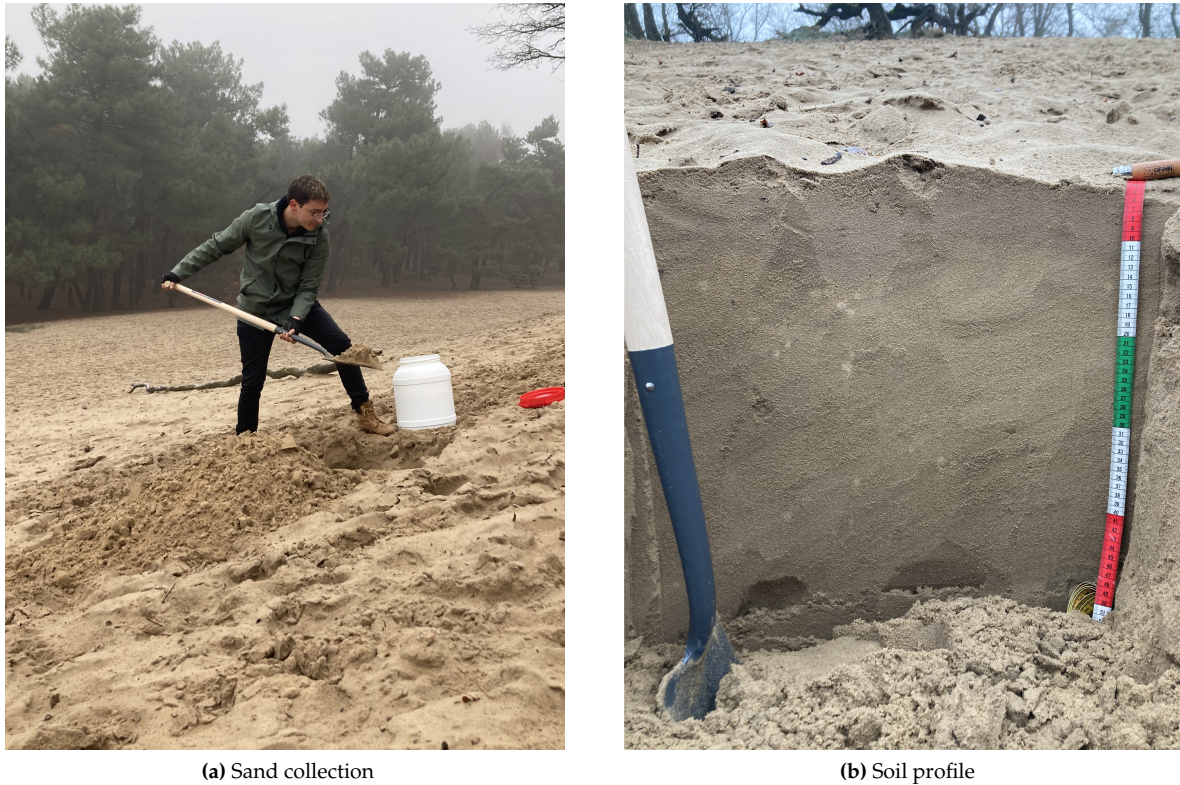


Figure 3.5: Sand collection at the Bedafse Bergen.

The location that was chosen to collect the sand lay approximately halfway up the dune, away from trees. Here a hole was dug of approximately 20 cm deep, equivalent to the depth of the shovel head, and this material was discarded. Digging a hole before collecting the material reduces the amount of organic material present such as soot from surrounding houses but also hair and waste from animals (Carter & Gregorich, 2007). Two containers with a content of 26 litres were filled with sand and the hole was closed again. Figure 3.5 shows on the left the researcher collecting the sand and on the right the soil profile of the upper half meter of the dune.

3.1.3. Preparation of material

The collected sand contained water, which would likely result in unfavorable interparticle forces during the experiments, and possibly consisted of particles too large or too small for saltation. Therefore, the sand was dried and sieved. The wet sand was placed in twelve metal containers and spread out in a layer of approximately 4 cm thickness. The containers were placed in an oven and dried for 24 hours at 100 °C. The mass of the sand in each container before and after drying is shown in Table 3.2 and Figure 3.6. It can be seen that for the last container, the mass seems to increase. This is likely due to an error during the weighing before drying, as the weighing after drying was repeated for this container to ensure the result was correct.

Table 3.2: Overview of sand container masses prior and after drying, excluding the mass of the container, in grams. For container 12, the mass of the wet sand lower than expected due to an error during the weighing.

Container	1	2	3	4	5	6	7	8	9	10	11	12
Wet mass [gr]	5100	5310	6055	6210	6245	6245	6340	6440	6655	6685	6815	7215
Dry mass [gr]	4775	4980	5775	5900	5900	5910	6025	6155	6350	6430	6520	7300

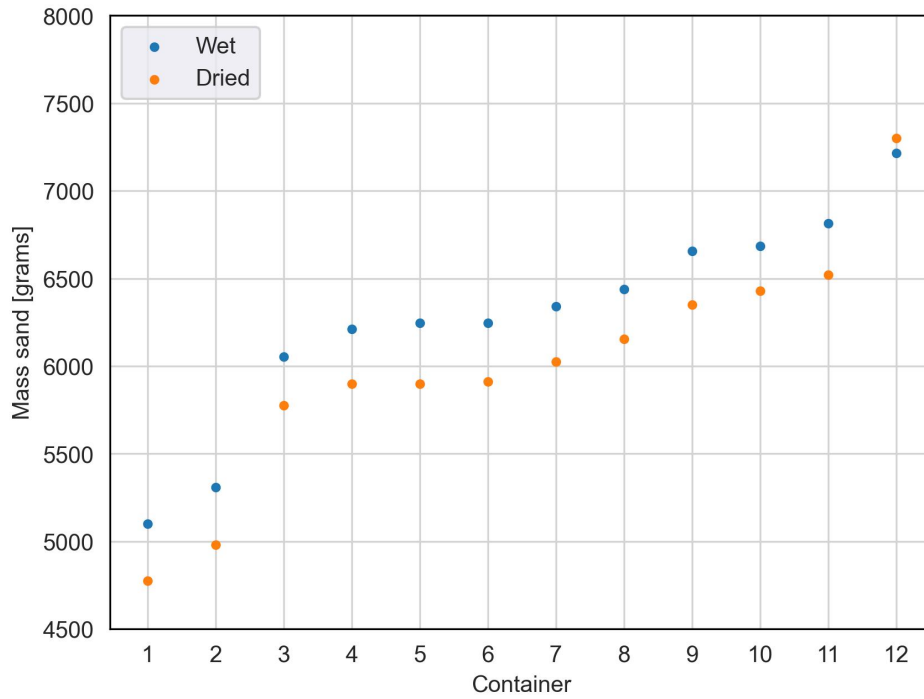


Figure 3.6: Mass of sand in each container excluding the mass of the container, before and after drying.

Table 3.3: Overview of material size caught in each bucket and the vertical structure of the sieves.

Bucket	Grain sizes
1	> 1000 μm
2	500 μm < and < 1000 μm
3	63 μm < and < 500 μm
4	< 63 μm

After drying, the sand was sieved using a vibrating sieving machine. Based on the availability of mesh sizes, the decision was made to use 63 and 500 μm as lower and upper limits, as particles engaging in saltation are typically sized 70 to 500 μm (Nickling & McKenna Neuman, 2009). Three sieves were placed on top of each other, with mesh sizes 63, 500 and 1000 μm starting from the lowest one going up. Three sieves were needed to reach the required height to secure the inlet, so the upper sieve should not inhibit any desired material from passing through. Each sieve and the basin below the smallest sieve had an exit with a pipe leading to a bucket to collect the material. Table 3.3 shows the vertical structure of the sieves and the corresponding grain sizes collected in each bucket. The contents of buckets 1, 2 and 4 were discarded and the contents of bucket 3 were collected in the original 26 liter containers. In Figure 3.7 the mass loss of each process can be seen. The dried sand with a mass of 65020 grams was sent to Aarhus to be used in the wind tunnel experiments.

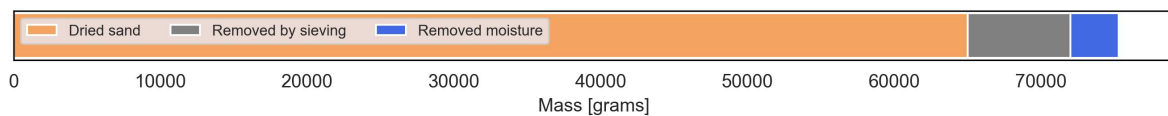


Figure 3.7: Mass loss at each sand treatment step. The removal of 3295 grams of moisture due to drying and 7000 grams of material due to sieving result in 65020 grams of dry sand.

3.2. Wind tunnel experiments

As introduced in chapter 1, the goal of this research project was to quantify the preferred orientation of saltating grains in low-pressure atmospheres using wind tunnel experiments. To this end, the Aarhus Wind Tunnel Simulator II (AWTSII) was chosen as this is an environmental closed circuit wind tunnel that allows the use of sand. This specific wind tunnel has been used to research entrainment of small particles such as sand and dust, specifically on Mars (Colombatti *et al.*, 2018; Waza *et al.*, 2023), and has been used to study the saltation threshold on Mars (Andreotti *et al.*, 2021). The wind tunnel belongs to the Department of Physics and Astronomy of Aarhus University in Denmark. In order to determine the degree of preferred orientation, images of the sandbed were taken using a microscope. This section will present the setup and execution of the wind tunnel experiments.

3.2.1. Experimental setup

For the experiments, a setup similar to Andreotti *et al.* (2021) was used. An insert was placed into the wind tunnel to narrow down the active cross section of the wind tunnel. The insert consisted of four parts, each 1 m long, 40 cm wide and 80 cm high. Below, in Figure 3.8 the setup is shown. In the insert, a 2 cm thick sandbed was created using the material that was collected and treated, as described above in section 3.1. Near the downwind end of the sandbed, a horizontal laser sheet was placed approximately 1 cm above the sandbed, at a 45° angle pointing sideways and upwind, as can be seen in the top view of Figure 3.8. A webcam was positioned about 40 cm from the downwind end of the sandbed looking sideways over the sandbed, focused on the intersection with the laser sheet to detect saltating grains, as can be seen on the top view and side view of Figure 3.8. Furthermore, at the middle of each 1 m section of the insert, a webcam was placed above the top plane looking down at the sandbed, continually taking images of the sandbed to image ripple formation. A lamp was placed outside the tunnel at the upwind end shining through a window. This horizontal light helped with imaging the ripples, as it generated shadows for small disturbances of the sandbed. A sand trap was placed on the sandbed, with its entrance approximately 25 cm from the downwind end of the bed. The opening of the sand trap was 1 cm high and 2 cm wide. To increase the uniform lighting during image capturing with the microscope, an LED ring light was placed approximately 75 cm from the downwind end on top of the insert section shining down. Finally, a digital microscope was used to take images of the sandbed. It was placed on top of a supporting construction that enabled the setup to rest on the sides of the sandbed holder so it would not disturb the sandbed while allowing the microscope to take images at a distance of 3 cm above the sandbed. The supporting construction is visible in the inside view of Figure 3.8.

3.2.2. Experimental procedure

A number of tests were conducted before the experiments commenced. First, two tests were performed to determine if closing or opening the wind tunnel affected the orientation of the grains in the sandbed. Using a digital microscope mounted to the side of the insert looking down at the sandbed at an angle, pictures before, and after closing and reopening the wind tunnel were taken, and a video showing the same procedure was captured. No movement was found. Next, a microscope was placed on top of the sandbed using the support described above. Pictures of the sandbed were taken before closing and after reopening. While there was a slight translation of 5 pixels, about 21 μm , no change in the orientation of the grains was visible. During testing, it was determined that the microscope was unable to bring the entire image into focus, so it was decided to take three images per location, each at a different focus depth. Furthermore, it was verified that the images were segmentable using a freely available version of PADM written in MATLAB (Nowiński, 2020).

Each experiment followed a similar procedure. First, the sandbed was either pulled out the upwind end of the wind tunnel and was smoothed, or without removing the sandbed, the last downwind meter of the bed was smoothed. The sandbed was then slid back in and the upwind end of the tunnel was closed. A handful of grains was sieved on top of the downwind end of the sandbed using a 250 μm mesh and the sandtrap was placed. The grains were sieved on top in an attempt to remove any possible signal induced by the smoothing of the sandbed, as grains subjected to only gravity show a random orientation (Dapples & Rominger, 1945). All lights were turned off, except the LED ring light, and the microscope and its support were placed on the sandbed. Four or five images were taken of the sandbed prior to the experiment and the microscope was removed. The tunnel was closed and the light upwind of the tunnel was turned on. The wind tunnel was pumped to the desired pressure. The overhead webcams

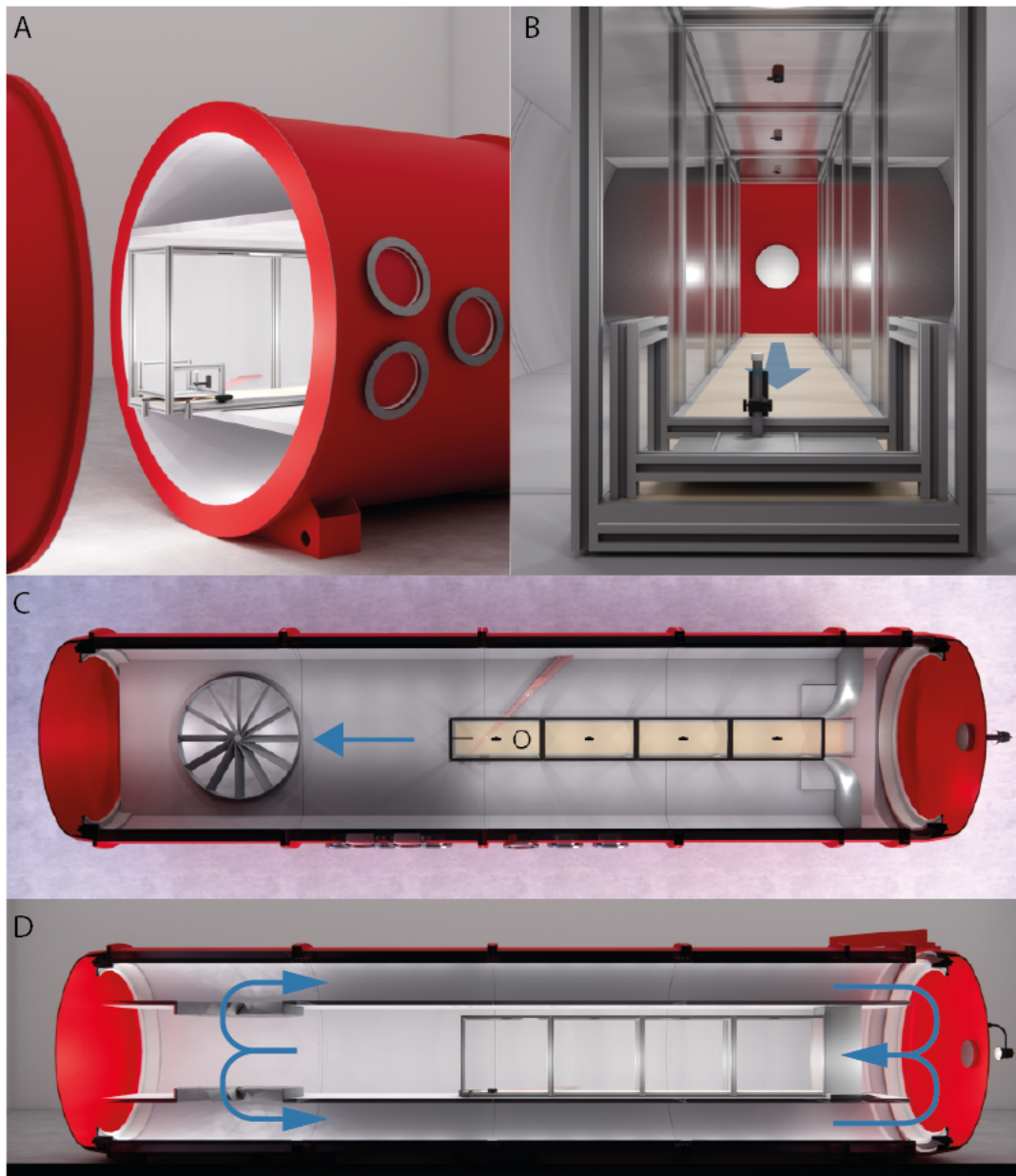


Figure 3.8: Schematic views of the experimental setup in the AWTSII-II. **A)** The test section opened. **B)** The inside of the narrow insert, showing the microscope setup looking upwind. **C)** Top view of the wind tunnel showing on the left the fans and on the right the sandbed. The blue arrow indicates the flow direction. **D)** Side view of the wind tunnel. The blue arrows indicate the flow direction.

and the side webcam started recording, and the fans were turned on at the desired fan frequency, which corresponds to a friction velocity dependent on the pressure. After a predetermined duration, the fans were turned off and the recordings were stopped. The wind tunnel was pumped back up to ambient pressure and opened. The sand trap was taken out and its contents were weighed. Again, all lights except for the LED ring light were turned off and microscope pictures were taken at 3 focus depths at 7 locations in 3 rows, resulting in 21 measuring locations and 63 images in total per experiment. The images were taken in a 3x7 grid at 2 cm intervals. The locations of the images on the sandbed are shown in Figure A.1.

An overview of each experiment, and its settings and specific procedures is presented in Table A.1. To answer the research questions, the idea was to determine the preferred orientation and fabric strength

for each image and experiment. The pressure and velocity of each experiment varied so the influence of these parameters could be investigated. For the experiments under Martian conditions, ambient air instead of CO_2 was used, at a pressure of 14 *mbar*. At this pressure, the ratio between the density of the medium and the density of the sand grains is equal to that found on Mars (Andreotti *et al.*, 2021). This scaling method allows for the effect of the densities on the aerodynamic forces to be similar to what would be the case on Mars. As this research is focused primarily on the aerodynamic streamlining of grains during saltation, the direct effect of gravity is of less importance, although it plays a role in the determination of the threshold velocity and affects the impact speed of grains, as will be discussed in chapter 5.

The threshold shear velocity was determined for each pressure separately. The wind tunnel used the fan speed in RPM as input (Holstein-Rathlou *et al.*, 2014). The corresponding shear velocity was determined using Equation 3.1 (J.P. Merrison, personal communication, December 16, 2024), which gives the ratio of shear velocity, u_* , in *m/s* to fan speed, ω_{fan} , in RPM, based on the pressure, P , in *mbar*, specifically for the Aarhus Wind Tunnel Simulator II.

$$u_*/\omega_{fan} = 0.0000447609 \cdot (\log_{10}(P))^5 - 0.000326804 \cdot (\log_{10}(P))^4 + 0.000626181 \cdot (\log_{10}(P))^3 + 0.0002305 \cdot (\log_{10}(P))^2 - 0.00180848 \cdot \log_{10}(P) + 0.004703371 \quad (3.1)$$

The threshold fan speed and shear velocity were determined visually by gradually increasing the fan speed of the wind tunnel while closely monitoring the webcam looking at the laser sheet over the sandbed. If multiple bursts of grains were visible in close succession, the current setting was marked as the threshold for that pressure. Examples of a calm sandbed, a few saltating grains and constant saltation are shown in Figure 3.9. The threshold was determined visually since the grains were not all of the same size. This excluded the possibility of determining the threshold numerically. The visual determination was also performed in a similar experiment by Andreotti *et al.* (2021), although they used only grains of one particular size.

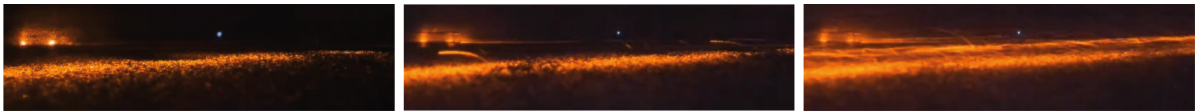


Figure 3.9: View of the sandbed and the lasersheet through the sideways looking webcam. On the left, the sandbed without movement. In the middle, two saltating grains. On the right, permanent saltation. The flow direction is right to left.

The variation in duration between some of the experiments, as shown in Table A.1, is mostly due to the increased amount of transport happening at higher friction velocities. Since the goal was to study the effect of saltation on the sandbed, as soon as an entirely new layer was deposited on the original layer, the experiment had run for enough time.

In total, fourteen experiments were performed, of which ten form the main research. A brief overview of these experiments is shown in Table 3.4, while the full overview can be found in Table A.1. The numbers correspond to the chronological order of the experiments and are the same in both tables.

3.3. Image and data analysis

The images taken by the microscope were the main data product of the experiments. Thus, their processing was a large part of this research project. In section 2.3 possible pre-processing and image processing methods were discussed. In this section, a different pre-processing technique will be introduced that was necessary for the analysis of the images. Certain pre-processing methods from the previous chapter are integrated into the PADM algorithm and will be further discussed in the segmentation section. The following procedure was used for the image analysis of the microscope images:

First, pre-processing was performed to enhance image processing. Next, segmentation and classification were applied to extract individual grains and their shape parameters. The PADM algorithm, originally developed for analyzing Mars rover microscope images, was used for this purpose, enabling

Table 3.4: Overview of the ten experiments that are part of this research.

Experiment	Pressure (mbar)	Shear velocity (% of u_{*f})
3	1000	150
4	1000	120
5	14 (Mars)	120
6	14 (Mars)	150
8	720	120
9	720	150
10	240	120
11	240	150
12	480	120
13	480	150

the extraction of shape properties such as the particle diameter and elongation (Kozakiewicz, 2018). Finally, the extracted data was analyzed to determine relevant properties, primarily the fabric strength.

3.3.1. Pre-processing

To improve the performance of the segmentation, often pre-processing steps are performed on images. In this case, it was determined during the experiments that the microscope could not focus on the entire field of view, so multiple images were taken at each location but at different focus depths. Focus stacking can be used to combine the parts of each image that are in focus to create an image that is completely in focus.

First, this process was done using Adobe Photoshop, as this program was readily available and had a built-in option to focus stack. However, upon closer inspection, it was determined that a different tool was needed. For one, the edges of the combined image would be extremely blurry and due to the built-in settings, lines would appear at the edges where the images did not overlap. The slight lack of overlap at the edges is a result of the focusing method of the microscope, as this was done by zooming in and out slightly, increasing or reducing the field of view. Lastly, in some cases Photoshop would almost completely neglect two of the three layers, mostly using the middle one.

A second tool was tested called Helicon Focus 8, which is a program designed specifically to focus stack microscope images. The software has numerous settings that are beneficial for specific use cases. The main methods of focus stacking are called weighted average, depth map and pyramid. The first method generates a weight based on the contrast of each pixel of each image, then takes the weighted average of all pixels from every image. It is the most generally applicable method. The depth map method generates a depth map based on the sharpest pixels of each image, then attempts to join the regions of each image that are flagged as "sharp". It does not work well for images with crossing lines. Lastly, the pyramid method decomposes each image into layers of features at different frequencies, then compares each layer of each image to find the sharpest layer, combining the sharpest layers into a new image. It does not work well to remove glare.

The three methods were compared by analyzing the focus stacked image using PADM in its MATLAB version, with the default values for Watershed segmentation. The weighted average, depth map and pyramid methods resulted in the detection of 192, 191 and 181 grains, respectively. The weighted average method was chosen as this is an overall good method resulting in most detected objects and the third method generally performs poorly for images with glare.

The weighted average method has two parameters that can be changed, the radius and smoothing. The radius affects the area around each weighted pixel that is marked as "sharp" during the stacking process. A larger radius leads to larger areas around "sharp" pixels being used from that original image. A larger radius can reduce artifacts but also remove details. The smoothing parameter affects how the stack of images is combined. Specifically, a larger smoothing parameter introduces more smoothing, making the transition from a sharp part of one image to the sharp part of a different image less pronounced, but possibly creating a blurry image. Smaller smoothing creates a sharper image but

Table 3.5: Number of detections for different focus stacking settings of Helicon Focus, using the Watershed segmentation method in the MATLAB version of PADM with its default settings.

Smoothing \ Radius	Radius					
	1	8 (default)	20	30	40	50
1	-	191	-	-	-	-
4 (default)	178	192	195	195	197	197
10	-	196	-	-	-	-

may introduce artifacts.

For the weighted average method, first three values were tested for the radius parameter to see the effect of changing from the default value, 8, to the smallest value, 1, and the largest value, 50. It was determined that a larger radius is beneficial, so next the values 8, 20, 30, 40 and 50 were compared. For the smoothing, the values 1, 4 and 10 were compared, with 10 being the maximum value. The number of detected particles for the combinations of tested settings can be seen in Table 3.5. While a radius of 1 gives a somewhat significant reduction in the number of detected particles, the other settings all produce between 191 and 197 detections. Since the difference is quite small, the figures of the contours drawn onto the original images were compared qualitatively to determine which settings produce the most correct contours. It was found that a radius of 20 and a smoothing of 4 produced the best results, although the differences were small. A comparison between the performance of Photoshop and Helicon Focus 8 is shown in Figure 3.10. All images of each experiment were focus stacked to prepare for the segmentation.



Figure 3.10: Close-up of the two focus stacking methods. On the left using Adobe Photoshop and on the right using Helicon Focus 8. Note the lines on top of the left image and the increased blur on the right of the left image.

3.3.2. Segmentation and classification

As mentioned in the introduction of this section, PADM was used to identify grains in the microscope images taken in the wind tunnel. The choice for this method lies in its familiarity due to previous usage and the fact that it is specifically designed for the purpose that is needed in this research, namely identifying grains in images of the sandbed taken with a microscope (Kozakiewicz, 2018; Kozakiewicz

et al., 2023). Other options that were briefly considered include the use of GIS software such as ArcGIS or QGIS, which has only been used in manual methods (Li *et al.*, 2008; Hassanpour, 2012), or the development of a Neural Network, which did not seem feasible given the perceived workload necessary to develop and train it.

The original PADM algorithm was developed using Wolfram Mathematica and is not publicly available. An interpretation of the algorithm was made in MATLAB, but its use of a GUI made automation difficult (Nowiński, 2020). These issues combined with limited knowledge of these programming languages led to the decision to develop the algorithm using Python, based on the MATLAB interpretation and the publication of PADM by Kozakiewicz (2018).

The benefits of developing the interpretation of PADM in Python are that total familiarity with the algorithm was required and that experience with Python led to customization and automation options. The downsides were the labor involved with making the tool and the sometimes unclear steps followed in the publication or the MATLAB version. Below, an overview of the original algorithm is given, followed by the Python adaptation. Finally, the determination of the input settings is discussed.

Original PADM algorithm

The original PADM algorithm consists of four main steps, as shown in Figure 3.11. First, it is determined whether the background is plain or noisy, based on a so-called background procedure. The image is opened in grayscale using a structuring disk, which smooths the image. Then, the image is binarized using Otsu's threshold, creating a binary image (Otsu, 1979). The sum of all pixel intensities, V_{BF} , is taken as shown in Equation 3.2, with p corresponding to a single pixel, D to the entire image domain and f to the pixel intensity. Lastly, the sum of intensities is normalized by dividing by the sum of all pixel intensities of the original image, V , resulting in $V_N(R)$ as can be seen in Equation 3.3.

$$V_{BF}(R) = \sum_{p \in D} f(p) \quad (3.2)$$

$$V_N(R) = V_{BF}(R)/V \quad (3.3)$$

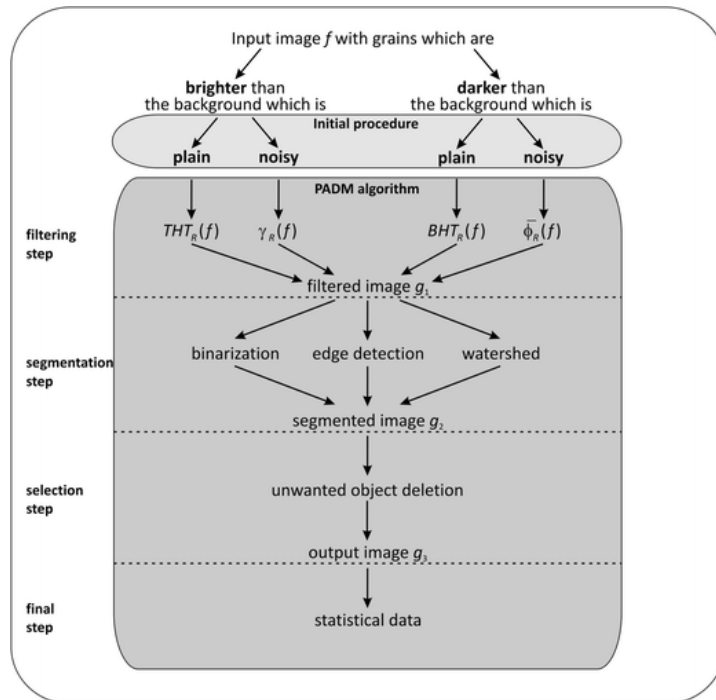


Figure 3.11: The scheme of the PADM algorithm. (Kozakiewicz, 2018)

This step is firstly done with a disk radius of 1, but repeated by increasing the disk radius by 1, until the obtained $V_N(R)$ encounters its first minimum. In other words, if the normalized sum of

pixel intensities is smaller than the previous value for $V_N(R)$, the first minimum is found. If then, this minimum is larger than an empirically determined value, in the case of Mars 0.06, the background is deemed noisy.

For the second step, filtering is applied based on the previous classification of the background and the brightness of the grains compared to the background. If the background is plain, the background is removed from the image using a top-hat transform if the grains are brighter than the background, and a bottom-hat transform if the grains are darker than the background. This is achieved by representing the image using structuring disks that are larger than the largest particles. If the background is noisy, the image is represented using structuring disks that are of the same size as or larger than the background irregularities.

Next, the segmentation is performed using binarization, edge detection or the watershed method. Binarization converts the filtered image into a binary image depending on a given threshold value, for which often Otsu's threshold is used. Edge detection passes a filter over the image that is of approximately equal size to the grains to identify large changes in pixel intensity, indicating the edge of a particle. The identified edge lines are thinned to 1 pixel and the contours are filled, creating again a binary image. Erosion and dilation are performed to remove the remaining edge lines that did not result in closed shapes and remained as lines, using a square structuring element with the size of 1 pixel. The third option, the watershed segmentation technique, is the most involved method and combines the previous two techniques. An overview of the results of most steps is shown in Figure 3.12. The filtered image is sharpened using unsharp masking, a method where a blurred version of the image is subtracted from the original image, and canny edge detection is used to detect contours. The contours are added to the sharpened image to create an enhanced image, followed by a parallel process. On one hand, the gradient of the enhanced image is determined using gradient filtering, denoted by SF in the image. On the other hand, binarization is performed using a given threshold, for which, again, Otsu's threshold is often used, followed by the computation of the distance transform to determine the distance of each pixel to the nearest pixel with a value of 0. Next, Gaussian filtering is done to smooth the distance transform and extended maxima detection is used to establish where the markers are placed. Essentially, this step places a marker at each local maximum, so the farthest points from pixels with the value 0. The markers indicate that a grain is located at that coordinate in the image. Some of these local maxima are removed based on an input value. The markers are combined with the gradient bringing the parallel processes together. Finally, the watershed transform of the combined image is taken and binarized using Otsu's threshold. The input for the watershed transform is the image with the markers and the gradient. At the location of the markers, the pixel value is 0, so the watershed method begins filling the depth map generated by the gradients at these locations. As the "water level" rises and passes over the ridges formed by the gradients, and encounters "water" from a different source, a different marker, a boundary is drawn along the points of contact.

Each segmentation method described above results in a binary image that ideally consists of a number of grains in white, separated by black space. Classification is then performed as the fourth step to extract the shape properties and contours of each grain in the image since they should now be clearly detached. Lastly, unwanted objects are deleted. This includes grains that are touching the border of the image and grains that have properties above or below certain thresholds that the user can decide, such as grain size or circularity. The remaining grain data can be exported for further analysis.

All in all, PADM is a tool designed specifically to segment and classify sand grains in images taken using a microscope and determine their shape properties, which makes this algorithm very useful for this research.

Python adaptation of the PADM algorithm

The decision to use PADM still left substantial room for development. While the algorithm was a good base to start with, the only available version was in MATLAB using a GUI. The GUI made the implementation of different settings easier, but various settings in the program were hard-coded to match the uses of the designer. For example, the tool was designed for square 1024x1024 pixel images, which distorted the image in the GUI and resulted in contours that were misplaced. This effect can be seen in Figure 3.13, where the large contour on the left image corresponds to the light grain in the top left corner clearly indicating the translated contour placements.

Furthermore, the existence of the GUI prohibited the automation of the analysis to allow for the study of the large quantity of images taken during the experiments. The changes that would have had to

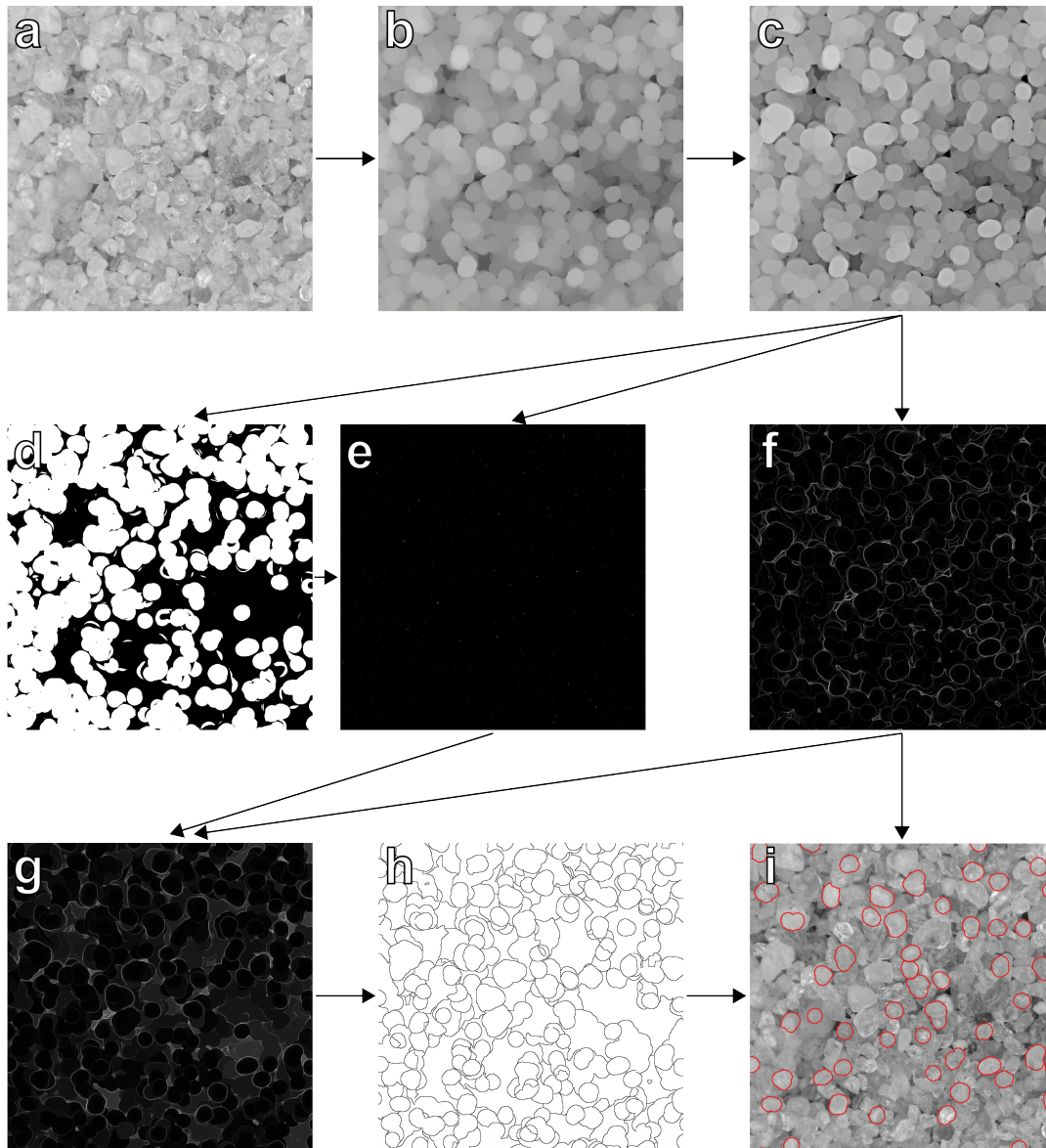


Figure 3.12: Overview of the segmentation and classification steps of PADM for medium sized grains. **a)** Input image f . **b)** Opening of f , $g_1 = \gamma_{19}(f)$. **c)** Sharpening of g_1 , $g'_1 = SH_9(g_1)$. **d)** Binarization of g'_1 , $h = BIN_{otsu}(g'_1)$. **e)** Markers MS (Note the small white dots). **f)** Gradient of g'_1 , SF . **g)** Markers MS with SF contours. **h)** Segmented image. **i)** Detected particles.

be implemented using MATLAB were deemed to be more work than rewriting the algorithm in Python, so the latter was chosen.

Both the publication and the MATLAB implementation were used to make the algorithm, since both sources contained at times confusing or missing steps, but together they provided a relatively clear picture. The program was built using the OpenCV and Skimage packages (Bradski, 2000; Van der Walt *et al.*, 2014).

The biggest difference between the developed version and the original version is in the first steps, as shown in Figure 3.11. The background procedure was completely removed and the filtering step was simplified to only one option. The background procedure, the classification of the type of image based on the noisiness of the background and the brightness of the grains, was omitted due to the images analyzed for this research being very similar and due to the unclear distinction between particles and background, thus leading to a noisy background. In the case of a plain background, it would be subtracted from the image, while in the case of a noisy one, a structuring disk would be used to



Figure 3.13: Comparison of output results of PADM, with on the left the MATLAB implementation and on the right the Python implementation developed for this research.

smooth the image. Not implementing the background procedure resulted in only one possible filtering step instead of four, so a noisy background was assumed, and the size of the structuring disk was determined based on the optimization procedure further elaborated upon after the presentation of the implementation of the algorithm in Python.

For the segmentation steps some minor changes were implemented. While binarization remained the same, the canny edge detection was slightly altered. An option to perform Gaussian blurring prior to the edge detection step was implemented. In the MATLAB version of the algorithm, Gaussian blurring is built into the function used for Canny edge detection, which is not possible in Python when using the OpenCV package. Gaussian blurring or smoothing helps reduce noise and was originally part of the Canny edge detection process (Canny, 1986). In the original implementation, there is no further information on whether this step is used, which is why it was added as a possible option. This same difference was also implemented in the watershed method. Furthermore, after the first binarization, no filling was performed, as this created too large shapes by combining multiple grains. The combination of the gradient of the image with the markers was done by imposing the minimum of the two on the final image, which is in line with the MATLAB version, while in the original it is not mentioned how the parallel processes are combined.

In the selection step, objects were deleted if they touched the border, as the grains may be incomplete. Furthermore, lower and upper grain size filters were implemented to allow different settings to be used for different grain sizes, along with a lower circularity filter to remove angular artifacts that often arose with the watershed segmentation method. The grain sizes were determined by their equivalent diameter, the diameter of a circle with the same area as the grain, while the circularity was computed using Equation 3.4, with A the area of the grain and P its perimeter.

$$Circ = \frac{4\pi A}{P^2} \quad (3.4)$$

In the final step, the orientation, location, circularity and elongation of the grains were added as extra data output. The orientation and elongation were those of an ellipse with the same second moment as the grain. The long-axis orientation could not be directly extracted and was added in post-processing, which will be described in the next subsection.

Settings optimization

With PADM working, the next step was to determine viable settings for the algorithm. The optimization of the PADM input settings consisted of multiple steps. First, the grains were divided into three classes based on their size using their equivalent diameter. The classes with their corresponding grain sizes and percentages of the total population can be seen in Table 3.6. The classes were chosen with the idea that the largest part of the population, the medium grains, would be analyzed using one set of settings, with the small and large grains representing a smaller fraction of the total population. In the end, the lower boundary of the small grains was raised significantly as smaller grains were of equal size to artifacts on the images, resulting in many false positives. This resulted in a relatively small domain.

Table 3.6: Grain size classes.

	Small	Medium	Large
Equivalent diameter range [pixels]	30-40	40-70	70-150
Equivalent diameter range [μm]	129-172	172-301	301-645
Percentage of population QICPIC [%]	15	75	10

Then, for each size class viable settings were determined. An overview of the available settings and their chosen values based on the optimization can be seen in Table 3.7. The eleven settings were optimized both quantitatively and qualitatively, through a combination of testing different settings and comparing the total number of detected grains, and visually inspecting the determined grain contours.

Table 3.7: Overview of used settings for the Watershed segmentation method.

Process	Available Input Settings	Small	Medium	Large
Filtering	Opening disk radius	5	19	23
Sharpening	Sharpening radius	7	9	11
Canny	σ_{blur}	1.6	0.4	2.2
	Upper threshold	Otsu's	Otsu's	Otsu's
	Lower threshold	Otsu's/3	Otsu's/3	Otsu's/3
	Aperture size	5	3	3
Binarization	Binarization threshold	Otsu's	Otsu's	Otsu's
Gaussian Filtering	Kernel size	0	5	0
	σ	0.5	1	7
Extended Maxima	Height maxima suppression	0.01	0.005	0.01
Circularity	Lower threshold	0.75	0.75	0.75

The values for each setting were compared either individually or in pairs, depending on the expected influence of the settings. Six comparisons were made for each grain size. The comparison was done by varying the one or two settings that were being inspected. The goal of this optimization was to find settings that provided useful results, with correct detections and statistically relevant numbers of detections; hence the combination of qualitative and quantitative assessment. Since the qualitative part was done by examining contours by hand, the settings are likely not the absolute best, but viable nonetheless.

Below, one of the 18 processes, the comparison of opening and sharpening radii for medium grains, will be elaborated upon. The others are presented in Appendix B. Discrepancies found in the number of detections in the Appendix are due to the raise of the lower limit of the small grains as discussed previously. The lower limit for the grain size was raised from 10 to 30 pixels when it was determined that many of the detections were artifacts and not grains. One of the 18 setting optimization steps is shown below in Figure 3.14. It can be seen that the combination that leads to the most detections is an opening radius of 19 and a sharpening radius of 9. Upon visual inspection of the contours created by these settings, and comparison of other combinations near this one, it was determined that these were indeed the best. However, for the small grains, the optimum is shown at opening radius 15 and sharpening radius 7, while the final settings were 5 and 7, respectively, as shown in Figure B.3. It was found upon visual inspection that the large opening radius resulted in more than a hundred incorrect detections. The opening radius was so large that the often sharply shaped smaller grains were reduced to circles and ellipses, and smaller grains were grouped together more often. To this end, the parameter space with smaller opening radii was investigated.

In a similar manner, the following combinations of settings were compared for each grain size class:

- Opening disk and sharpening radii

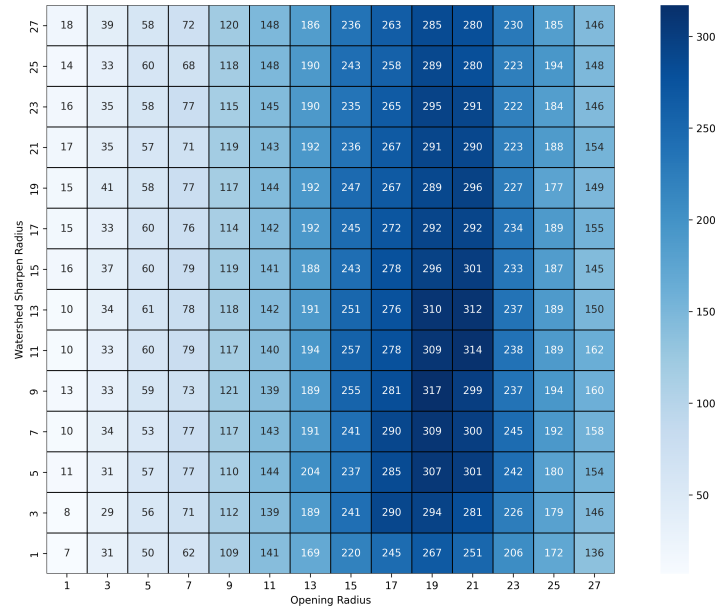


Figure 3.14: Number of detected grains for different opening and sharpening radii combinations for medium grains.

- Canny upper and lower thresholds
- Gaussian blur σ and aperture sizes
- Binarization thresholds
- Kernel sizes and σ for Gaussian Filtering
- Minimum height of the extended maxima suppression

The opening disk radius refers to the radius of the opening disks shown in the second image of Figure 3.12. The sharpening radius affects the σ of the Gaussian Filter used to blur the image that is then subtracted from the original image to sharpen it. For the Canny step, values above the upper threshold are marked as "strong" edges, values between the thresholds are "weak" edges and values below the lower threshold are neglected. "Strong" edges and "weak" edges adjacent to "strong edges" are pixels marked as edges. The σ of the Gaussian blur refers to the σ of the Gaussian Filter used to blur the image before Canny edge detection, while the Aperture Size signifies the size of the Sobel operator used for the Canny edge detection. The Sobel operator is a filter of size [Aperture size x Aperture size] that determines the gradient of an image. The binarization indicates the minimum pixel intensity for which a pixel is given the maximum value, in this case 255, while pixels with intensities below the minimum pixel intensity are given the value 0. The kernel size and σ for the Gaussian Filter refer to the size of the filter [Kernel size x Kernel size] pixels, and the standard deviation of the filter, respectively. Lastly, h , or the minimum height of the suppressed maxima, signifies the height difference maxima should have compared to their surroundings to be included (Soille, 1999). All maxima that do not qualify are removed.

After determination of the optimum settings, the same process was repeated for a second image to ensure the settings were not overly optimized for only one case and were also applicable to other similar images. These results are also shown in Appendix B. To save time, the results were evaluated only quantitatively. In almost all comparisons, the optimum settings were either exactly or nearly the same. If this was not the case, the significance of the difference was examined. The number of grains at the optimum settings, n_{opt} , was compared for both images together with the maximum number of grains, n_{max} for both images. If the difference between n_{opt} and n_{max} was similar, it was deduced that the variation was acceptable, as this would indicate that the effect of the settings on the number of detected grains is similar for both images.

After determination and verification of the optimum settings, all images of each experiment were

processed using the three sets of settings, resulting in three outputs per image, one for each grain size class.

3.3.3. Post-processing and data analysis

With all images processed using different settings for small, medium and large grain detection, the next steps are post-processing of the acquired data and data analysis. The output of the PADM version that was used was a list of coordinates corresponding to the contours of each grain and a dataframe containing various shape properties presented in Table 3.8. The label is a unique number given to every shape during classification. The ellipse parameters correspond to the properties of an ellipse that has the same second moment around the x and y axis as the grain. y_c and x_c refer to the coordinates of the centroid of each grain.

Table 3.8: Overview of the shape parameters that are the output of the PADM algorithm.

Stored shape parameters										
Label	Equivalent diameter	Perimeter	Area	Minor axis ellipse	Major axis ellipse	Orientation ellipse	y_c	x_c	Circularity	Elongation ellipse

Post-processing

In order to properly process the data, duplicates that arose as a consequence of analyzing each image multiple times with different settings had to be removed, and the long-axis orientation and elongation had to be determined.

For the duplicate removal, first the hierarchy of most correct to least correct grain class was determined, followed by the application of this filtering on identified duplicates. Four randomly chosen images were compared by plotting all contours of all size classes onto the image. It was then determined for each instance of overlapping contours which size class was correct. The comparison and the images that were analyzed are shown in Appendix C. The final result is shown in Table 3.9 below. It can be seen that the smaller grain class performed better, although especially for the Large-Medium comparison there were many inconclusive results. Inconclusive results are when both contours are incorrect, both are correct (for example a smaller grain is lying on top of a larger grain), or it is not possible to determine which one is correct.

Table 3.9: Number of correctly contoured grains by each grain class settings for four images.

Comparison	Larger correct	Smaller correct	Inconclusive
Large - Medium	20	23	28
Medium - Small	7	16	3
Large - Small	0	1	0

For every small grain, it was determined if the centroid lay within the equivalent radius of a medium grain, from the centroid of that grain. In other words, it was checked if the centroid of a small grain was within the contours of a circle with roughly equal size to the larger grain. If that was the case, the larger grain was removed. This process was repeated for the small-large duplicate removal and for the medium-large duplicate removal. Now only grains that were not overlapping remained.

Next, the long-axis, the long-axis orientation, grain width and elongation were determined. To this end, each individual contour, consisting of a set of coordinates was examined as presented in Figure 3.15. The longest possible line connecting two coordinates was identified as the long-axis and its orientation was determined. The coordinates of the contour were rotated over the long-axis orientation so the long-axis was vertical, creating a new coordinate system. The minimum and maximum x' coordinates were used to determine the width of the grain and, finally, the elongation was computed by dividing the long-axis by the width. These four parameters were saved along with the parameters presented in Table 3.8 and this process was repeated for each grain in each image.

Finally, the shape parameters for each grain size were combined for each image, resulting in 21 dataframes per experiment.

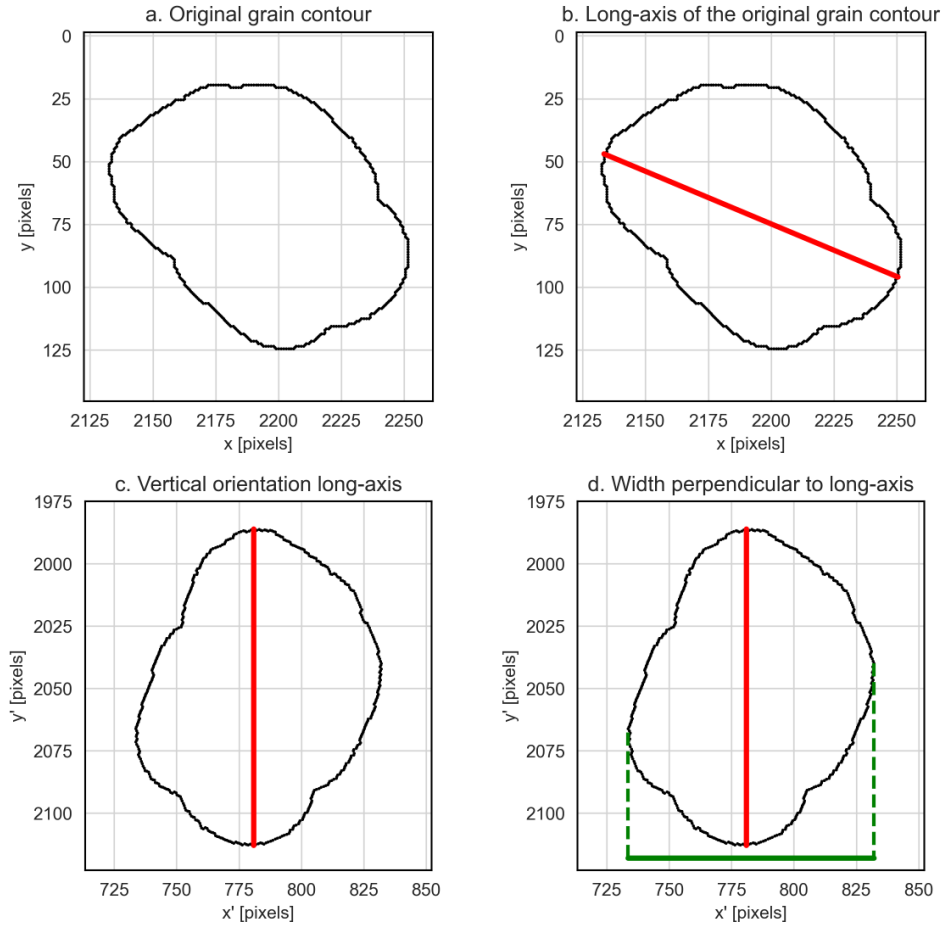


Figure 3.15: Determination of long-axis and corresponding width for a detected sand grain. **a.** The original grain contour. **b.** The long-axis in red. **c.** The grain rotated over the long-axis orientation so the long-axis becomes vertical. **d.** The width perpendicular to the long-axis in green.

Data analysis

The main quantifiable parameters describing preferred orientation are the fabric strength, R , discussed in chapter 2, and the preferred orientation itself, in this case specified as the angle of the long-axis clockwise positive from the vertical axis. R is computed using Equation 3.5 with C and S found with Equation 3.6 and Equation 3.7. The preferred orientation, x , is computed using Equation 3.8. The equations are further elaborated upon in chapter 2.

$$R = \sqrt{\left(\frac{C}{n}\right)^2 + \left(\frac{S}{n}\right)^2} \quad (3.5)$$

$$C = \sum_{i=1}^{18} f_i \cos(2\alpha_i) \quad (3.6)$$

$$S = \sum_{i=1}^{18} f_i \sin(2\alpha_i) \quad (3.7)$$

$$x = \frac{1}{2} \tan^{-1}(S/C) + K \cdot 90^\circ, \text{ with } K = 0 \text{ or } 1 \quad (3.8)$$

For each of the 21 images per experiment, the fabric strength and preferred orientation were determined. This process was carried out for grains with an elongation of 1.1 or larger, similar to the work of de Vet, 2013. This elongation was chosen since a clearer signal is shown for larger elongations, but the number of grains reduced drastically. The results are presented in the next chapter.

3.3.4. Analysis pipeline

The idea of the implementation of PADM in Python was increased automation. To that end, the program was adapted to analyze every image of each experiment using multiple sets of settings per image. This allowed for the optimization of the settings for different grain sizes, increasing the performance of the segmentation, both in terms of the number of detected objects and in correctness of the detections. A high-level block diagram of the entire image and data analysis pipeline is shown in Figure 3.16.

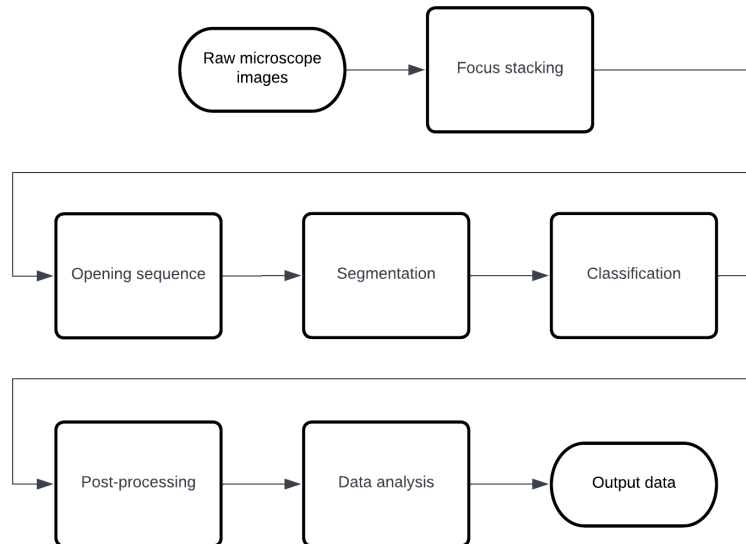


Figure 3.16: High-level block diagram of the grain detection tool.

All steps after the focus stacking, which was done using Helicon Focus 8, were automated using Python. The opening, segmentation and classification fall under the PADM algorithm, while the post-processing and data analysis were developed separately and specifically for this research.

4

Results

The PADM algorithm and subsequent post-processing steps resulted in shape and location data for each classified grain, and the contour of each grain. The filtered contours can be seen in Figure 4.1. It is clear that most grains fall in the medium size class (red), while the large (blue) and small (green) size classes are less represented.

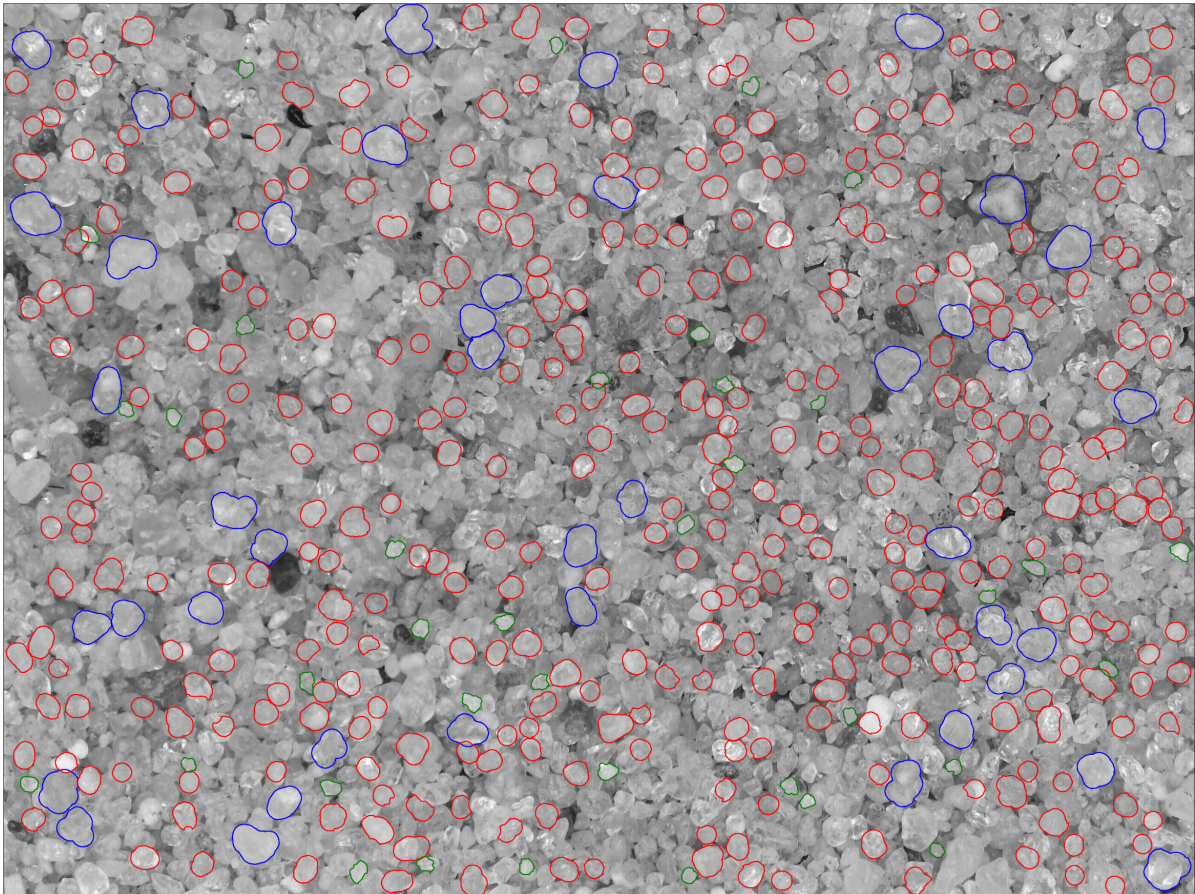


Figure 4.1: Segmented and classified grains from the experiment at ambient pressure and 150% u_{st} . The blue, red and green colors indicate the large, medium and small grain sizes, respectively.

The results of the separate analysis for each grain size class in the above image are shown in Table 4.1. Clearly, the medium size class contains most grains, about 82%, reduced to 76% when only taking into account grains with an elongation of 1.1 or higher. Interestingly, the relative reduction of number of

Table 4.1: Overview of data obtained from Figure 4.1.

Grain size class	Large	Medium	Small
Equivalent diameter	129-172 μm	172-301 μm	301-645 μm
Number of grains	43	367	37
Number of grains with elongation ≥ 1.1	38	220	33
Preferred orientation	101°	110°	114°
Fabric strength	0.188	0.033	0.262

grains when using this elongation as a lower limit varies greatly between the size classes. The large and small classes lose about 11%, while the medium class loses 40% of its population. This means that many of the medium grains are detected as very highly spherical, as defined by Figure 2.4, or not elongated. This could be due to the relatively large opening radius that was used for the medium grain size. As disks with a radius of 19 pixels, as shown in Table 3.7, so a diameter of 38 pixels, were used to construct shapes corresponding to grains with an equivalent diameter of 40 to 70 pixels, it is likely that the grains were made to appear more spherical during the opening step of the segmentation. On the other hand, the relatively small reduction in number of grains for the small and large grain size classes would either indicate that these sizes have fewer highly spherical grains, or that the smaller radius relative to the equivalent diameter is more successful in accurately portraying the correct elongation of the grains.

4.1. Grain orientations

The orientation of the long-axis of each grain with an elongation of 1.1 or higher in Figure 4.1 was used to construct a windrose. A windrose is a circular histogram, showing the number of instances of orientations that fall in predetermined bins. The windroses used in this research represent grain orientations in one of 9 bins, each with a width of 20°, mirrored about the origin. Unlike the research of Dapples and Rominger (1945), the end-position was not used to determine the orientation of the grain. Instead, the orientation of the long-axis was used, which is why the windroses are symmetric about the origin. One such windrose was constructed for each grain size class of Figure 4.1, shown in Figure 4.2. The flow in the wind tunnel in this and all subsequent windrose images is along the North-South line. The preferred orientation of the size classes varies by no more than 10° from each other, but clearly the medium size is statistically much more relevant due to the larger population. Interestingly, the medium and large grains have a strong signal almost perpendicular to the preferred orientation.

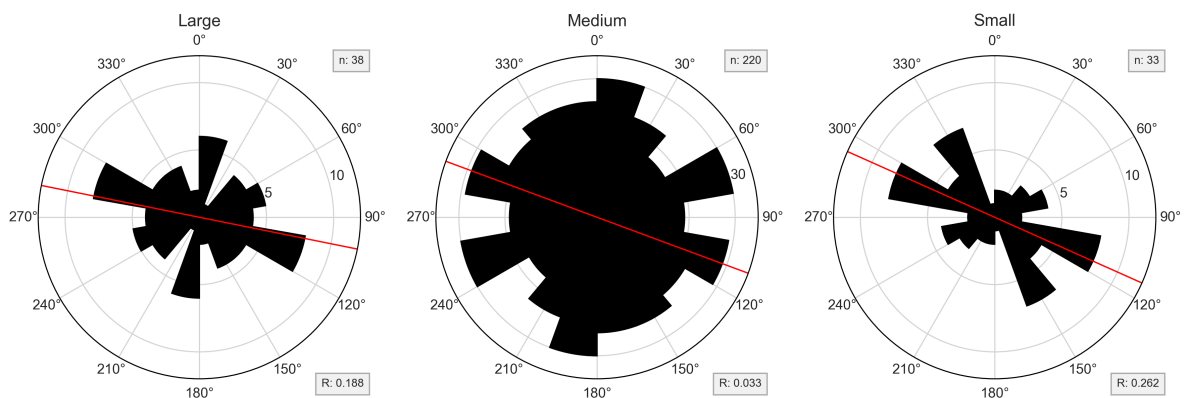


Figure 4.2: Windroses for each size class. Note the smaller range for the large and small grains, which was decreased for better visibility. n and R indicate the number of grains and fabric strength, respectively. The red line indicates the preferred orientation.

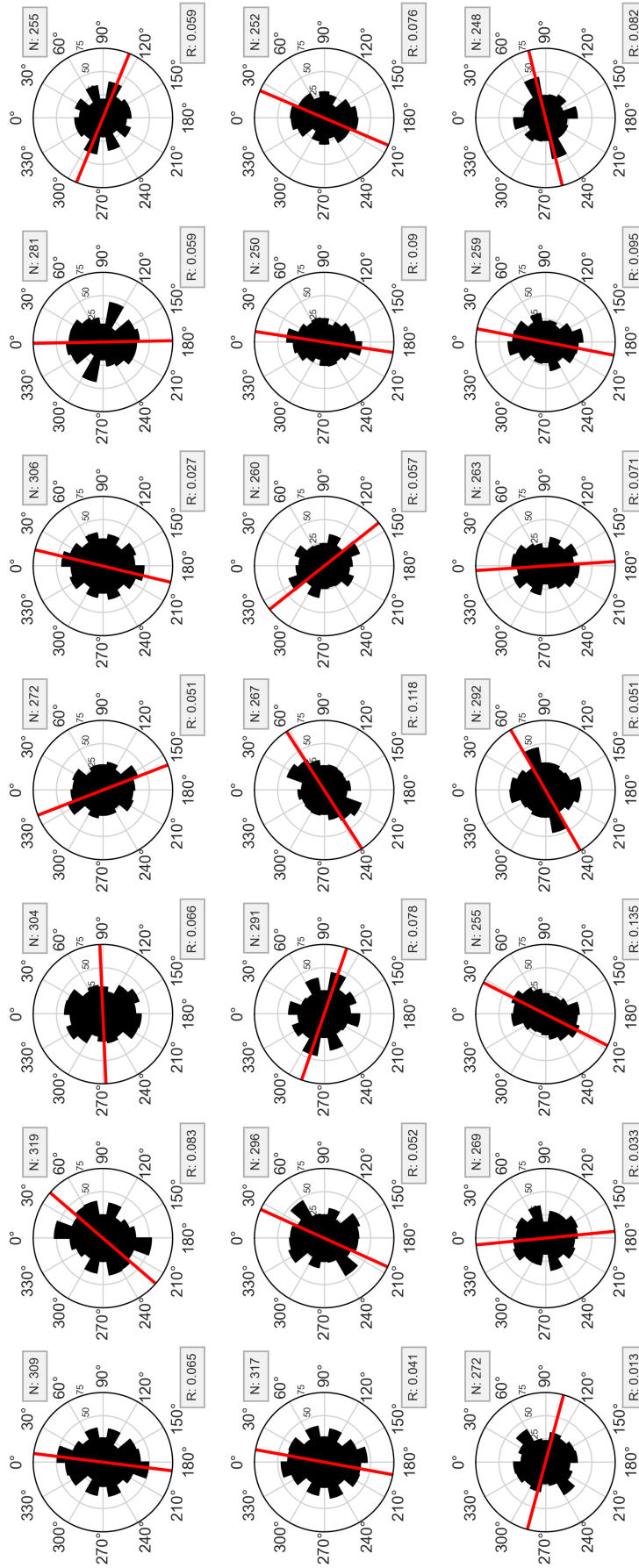


Figure 4.3: Grid of windroses of the experiment under ambient pressure at 150% u_{4t} . Each windrose describes the orientations in one image, with the grid corresponding to the physical grid of images taken in the wind tunnel. The red line coincides with the determined preferred orientation. N and R are the number of grains and the fabric strength, respectively.

Combining the data of all grain size classes yields one windrose for all detected grains of an image. This process was performed for each of the 21 images taken per experiment, and a grid of the wind roses corresponding to their measurement locations was constructed. The grid can be seen in Figure 4.3. The flow in the wind tunnel moves vertically over the grid. A physical representation of the sampling locations of the grid is shown in Figure A.1. The third windrose from the left on the second row is deduced from the data in Figure 4.1. In most windroses, a preferred orientation is visible, based on the distribution of the grain orientations. The red lines show the mathematically determined preferred orientation, based on bins of 10° , as specified in Equation 3.8. Due to the nature of Equation 3.8, the orientation is determined per quadrant, and 90° were added to let the orientation coincide with the quadrant that contained the most grain orientations. The red lines do not seem to reliably coincide with the flow direction of the wind tunnel. Specifically, out of the 21 images, 9 had a preferred orientation within 15° of the wind flow direction, 13 within 30° and 15 within 45° , leaving 6 with a deviation larger than 45° .

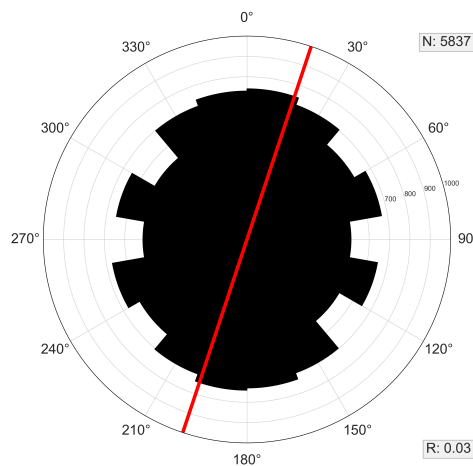


Figure 4.4: Windrose of the experiment under ambient pressure at $150\% u_{*t}$. This figure shows the combined orientations of all 21 measurements. The red line coincides with the determined preferred orientation. N and R are the number of grains and the fabric strength, respectively.

When all grain data of one experiment are combined, Figure 4.4 is obtained. The windroses for the other experiments can be found in Figure E.1 and Figure E.2, in Appendix E. The distribution over the bins becomes a bit more uniform than for the individual images, which would indicate small-scale effects affect the preferred orientation in the images. Indeed the fabric strength of 0.03 is lower than the average fabric strength of the windrose grid, which is 0.07. In comparison, de Vet (2013) found values for the fabric strength ranging from 0.01 to 0.24 for grains of elongation 1.5 and higher studying thin-sections, which consist of clear grain boundaries. Using microscope images of Martian sediment, taking into account grains of elongation 1.1 and higher they found R values ranging from 0.10 to 0.17. These values are for individual images.

For the combined windrose of each experiment, the preferred orientation of seven out of 10 experiments was within 10° of the expected flow direction in the wind tunnel, with only one experiment deviating by more than 30° , the experiment under Mars equivalent pressure at $150\% u_{*t}$. These results can be seen as the red line, indicating the preferred orientation in Figure E.1 and Figure E.2. This means that for most cases, the estimation of the wind direction based on the orientation of the sand grains with an elongation of 1.1 or higher would fall within 10° of the actual wind direction if the results of multiple images in a general area would be used. The increased alignment of the preferred orientation to the wind flow in the combined case versus the case of individual images seems to be an effect of small-scale disturbances, such as ripples. This effect is more pronounced in individual images, as for the combined case the random noise due to disturbances becomes less significant.

4.2. The effects of pressure and velocity on fabric strength

If the images of each experiment are processed individually, and the average fabric strength per experiment is plotted against the pressure for both wind speeds, the top image of Figure 4.5 is obtained when taking into account only grains with an elongation of 1.1 and higher. The full range of fabric strengths determined for each experiment can be found in the lower image of Figure 4.5.

For the higher shear velocities, at 150% of the threshold, as the pressure increases, so does the fabric strength. For the lower shear velocities, at 120% of the threshold, the same applies, but only for higher pressures. At 240 and 14 mbar, the fabric strength is higher than at higher pressures, even surpassing the fabric strength of the higher shear velocity.

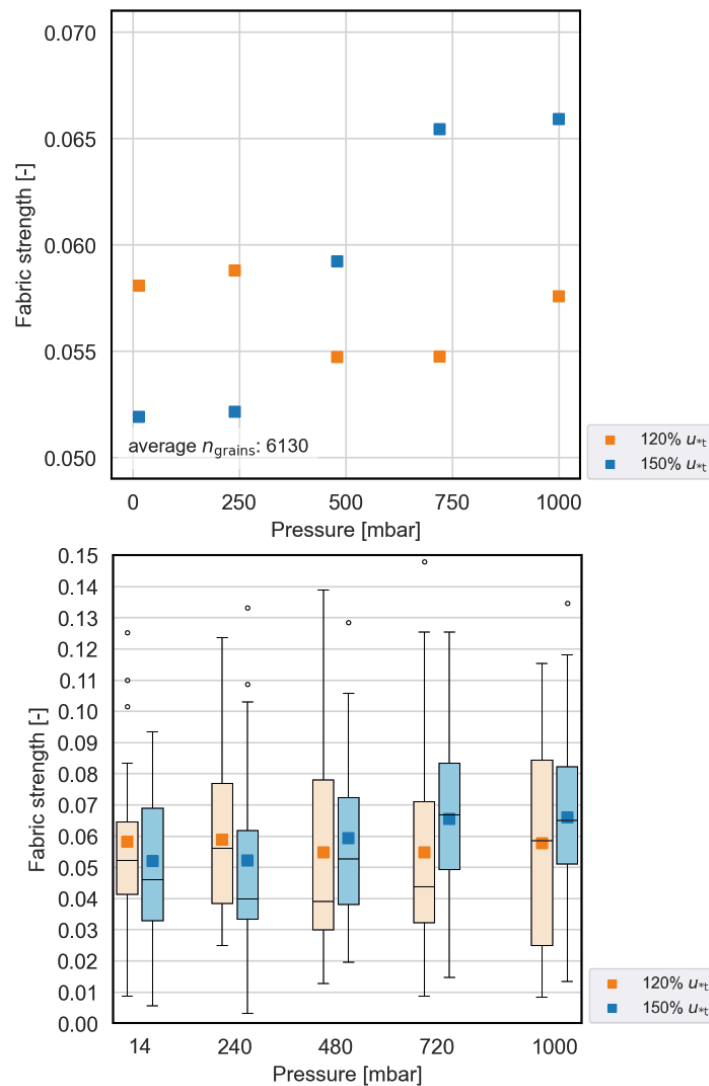


Figure 4.5: In the top image, the average fabric strength over all images for each experiment, for an elongation of 1.1 and higher. In orange at 120% of the threshold shear velocity and in blue at 150% u_{*t} .

In the lower image, box plots of the fabric strength of every image for each experiment, for an elongation of 1.1 and higher. For better readability the box plots are placed next to each other, with the squares indicating the respective average values as seen in top image.

This could indicate that at lower pressures, the randomization of grain orientation due to impacting grains is more prominent than at higher pressures. At higher pressures, the effect of airborne streamlining of particles would then be more visible in the orientations of the grains in the sandbed. At lower pressures, since the density is lower, a higher shear velocity is required to saltate the grains, this increased velocity then increases the impact speed of the sand grains, resulting in more splashed particles.

4.3. Grain shape parameters

The relationship between the two main shape properties relevant for this research, the equivalent diameter and the elongation is shown in Figure 4.6.

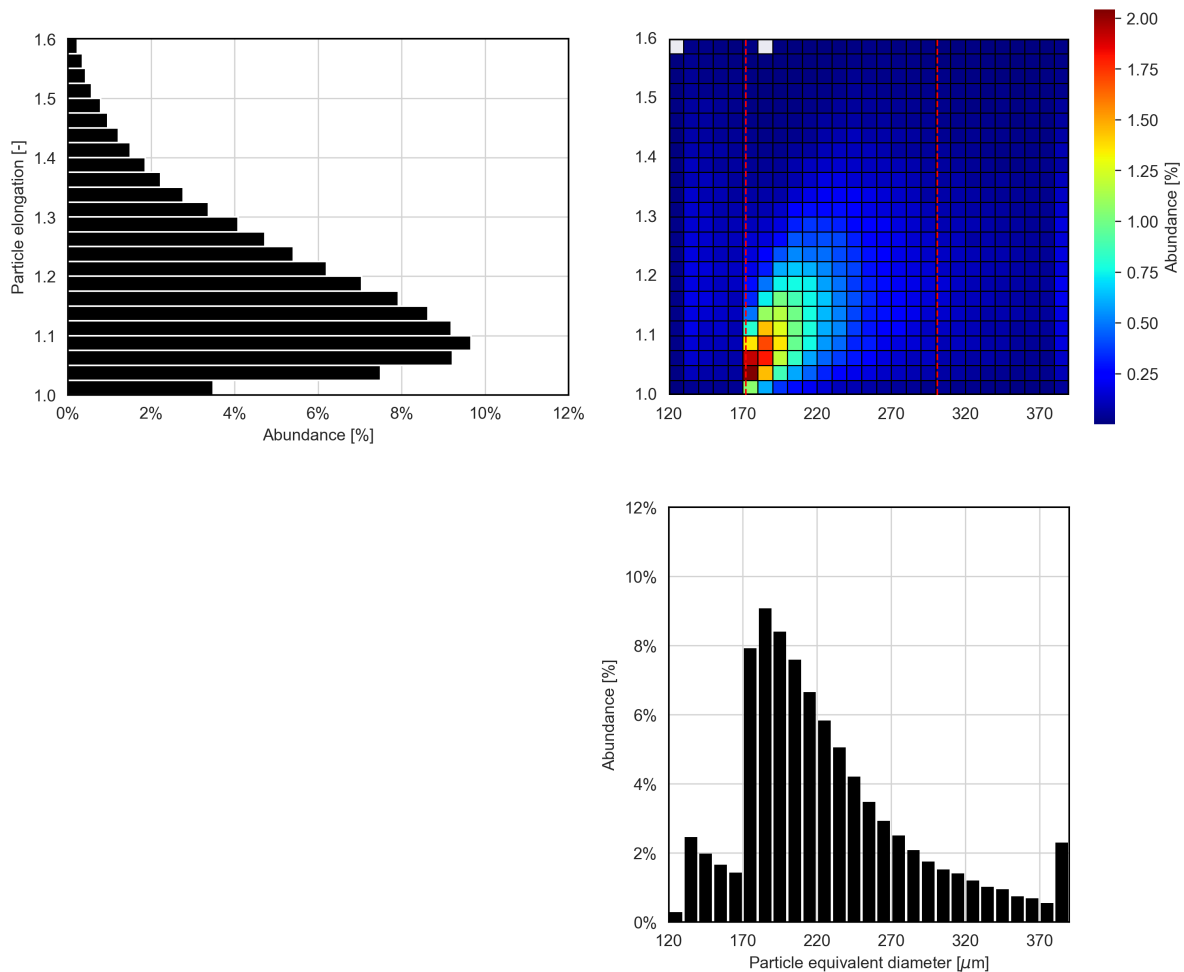


Figure 4.6: Overview of the particle elongation and equivalent diameter for all detected grains, 143530 in total. The gray cells in the heatmap indicate that no grains were detected. The red dashed lines coincide with the boundaries between the grain size classes, small, medium and large. All grains with an equivalent diameter larger than 390 μm were added to the rightmost column and all grains with an elongation greater than 1.6 were added to the top row.

The heatmap is a percentual representation of the total population of detected grains for all the experiments studied combined, totaling 143530 grains. Grains with an elongation larger than 1.575 have been grouped in the row for representing elongation 1.575-1.600, and grain sizes exceeding 380 μm have been grouped in the column representing 380-390 μm . From the heatmap, it follows that most of the grains have an elongation between 1.0 and 1.2, with an equivalent diameter ranging from 170 μm to 230 μm , approximately 40% of the total population. Noteworthy is the sharp difference between the sizes below and above 170 μm . This size coincides with the switch from small to medium grains in the segmentation process. Different sets of settings were used for each size class, which could have impacted this sudden change. The optimum settings determined for the smallest grain sizes likely underperform, resulting in this sharp change. Lastly, it can be seen that there is a general tendency for larger grains to have a larger elongation. This can be a result of smaller grains being a product of more erosion than larger grains, but studies have not shown that there is a relationship between grain size and grain shape consistently (Das & Ashmawy, 2007).

4.4. Validation of results

Two parts of the research were validated. On one hand, the results of the PADM algorithm were compared to the results of the QICPIC dynamic image analyzer to investigate the performance of the image analysis. On the other hand, the threshold shear velocities for the experiments were explicitly determined and compared to their expected relationship.

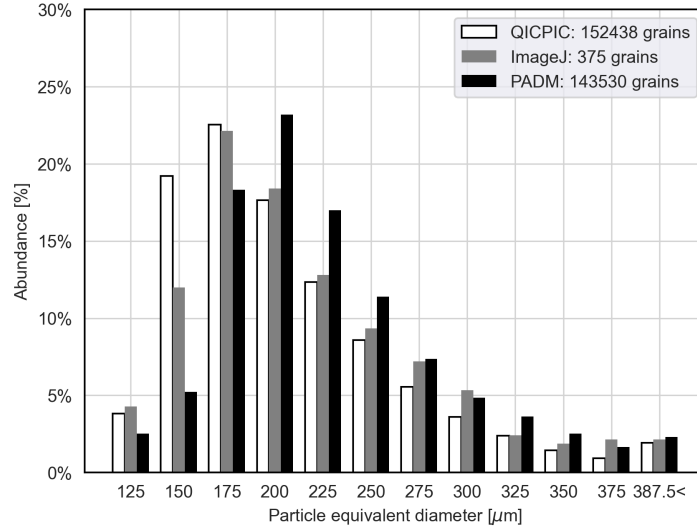


Figure 4.7: Histogram of detected particle sizes for ImageJ, QICPIC and PADM measurements. The upper and lower boundaries for grain sizes were set at the upper and lower boundaries of PADM to keep the range the same.

In Figure 4.7 the histograms of the equivalent diameter for the ImageJ and QICPIC measurements, and the PADM results are shown. It can be seen that the population of grains detected by PADM is skewed towards larger grains compared to ImageJ and QICPIC. The sharp increase between the 175 μm and 200 μm for PADM roughly coincides with the boundary between the small and medium grain size classes. This means that either the algorithm and deduced settings underperform when it comes to smaller grains, or that fewer smaller grains are visible in the images than there are present in the sediment. Larger grains may have laid more on top of the sandbed than smaller grains which could have settled more in-between other grains, resulting in larger grains being fully in view and therefore being detected. Overall, the differences all fall within 5% with the only exception being grains with an equivalent diameter of around 150 μm .

The threshold shear velocities determined for the material used in the experiments at different pressures are presented in Figure 4.8. The threshold shear velocities are as expected following a roughly inverse square root distribution. According to the simplified version of the equation used to determine the fluid threshold, Equation 4.1, this is the expected result since in all experiments the gravity, particle diameter and particle density remained the same. In the equation, u_* denotes the shear velocity, A_{*t} is a constant dependent on the interparticle forces, the lift force and Reynolds number, ρ_p and ρ_a are the densities of the sand particles and the air, respectively, g is the gravitational acceleration and D_p is the particle diameter (Greeley & Iversen, 1985; Kok *et al.*, 2012). Now it is not very clear if the threshold determined for the experiments performed in Aarhus is the fluid or impact threshold, as the threshold was determined for a sediment with a wide range of grain sizes (63 to 500 μm) and the threshold was reached by gradually increasing the shear velocity, likely already inducing rolling or other forms of movement, especially in the smaller grains (Merrison *et al.*, 2007; de Vet *et al.*, 2014). This presumably reduces the required shear velocity needed to reach saltation.

$$u_{*t} = A_{*t} \sqrt{\frac{\rho_p - \rho_a}{\rho_a} g D_p} = A_{*t} \sqrt{\left(\frac{\rho_p}{\rho_a} - 1\right) g D_p} \quad (4.1)$$

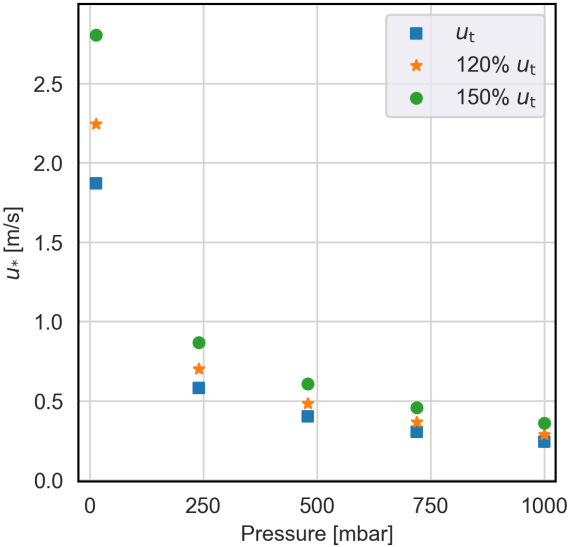


Figure 4.8: Fluid threshold for the sediment at different pressures, along with 120% u_t and 150% u_t .

5

Discussion

In this chapter results that are not directly part of the research will be presented, implications of the results on the research field will be discussed and recommendations for future research will be given.

5.1. The effects of grain elongation on fabric strength

The fabric strength, R , shown in Figure 4.5 differs depending on the minimum grain elongation taken into account. In general, it was found that for larger elongations, the average fabric strength increases, as can be seen in Figure 5.1. This indicates that more elongated grains align themselves better. The box plots of the fabric strength of individual images for each experiment, presented in Appendix F, show that this is indeed the case for all experiments, with the maximum, minimum and median values all generally increasing with elongation. This outcome can be used to determine a lower limit for the elongation that should be taken into account when studying the preferred orientation of grains in a sandbed, especially if the goal is to determine the flow direction of the wind.

However, the number of grains that are taken into account reduces substantially with each step, as shown in Figure 5.2. At an elongation of 1.1 already about a third of the grains is removed, resulting in an average R of about 0.06. If double that fabric strength would be desired, in theory leading to a clearer preferred orientation, an elongation of 1.3 or higher would be needed. However, this would result in roughly 75 grains per image, divided over the 18 bins used to calculate the fabric strength and preferred orientation, the results start to become statistically much less relevant. Thus, when determining a lower bound for the elongation, it is vital to ensure an adequate number of grains is used for a statistically relevant result. This is especially important for natural deposits such as on the surface of Mars, where it might be necessary to take a large number of images to ensure enough particles with the desired elongation are present since there is no control over the grain shape parameters.

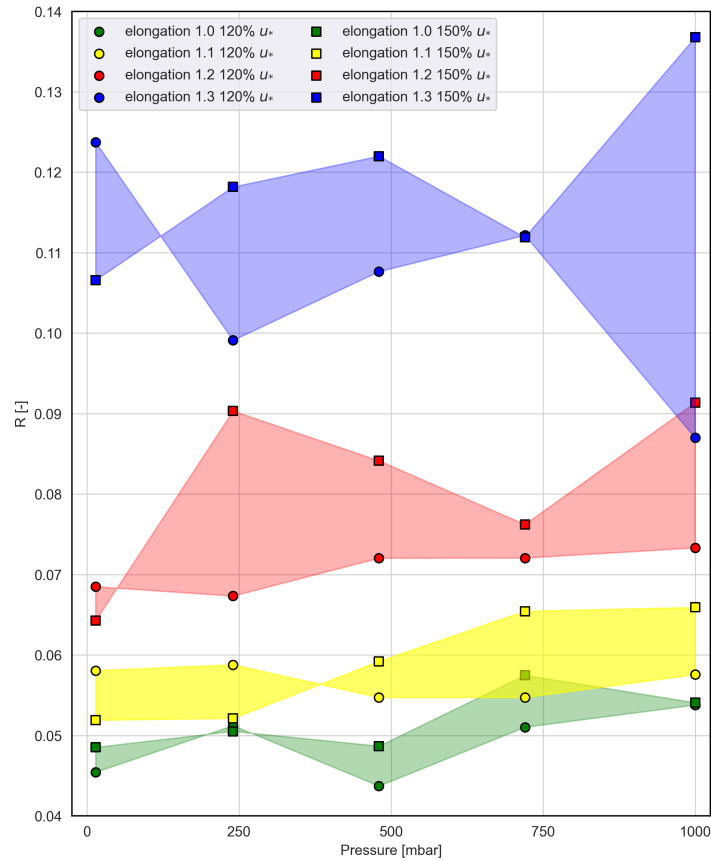


Figure 5.1: Average fabric strength over all images, for each experiment and for various elongations. The circles indicate 120% of the threshold shear velocity and the squares 150% u_{*t} . The colored areas only serve as a visual aid to highlight the datapoints that belong together. The yellow area corresponds to Figure 4.5.

The elongation of 1.1 was chosen as the main elongation to study since there are still approximately 300 grains per image, while any lower the correctness of the grain shape starts to become questionable. In Table 5.1 an estimation of the difference in number of pixels between the length and width of a grain at various elongations and equivalent diameters is shown. Since grains are irregularly shaped, as shown in Figure 3.15, an ellipse with the same area was used to approximate the grains of various sizes. The equivalent diameters coincide with the limits of each grain size class. While the particles are in reality more angular than an ellipse, they come from an aeolian-mature dune, so they are expected to be quite rounded, making an ellipse an acceptable approximation for this estimation (Bagnold, 1941). For approximately 75% of the grains, the difference between the long-axis and the width is four to seven pixels. While this is not a very large difference, an extremely high resolution would be required to have a more substantial difference for these grain sizes. Furthermore, the distribution of fabric strengths becomes increasingly sparse as the elongation increases, making the results less trustworthy. With the lower bound for elongation at 1.1 the box plot in Figure 5.2 shows a relatively small spread in fabric strength values, while a still-significant number of grains is taken into consideration. An overview of the number of grains and fabric strength for different elongations of all experiments can be found in Appendix F.

5.2. Threshold shear velocity and implications for Mars

From Figure 5.1 it follows that at low pressures the shear velocity for which the fabric strength is higher flips, with 120% u_{*t} showing more preferred orientation. This effect happens for multiple elongations, but the pressure at which the flip occurs is not consistent, with the flip happening somewhere between 14 and 480 *mbar*. However, it can be said that for the equivalent pressure on Mars, 14 *mbar*, lower shear

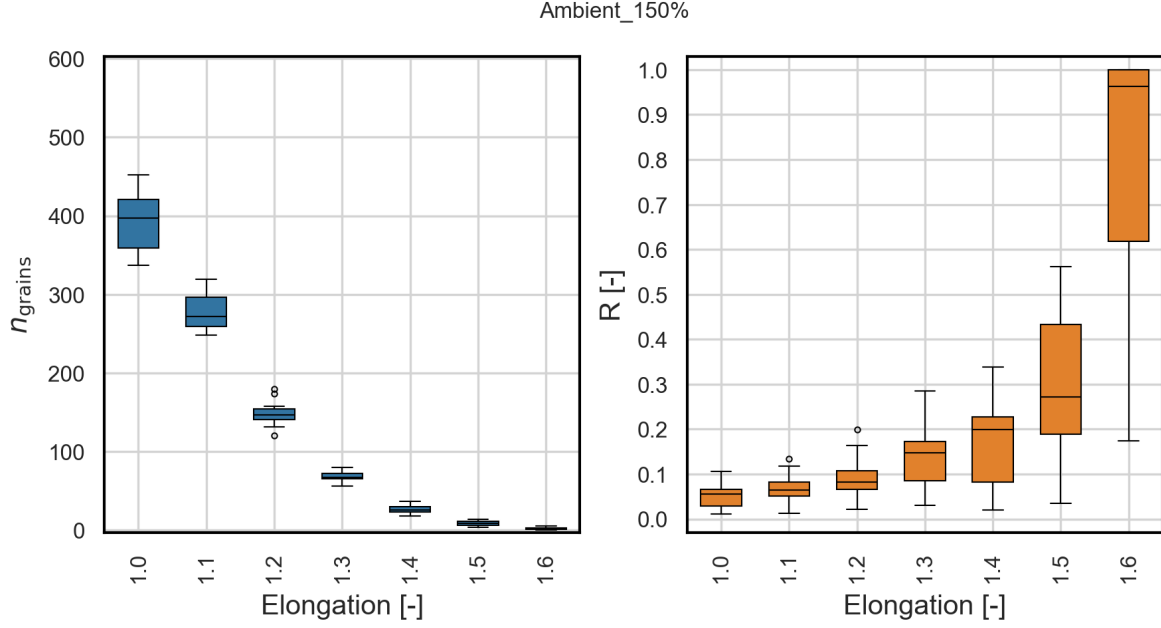


Figure 5.2: Box plots of the number of grains and fabric strength of the experiment under ambient pressure at 150% u_{*} , for 21 images. On the left, in blue, the number of detected grains per lower limit setting for the elongation, and on the right, in orange, the fabric strength.

Table 5.1: Difference between major axis and minor axis in pixels for an ellipse of different elongations and equivalent diameters.

Elongation \ Eq. diameter [μm]	Eq. diameter			
	129	172	301	645
1.0	0	0	0	0
1.1	3	4	7	14
1.2	5	7	13	27
1.3	8	11	18	39

velocities show a higher degree of preferred orientation than higher shear velocities. This means that the effect of preferred orientation likely diminishes at higher wind speeds.

Now, as mentioned in chapter 4, the randomization of the grain orientation due to impacting grains is expected to be larger at low pressures for higher velocities. Since the density is much lower at low pressures, the drag and lift forces are also smaller and require a higher shear velocity for saltation to take place. This increased wind speed results in grains impacting with a higher velocity, resulting in a higher number of splashed grains as per Equation 5.1 (Ammi *et al.*, 2009) and Equation 5.2 (Kok *et al.*, 2012). In the equation, \overline{N}_e denotes the mean number of splashed particles, \bar{e} and v_{imp} are the effective restitution coefficient and impact velocity, g and D denote the gravitational acceleration and diameter of the grain, while n_0 and ζ are fit parameters. For the second equation, N and a are the number of splashed particles and a proportionality constant, while m_{imp} and $\overline{m}_{\text{spl}}$ denote the mass of the impacting grain and the average mass of the splashed particles, respectively.

$$\overline{N}_e = n_0 (1 - \bar{e}^2) \left(\frac{v_{\text{imp}}}{\zeta \sqrt{gD}} - 1 \right) \quad (5.1)$$

$$N = a \frac{m_{imp}}{m_{spl}} \frac{v_{imp}}{\sqrt{gD}} \quad (5.2)$$

Ultimately, these results show that especially for shear velocities near the threshold speed preferred orientation is more pronounced than at higher velocities, where the effect of impacting grains induces significant noise by splashing grains at random orientations. It would be interesting to map this near-threshold domain further, to gain a clearer picture of the effect of shear velocity at Mars equivalent pressure. This could provide more information on the movement of grains near the threshold. For example, if the degree of preferred orientation starts reducing below a certain shear velocity, this could indicate the transition of type of movement from saltation to rolling. Furthermore, it would provide more information on the possibility of movement below the threshold.

5.3. The effect of gravity on the threshold shear velocity on Mars

Comparing the material and atmospheric conditions used in the experiment with those on Mars, the most significant difference is the gravitational acceleration. The densities of the air and grains also differ, as well as the chemical composition of both, with the grains on the Martian surface consisting mostly of basalt, while for the experiments quartz was used. These and other relevant parameters are shown and compared in Table 5.2.

Table 5.2: Environmental and material properties on Mars and in the wind tunnel.

Parameter	Mars	Mars analogue	Ratio	Sources
$g [m/s^2]$	3.7	9.8	0.378	(D. Williams, 2024)
Gas	CO ₂	Air	-	-
Temperature [K]	243	293	0.830	(Andreotti <i>et al.</i> , 2021)
R [J/kgK]	188.9	287.1	0.658	(Huber, 2023)
$\rho_a [kg/m^3]$	0.0189	0.0170	1.11	(Andreotti <i>et al.</i> , 2021)
$\rho_p [kg/m^3]$	3000	2700	1.11	(Ehlmann <i>et al.</i> , 2017) (Andreotti <i>et al.</i> , 2021) (Kozakiewicz <i>et al.</i> , 2023)
$\rho_a / \rho_p [-]$	$6.3 \cdot 10^{-6}$	$6.3 \cdot 10^{-6}$	1	-
$d_{peak} [\mu m]$	130	190	-	(Sullivan & Kok, 2017) (Kozakiewicz <i>et al.</i> , 2023)

As mentioned in section 3.2, similarly to Andreotti *et al.* (2021) ambient air was used in the experiments instead of CO₂. However, in order to obtain a similar medium density, a different air pressure was needed than one would encounter on Mars since the temperature and specific gas constants differ. Therefore, the pressure in the wind tunnel was not set to the pressure found at the surface of Mars, but at a value resulting in the ratio of medium density to particle density being the same as on Mars. The ratio of the densities can be seen in Table 5.2. This scaling of the pressure in the wind tunnel allows for the same aerodynamic forces to be active on the particles as would be the case on Mars.

The grain size distribution of the material used in the wind tunnel shown in Figure 4.6 differ slightly from the distribution found on Mars (Sullivan & Kok, 2017; Kozakiewicz *et al.*, 2023). Using the PADM algorithm it was found that the peak of the size distribution histogram of the quartz lay around 190 μm , while on Mars, again using PADM, it was found that one peak lay around 130 μm (Kozakiewicz *et al.*, 2023). The peak for the material on Mars lies near the lower limit of the tool's capabilities for the used images, but when comparing with the results from the dynamic image analyzer, shown in Figure 3.3, the peak lies near 150 μm . While the work of Kozakiewicz *et al.* (2023) studied a much larger size population than this research, grains sized 120 to 350 μm , roughly corresponding to the main population of the material used in the wind tunnel, are abundant on Mars.

Clearly, for the wind tunnel experiments, a higher velocity was needed at Mars equivalent pressure than would be necessary on Mars, where the gravity is about a third of that on Earth. However, grains on Mars are also expected to have higher saltation arcs, increasing their impact speed. The question is which effect is stronger at different shear velocities. It could be that this technique is useful to deduce the wind direction and wind speed only within a certain window of shear velocities. Since in the experiments it was found that the signal increases at lower shear velocities, this method is possibly beneficial at shear velocities near the fluid threshold, while the signal is insignificant for higher shear velocities.

It should be noted that the threshold found for Mars equivalent pressure, shown in Figure 4.8 does not take into account the different gravitational acceleration of Mars. When looking at Figure 5.3, it can be seen that the threshold, as determined in this study is similar to what is expected to be the fluid threshold on Mars, when looking at a grain size of $200 \mu\text{m}$. It should be noted that the threshold determined during the wind tunnel experiments might not exactly be the fluid threshold, but rather the lowest shear velocity for which saltation took place at a large scale. This likely falls between the fluid threshold and impact threshold, as movement already takes place below the fluid threshold. It was noted during the experiments that the threshold was consistently higher than expected, likely due to the moisture that was still present in the sand. This hypothesis was supported by the observation of multiple instances of off-gassing. Right after pumping the air in the wind tunnel to the desired pressure, the pressure would slowly rise by 0.5 mbar at the lowest pressure settings, which is an increase of about 4%. This was presumably due to moisture present in the sand, which evaporates at much lower temperatures at low pressures.

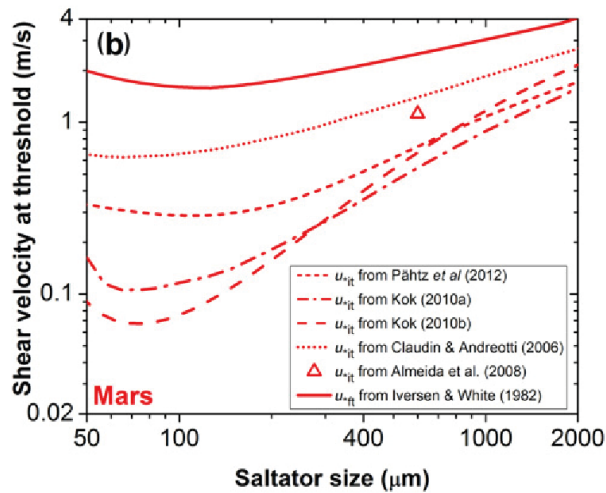


Figure 5.3: From Kok *et al.* (2012), Predictions of the fluid and impact thresholds on Mars.

In order to estimate which wind speeds would be necessary to reach the shear velocities used in the experiments, a detachment model can be used. Merrison *et al.* (2007) used experimental results at low pressure to establish an empirical expression for the threshold shear stress required for detachment of a sand grain. Detachment includes creep, or rolling, of grains as well as saltation. Their Equation 5.3 uses four terms to determine the threshold, one for gravity, interparticle or adhesion forces, lift and torque. This model differs from the one presented in subsection 2.1.1 mostly due to the inclusion of torque. The lift, adhesion and torque expressions contain the following empirically determined coefficients:

- Adhesion coefficient: $C_{adh} = 2.7 \cdot 10^{-5} \text{ N/m}$
- Lift coefficient: $C_L = 1.45$
- Torque coefficient: $C_T = 4.4 \cdot 10^4 \text{ m}^{-1}$

$$\rho_a u_*^2 \approx \frac{\frac{\pi}{6} g \rho_p d^3 + C_{adh} d}{C_L d^{1.93} + C_T d^{2.93}} \quad (5.3)$$

Given these coefficients, and the gravitational acceleration, density of the CO₂ atmosphere for a pressure of 9 mbar and temperature of -60°C and density of the basalt sand grains found on Mars, the threshold shear velocity for particles of different diameters can be estimated. Next, the free flow velocity was determined using Equation 5.4, with z the height above the sandbed and z_0 the surface roughness. In this case, similarly to Merrison *et al.* (2007), a height of 1.6 m and surface roughness of 3 mm were used.

$$U = u_* \cdot 2.5 \ln \left(\frac{z}{z_0} \right) \quad (5.4)$$

The resulting threshold wind speed curves for quartz sand and basalt were plotted, and can be found in Figure 5.4. The quartz curve corresponds to the work of Merrison *et al.* (2007), while the basalt curves are estimations of the required wind speeds on Mars to achieve detachment and to reach 120% and 150% of the threshold shear velocity. These basalt curves would correspond to the conditions of the wind tunnel experiments, but now including Martian gravity. These wind speeds are higher than the average wind speeds found on the red planet but are attainable during gusts (Viúdez-Moreiras, de la Torre, *et al.*, 2022; Viúdez-Moreiras, Lemmon, *et al.*, 2022; Stott *et al.*, 2025).

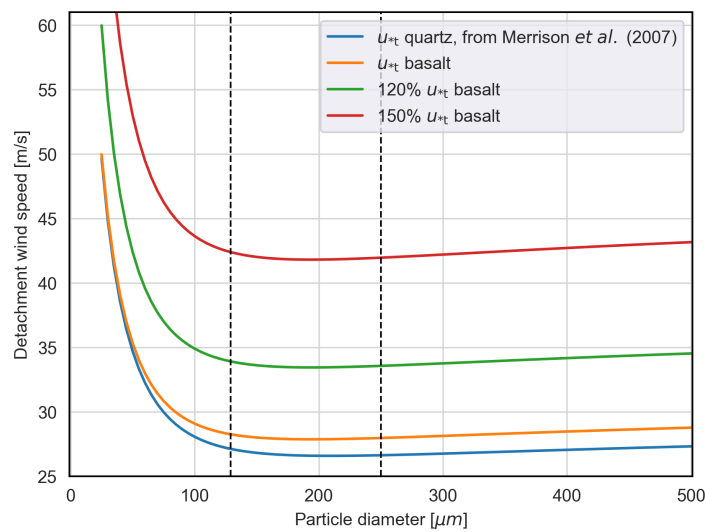


Figure 5.4: Expected wind speeds on Mars for the different conditions used in the experiment. These wind speeds were determined using real Martian conditions, so a CO₂ atmosphere, basalt as the material and Martian gravity. The left dotted line indicates the smallest particles detectable in this research. The right dotted line indicates the maximum diameter for which the estimated coefficients are definitely valid (Merrison *et al.*, 2007).

5.4. Recommendations for future research

As with any research, several complications arose during different steps of the project. This section aims to provide recommendations on how to prevent them and looks forward to possible next steps that can be taken.

The selection and preparation of sediment is crucial. While analyzing the microscope images it became apparent that it was often difficult to determine the edge of a grain. Grains of the same grayscale shade sometimes lay on top of each other, making it difficult to distinguish which part belonged to which grain. Furthermore, the quartz sand grains were semi-transparent. This resulted in grain boundaries sometimes running virtually through a different grain as it was still visible, resulting in a combination of boundaries from multiple grains being detected as one grain. Another issue was the glare on parts of grains due to the reflections of the light sources. As the grain surfaces were not homogeneous, some parts of the grains reflected the light differently than others and PADM would recognize these areas as separate grains. To combat this, the lower limit of the equivalent diameter was raised significantly to

129 μm , not taking into account a large portion of the population which is especially of interest as the minimum impact threshold is expected to lie near or below 100 μm for Mars, as can be seen in Figure 5.3. Both these issues can be, at least partly, resolved by using material that is opaque and less-reflecting. Based on images of the sand on the surface of Mars, it can be deduced that it is less transparent and reflective than the sand used in this experiment, as can be seen in Figure 5.5 and other works studying sand grains on Mars such as Sullivan and Kok (2017), Baker *et al.* (2022), and Kozakiewicz *et al.* (2023). Comparing the two images it seems visually that there is a clearer distinction between the different grains on the left image than on the right, mostly due to the clearer distinction in color and the lesser degree of transparency, resulting in clearer grain borders, even at the much lower resolution.

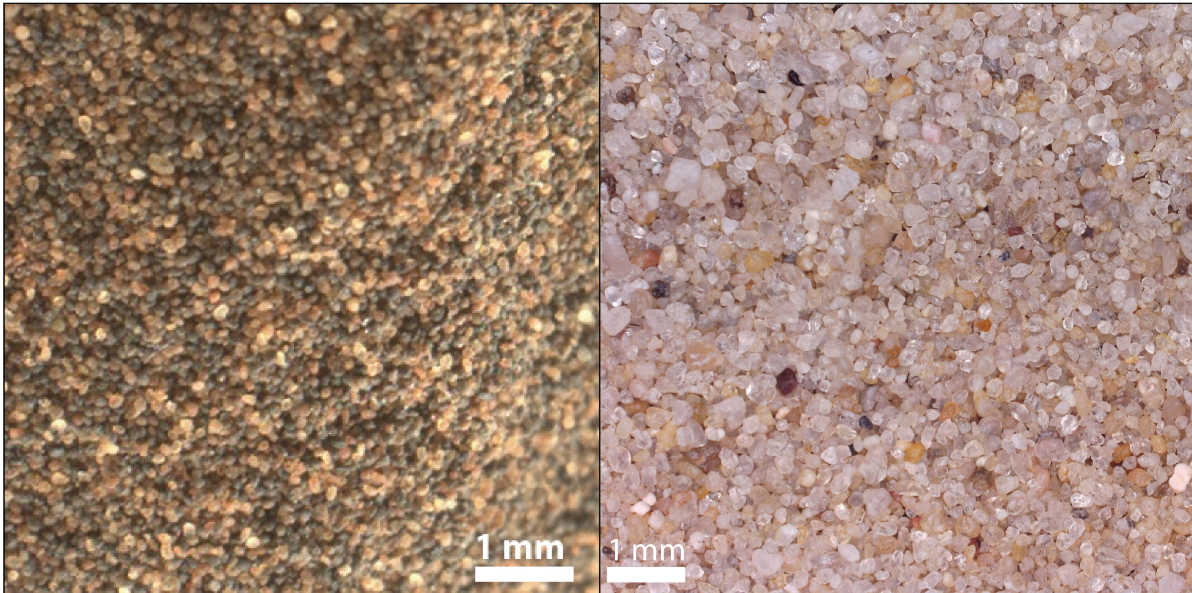


Figure 5.5: On the left, close-up by the Curiosity Mars Hand Lens Imager, MAHLI, on sol 1241, approximately 400x400 pixels. Note that the grains were passed through a 150 μm sieve (The Plantery Society, 2025). On the right, excerpt of wind tunnel image, approximately 1900x1900 pixels.

During the experiments, it was found that the threshold lay slightly higher than expected. When discussing the possible reasons behind this it was deduced that the sediment still contained some moisture after the drying procedure. Moisture can drastically increase the interparticle forces (Nickling & McKenna Neuman, 2009, p. 541). The material was dried for 24 hours at 100°C, which did not achieve the required pressure of the moisture to force its way out between the sand since the thickness of the sand was about 4 cm. For similar experiments in the future, it is recommended to dry the sand at a higher temperature to ensure the water vapor has enough pressure to move out of the sand. Alternatively, spreading the sand over a thinner surface will make it easier for the moisture to be removed.

There are multiple possible next steps based on this research. Most importantly it would be very interesting to map the effect of gravity on the preferred orientation to further illustrate the effect of grain impacts onto the sandbed on the degree of preferred orientation. Next, the effect of elongation can be investigated. It would seem that larger elongations tend to align themselves better with the direction of the wind, but the sample size became quite small so experiments using a smaller number of grains, manufactured to have a larger elongation would help to prove this. For the analysis method, it would be good to investigate the effect of using even more combinations of methods. For example, analyzing the different color channels separately or analyzing the inverted image. Inherently, the method of simple binarization works well for detecting lighter objects on a darker background, due to their use of a lower threshold for pixel intensity, so darker grains in the images are neglected, thus inverting the image will enable the detection of the dark grains. Lastly, it might be interesting to study the orientation of individual grains, to gain a direct observation of airborne streamlining of elongated grains, either by using a series of high-speed cameras near the sandbed with a very small number of particles, or by saltating a few of particles onto a sticky surface so that they retain their initial orientation, analyzing

with a similar method as used in these experiments. This would directly confirm that streamlining of the long-axis during saltation takes place.

This research gave insight into the effects of pressure and shear velocity on the degree of preferred orientation of saltating grains. The pressures that were investigated roughly correspond to pressures at high altitudes such as the Altiplano-Puna plateau and parts of the Atacama desert in South America, with altitudes varying from 3000 to 4200 meters (Prezzi *et al.*, 2014) and to the equivalent atmospheric pressure on Mars, as explained earlier. Given the results, this method of grain orientation determination can be useful mostly in situations of low shear velocity, near the fluid threshold, to globally determine the wind direction. While more elongated grains provide a clearer signal, it depends on the sediment how reliably specific elongations can be used. In the case of very few elongated grains in the sediment, many pictures would have to be taken to provide enough data for a reliable conclusion.

However, this method can possibly be used together with weather station readings on rovers. It can give insight into differences in the wind direction at 1.5 *m* above the sandbed where the weather stations are usually located, and the wind direction very near the surface. This can provide information on the influence of small-scale irregularities such as ripples and stones on the wind direction, or provide information on the long-term dominant wind direction, as opposed to the momentary reading of the weather station. Grain orientations offer information on the smallest scale of wind direction and strength, complementing the information from weather stations, and data obtained from ripples and dunes. Indeed, as the rover traverses the Martian surface, along the path of the rover the dominant wind direction near the surface can be mapped. Combining the results of several images in an area tends to provide a general estimate of the wind direction but at a lower fabric strength than the individual images.

6

Conclusion

This study aimed to quantify the preferred orientation of sand grains in ambient and low-pressure environments using wind tunnel experiments. The experiments were conducted at 1000, 720, 480, 240 and 14 *mbar*, and at 120% and 150% of the threshold shear velocity. To structure the research the following research question was formulated:

"To what degree does preferred orientation occur at different air pressures and velocities?"

The following sub-questions were formed to help answer the main research question:

- What is the influence of pressure and shear velocity on the fabric strength?
- How large is the effect of grain orientation randomization due to impacting grains at different pressures and velocities?
- How well does the preferred orientation align with the wind direction in wind tunnel experiments?

In order to quantify the degree of preferred orientation, the fabric strength, a measure of how well grains are aligned, and the preferred orientation were determined for 21 images of the sandbed for each experiment. For 150% of the threshold shear velocity, it was found that the fabric strength decreases as the pressure decreases, from 0.066 to 0.052. For 120% of the threshold, the same applies at high pressures, until a point comes where the fabric strengths increases again at lower pressures. The average fabric strength for 120% varies from 0.058 down to 0.055, then increases again up to 0.059 at lower pressures. In a sense, the fabric strengths flip. This is the result of the higher absolute velocity needed to engage the grains at lower pressures. While the airborne streamlining is expected to be present at all pressures, it will be more effective at high pressures, since the aerodynamic forces on the grain are greater. Furthermore, as the grain is expected to impact the surface with a larger velocity at lower pressures, the sandbed becomes more subject to the splashing of grains. This, in turn, results in more randomization of grain orientation, and thus more noise.

For most experiments, in at least a third of individual images the preferred orientation coincided within 30° of the expected flow direction in the wind tunnel. When combining the data of all images, the preferred orientation of seven out of 10 experiments was within 10° of the expected flow direction in the wind tunnel. Only one experiment deviated by more than 30°.

Next to the main investigation, the effect of elongation on the signal was found to be significant, with higher elongations achieving a higher fabric strength. However, the number of grains decreased dramatically as the elongation was increased. This resulted in statistically less relevant outcomes than lower elongations.

In conclusion, to answer the research questions, from the wind tunnel experiments and subsequent analysis it follows that for higher shear velocities the fabric strength increases with increasing pressure. On the other hand, for lower shear velocities the fabric strength increases with increasing pressure only at higher pressures. For a minimum particle elongation of 1.1, it was determined that at 14 and 240 *mbar* there is more preferred orientation for lower shear velocities than for higher shear velocities. This

flip is presumably a result of the randomization of grain orientations due to impacting grains. At lower pressures, the effect of impact randomization is larger than at higher pressures. At low pressures, a higher shear velocity is required to induce saltation, resulting in a higher acceleration of the grain and a higher impact speed. At higher pressures, the effect of streamlining of the particles during saltation is more prominent and the signal in the sandbed is less distorted by impacting grains. Thus, at lower pressures, increased wind speed leads to more noise and less preferred orientation. For individual images, the preferred orientation does not reliably coincide with the wind direction. However, if the data from multiple images in a general area are combined, the wind direction can in most cases be established within 10° of the actual direction, for various shear velocities and pressures, as this presumably suppresses small-scale disturbances that occur to grains in the same image. Finally, preferred orientation is more pronounced at higher pressures and shear velocities, while at lower pressures the fabric strength is increased for lower shear velocities. This effect is a result of the combination of streamlining dominating at higher pressures, while randomization due to impacts dominates at lower pressures.

References

- Abdulkarim, M., Grema, H., Adamu, I., Mueller, D., Schulz, M., Ulbrich, M., Miocic, J., & Preusser, F. (2021). Effect of using different chemical dispersing agents in grain size analyses of fluvial sediments via laser diffraction spectrometry. *Methods and protocols*, 4(3), 44.
- Almeida, M., Parteli, E., Andrade, J., & Herrmann, H. (2008). Giant saltation on mars. *Proceedings of the National Academy of Sciences*, 105(17), 6222–6226. <https://doi.org/10.1073/pnas.0800202105>
- Ammi, M., Oger, L., Beladjine, D., & Valance, A. (2009). Three-dimensional analysis of the collision process of a bead on a granular packing. *Physical Review E*, 79(2), 021305. <https://doi.org/10.1103/physreve.79.021305>
- Anderson, R., & Haff, P. (1991). Wind modification and bed response during saltation of sand in air. *Aeolian Grain Transport 1: Mechanics*, 21–51. https://doi.org/10.1007/978-3-7091-6706-9_{ }2
- Andreotti, B., Claudin, P., Iversen, J., Merrison, J., & Rasmussen, K. (2021). A lower-than-expected saltation threshold at martian pressure and below. *Proceedings of the National Academy of Sciences*, 118(5), e2012386118.
- Ashton, A., Murray, A., & Arnoult, O. (2002). Formation of coastline features by large-scale instabilities induced by high-angle waves. *Nature*, 414(1), 296–300. <https://doi.org/10.1038/35104541>
- Bagnold, R. (1941). *The physics of blown sand and desert dunes* (2nd ed.). Methuen.
- Bagnold, R. (1937). The transport of sand by wind. *The Geographical Journal*, 89(5), 409–438. <https://doi.org/10.2307/1786411>
- Baker, M., Newman, C., Sullivan, R., Minitti, M., Edgett, K., Fey, D., Ellison, D., & Lewis, K. (2022). Diurnal variability in aeolian sediment transport at gale crater, mars. *Journal of Geophysical Research: Planets*, 127(2), e2020JE006734.
- Barrett, P. (1980). The shape of rock particles, a critical review. *Sedimentology*, 27(3), 291–303. <https://doi.org/10.1111/j.1365-3091.1980.tb01179.x>
- Bates, R., & Jackson, J. (1980). *Glossary of geology* (2nd ed.). American Geological Institute.
- Beladjine, D., Ammi, M., Oger, L., & Valance, A. (2007). Collision process between an incident bead and a three-dimensional granular packing. *Physical Review E*, 75(6). <https://doi.org/10.1103/physreve.75.061305>
- Boggs, S. (2009). *Petrology of sedimentary rocks*. Cambridge university press.
- Bradski, G. (2000). The OpenCV Library. *Dr. Dobb's Journal of Software Tools*.
- Brewer, R. (1965). Fabric and mineral analysis of soils. *Soil Science*, 100(1), 73. <https://doi.org/10.1097/00010694-196507000-00024>
- Butler, J. B., Lane, S. N., & Chandler, J. H. (2001). Automated extraction of grain-size data from gravel surfaces using digital image processing. *Journal of hydraulic research*, 39(5), 519–529.
- Cameron, S., Nikora, V., & Witz, M. (2020). Entrainment of sediment particles by very large-scale motions. *Journal of Fluid Mechanics*, 888, A7.
- Cannon, K., Britt, D., Smith, T., Fritsche, R., & Batchelder, D. (2019). Mars global simulant mgs-1: A rocknest-based open standard for basaltic martian regolith simulants. *Icarus*, 317, 470–478.
- Canny, J. (1986). A computational approach to edge detection. *IEEE Transactions on pattern analysis and machine intelligence*, (6), 679–698.
- Carneiro, M., Rasmussen, K., & Herrmann, H. (2015). Bursts in discontinuous aeolian saltation. *Scientific Reports*, 5(1), 11109.
- Carter, M. R., & Gregorich, E. G. (2007). *Soil sampling and methods of analysis*. CRC press.
- Carver, R. (1971). *Procedures in sedimentary petrology*. John Wiley & Sons.
- Castellanos, A. (2005). The relationship between attractive interparticle forces and bulk behaviour in dry and uncharged fine powders. *Advances in physics*, 54(4), 263–376. <https://doi.org/10.1080/17461390500402657>
- Celestron. (2023). *Handheld digital microscope pro*. Retrieved November 24, 2023, from <https://www.celestron.com/products/handheld-digital-microscope-pro#specifications>

- Charalambous, C., McClean, J. B., Baker, M., Pike, W. T., Golombek, M., Lemmon, M., Ansan, V., Perrin, C., Spiga, A., Lorenz, R. D., Banks, M. E., Murdoch, N., Rodriguez, S., Weitz, C. M., Grant, J. A., Warner, N. H., Garvin, J., Daubar, I. J., Hauber, E., . . . Banerdt, W. B. (2021). Vortex-dominated aeolian activity at insight's landing site, part 1: Multi-instrument observations, analysis, and implications. *Journal of Geophysical Research: Planets*, 126(6), e2020JE006757.
- Chevrier, V., & Mathé, P. (2007). Mineralogy and evolution of the surface of mars: A review. *Planetary and Space Science*, 55(3), 289–314.
- Claudin, P., & Andreotti, B. (2006). A scaling law for aeolian dunes on mars, venus, earth, and for subaqueous ripples. *Earth and Planetary Science Letters*, 252(1-2), 30–44.
- Colombatti, G., Bettanini, C., Aboudan, A., Debei, S., Esposito, F., Molfese, C., Cecere, A., Merrison, J., & Iversen, J. (2018). Marstem sensor simulations in martian dust environment. *Measurement*, 122, 453–458.
- Creysseels, M., Dupont, P., El Moctar, A., Valance, A., Cantat, I., Jenkins, J., Pasini, J., & Rasmussen, K. (2009). Saltating particles in a turbulent boundary layer: Experiment and theory. *Journal of Fluid Mechanics*, 625, 47–74.
- Dapples, E., & Rominger, J. (1945). Orientation analysis of fine-grained clastic sediments: A report of progress. *The Journal of Geology*, 53(4), 246–261. <https://doi.org/10.1086/625284>
- Das, N., & Ashmawy, A. (2007). Relationship between grain size and shape of natural and crushed sand. In *Advances in measurement and modeling of soil behavior* (pp. 1–10).
- Davies, C. (1947). The sedimentation of small suspended particles. *Supplement to Trans. Inst. Chem. Eng. and Soc. Cemical Industry*, 25, 25–39.
- de Vet, S. (2013). When the glacier left the volcano: Behaviour and fate of glaciovolcanic glass in different planetary environments [Thesis, fully internal, Universiteit van Amsterdam. <https://hdl.handle.net/11245/1.394291>].
- de Vet, S., Merrison, J., Mittelmeijer-Hazeleger, M., Van Loon, E., & Cammeraat, L. (2014). Effects of rolling on wind-induced detachment thresholds of volcanic glass on mars. *Planetary and Space Science*, 103, 205–218.
- Den Bosch Region. (2024). "bedafse bergen | stuifduinen". Retrieved November 8, 2024, from <https://www.denboschregion.nl/nl/overzicht-locaties/3969608698/bedafse-bergen-stuifduinen>
- Diepenbroek, M., Bartholomä, A., & Ibbeken, H. (1992). How round is round? a new approach to the topic 'roundness' by fourier grain shape analysis. *Sedimentology*, 39(3), 411–422. <https://doi.org/10.1111/j.1365-3091.1992.tb02125.x>
- Doorenbosch, M., & van Mourik, J. (2016). The impact of ancestral heath management on soils and landscapes: A reconstruction based on paleoecological analyses of soil records in the central and southeastern netherlands. *Soil*, 2(3), 311–324.
- Dracos, T. (1996). *Particle tracking velocimetry (ptv)*. in: Dracos, t. (eds) *three-dimensional velocity and vorticity measuring and image analysis techniques: Lecture notes from the short course held in zürich, switzerland, 3–6 september 1996* (Vol. 4). Springer Science & Business Media.
- Edgett, K. S., Yingst, R. A., Ravine, M. A., Caplinger, M. A., Maki, J. N., Ghaemi, F. T., Schaffner, J. A., Bell, J. F. I., Edwards, L. J., Herkenhoff, K. E., Heydari, E., Kah, L. C., Lemmon, M. T., Minitti, M. E., Olson, T. S., Parker, T. J., Rowland, S. K., Schieber, J., Sullivan, R. J., . . . Goetz, W. (2012). Curiosity's mars hand lens imager (mahli) investigation. *Space science reviews*, 170, 259–317.
- Edgett, K., Caplinger, M., & Ravine, M. (2019). Mars 2020 perseverance sherloc watson camera pre-delivery characterization and calibration report. *Malin Space Science Systems, San Diego, California*.
- Ehlmann, B. L., Edgett, K. S., Sutter, B., Achilles, C., Litvak, M. L., Lapotre, M. G. A., Sullivan, R., Fraeman, A. A., Arvidson, R. E., Blake, D. F., et al. (2017). Chemistry, mineralogy, and grain properties at namib and high dunes, bagnold dune field, gale crater, mars: A synthesis of curiosity rover observations. *Journal of Geophysical Research: Planets*, 122(12), 2510–2543.
- Ewing, R., Lapotre, M., Lewis, K., Day, M., Stein, N., Rubin, D., Sullivan, R., Banham, S., Lamb, M., Bridges, N., Gupta, S., & Fischer, W. (2017). Sedimentary processes of the bagnold dunes: Implications for the eolian rock record of mars. *Journal of Geophysical Research: Planets*, 122(12), 2544–2573.
- Gemeente Maashorst. (n.d.). "bedafse bergen". Retrieved November 8, 2024, from <https://www.gemeentemaashorst.nl/ontdek-maashorst/natuurgebied-de-maashorst-/bedafse-bergen>
- GISGeography. (n.d.). *Obia – object-based image analysis (geobia)*. Retrieved June 25, 2024, from <https://gisgeography.com/obia-object-based-image-analysis-geobia/>

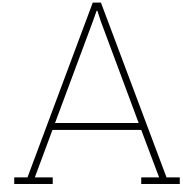
- Glezen, W., & Ludwick, J. (1963). An automated grain-shape classifier. *Journal of Sedimentary Research*, 33(1), 23–40. <https://doi.org/10.1306/74d70db7-2b21-11d7-8648000102c1865d>
- Gonzalez, R. (2009). *Digital image processing*. Pearson education india.
- Gough, T., Hugenholtz, C., & Barchyn, T. (2021). Re-evaluation of large martian ripples in gale crater: Granulometric evidence for an impact mechanism and terrestrial analogues. *Journal of Geophysical Research: Planets*, 126(12), e2021JE007011.
- Greeley, R. (2002). Saltation impact as a means for raising dust on mars. *Planetary and Space Science*, 50(2), 151–155.
- Greeley, R., & Iversen, J. (1985). *Wind as a geological process on earth, mars, venus and titan*. Cambridge University Press.
- Greeley, R., Iversen, J., Pollack, J., Udovich, N., & White, B. (1974). Wind tunnel studies of martian aeolian processes. *Proceedings of the Royal Society of London. A. Mathematical and Physical Sciences*, 341(1626), 331–360.
- Greeley, R., Leach, R., White, B., Iversen, J., & Pollack, J. (1980). Threshold windspeeds for sand on mars: Wind tunnel simulations. *Geophysical Research Letters*, 7(2), 121–124.
- Greeley, R., White, B., Leach, R., Iversen, J., & Pollack, J. (1976). Mars: Wind friction speeds for particle movement. *Geophysical Research Letters*, 3(8), 417–420.
- Hassanpour, R. (2012). The use of arcgis for determination of quartz optical axis orientation in thin section images. *Journal of Microscopy*, 245(3), 276–287.
- Heilbronner, R. (2000). Automatic grain boundary detection and grain size analysis using polarization micrographs or orientation images. *Journal of Structural Geology*, 22(7), 969–981.
- Holstein-Rathlou, C., Merrison, J., Iversen, J., Jakobsen, A., Nicolajsen, R., Nørnberg, P., Rasmussen, K., Merlone, A., Lopardo, G., Hudson, T., D., B., & G., P. (2014). An environmental wind tunnel facility for testing meteorological sensor systems. *Journal of atmospheric and oceanic technology*, 31(2), 447–457.
- Hovden, R., Xin, H., & Muller, D. (2011). Extended depth of field for high-resolution scanning transmission electron microscopy. *Microscopy and Microanalysis*, 17(1), 75–80.
- Huber, L. (2023). *Planetary Data System: The Planetary Atmospheres Node*. Retrieved January 31, 2025, from https://pds-atmospheres.nmsu.edu/education_and_outreach/encyclopedia/gas_constant.htm
- Hunzicher, A. (1930). *A laboratory study of antidune traction and the transnortation and denosition of ellipsoidal an'shaned nebbies: Unpublished". s* [Doctoral dissertation, Thesis, univ. of].
- Illenberger, W. (1991). Pebble shape (and size!) *Journal of Sedimentary Research*, 61(5), 756–767.
- ImageJ. (n.d.). *Introduction*. Retrieved February 12, 2024, from <https://imagej.net/ij/docs/intro.html>
- Iversen, J., & Rasmussen, K. (1999). The effect of wind speed and bed slope on sand transport. *Sedimentology*, 46(4), 723–731.
- Iversen, J., & White, B. (1982a). Saltation threshold on earth, mars and venus. *Sedimentology*, 29(1), 111–119.
- Iversen, J., & White, B. (1982b). Saltation threshold on earth, mars and venus. *Sedimentology*, 29(1), 111–119.
- Iversen, J. (2023). *AWTS II technical facts* (tech. rep.) (https://phys.au.dk/fileadmin/site_files/forskning/Planetology/AWTS_II_windtunnel_technical_fact_sheet.pdf). Aarhus University Department of Physics and Astronomy.
- Jordan, R., Tobin, R., Lundegard, P., Samuels, N., Schauf, F., Thaeller, J., V., V., & Potter, P. (1981). Comparison of methods of size analysis for sands of the amazon-solimões rivers, brazil and peru. *Sedimentology*, 28(1), 123–128.
- Josset, J., Westall, F., Hofmann, B., Spray, J., Cockell, C., Kempe, S., Griffiths, A., De Sanctis, M., Colangeli, L., Koschny, D., Föllmi, K., Verrecchia, E., Diamond, L., Josset, M., Javaux, E., Esposito, F., Gunn, M., Souchon-Leitner, A., Bontognali, T., et al. (2017). The close-up imager onboard the esa exomars rover: Objectives, description, operations, and science validation activities. *Astrobiology*, 17(6-7), 595–611.
- Kok, J. (2010a). Difference in the wind speeds required for initiation versus continuation of sand transport on mars: Implications for dunes and dust storms. *Physical Review Letters*, 104(7), 074502.
- Kok, J. (2010b). An improved parameterization of wind-blown sand flux on mars that includes the effect of hysteresis. *Geophysical Research Letters*, 37(12).

- Kok, J., Partelli, E., Michaels, T., & Karam, D. (2012). The physics of wind-blown sand and dust. *Reports on progress in physics*, 75(1).
- Kok, J., & Renno, N. (2009). A comprehensive numerical model of steady state saltation (comsalt). *Journal of Geophysical Research: Atmospheres*, 114(D17).
- Kozakiewicz, J. (2018). Image analysis algorithm for detection and measurement of martian sand grains. *Earth Science Informatics*, 11(2), 257–272.
- Kozakiewicz, J., Kania, M., Salata, D., & Nowak, L. (2023). Sands on meridiani planum, mars. *Journal of Geophysical Research: Planets*, 128(10), e2023JE007804.
- Krumbein, W. (1941). Measurement and geological significance of shape and roundness of sedimentary particles. *Journal of Sedimentary Research*, 11(2), 64–72.
- Krumbein, W. (1942). Settling-velocity and flume-behavior of non-spherical particles. *Eos, Transactions American Geophysical Union*, 23(2), 621–633.
- Kunkel, W. (1948). Magnitude and character of errors produced by shape factors in stokes' law estimates of particle radius. *Journal of Applied Physics*, 19(11), 1056–1058.
- Lane, E., & Carlson, E. (1954). Some observations on the effect of particle shape on the movement of coarse sediments. *Eos, Transactions American Geophysical Union*, 35(3), 453–462.
- Li, Y., Onasch, C., & Guo, Y. (2008). Gis-based detection of grain boundaries. *Journal of Structural Geology*, 30(4), 431–443.
- MathWorks. (2023). *Graythresh*. Retrieved February 11, 2024, from <https://www.mathworks.com/help/images/ref/graythresh.html>
- Mazzullo, J., Alexander, A., Tieh, T., & Menglin, D. (1992). The effects of wind transport on the shapes of quartz silt grains. *Journal of Sedimentary Research*, 62(6), 961–971.
- McNown, J., & Malaika, J. (1950). Effects of particle shape on settling velocity at low reynolds numbers. *Eos, Transactions American Geophysical Union*, 31(1), 74–82.
- Merrison, J., Bechtold, H., Gunnlaugsson, H., Jensen, A., Kinch, K., Nornberg, P., & Rasmussen, K. (2008). An environmental simulation wind tunnel for studying aeolian transport on mars. *Planetary and Space Science*, 56(3-4), 426–437.
- Merrison, J., Gunnlaugsson, H., Nørnberg, P., Jensen, A., & Rasmussen, K. (2007). Determination of the wind induced detachment threshold for granular material on mars using wind tunnel simulations. *Icarus*, 191(2), 568–580.
- Meyer, F., & Beucher, S. (1990). Morphological segmentation. *Journal of visual communication and image representation*, 1(1), 21–46.
- NASA. (2022). *Mars 3 lander*. Retrieved June 29, 2024, from <https://nssdc.gsfc.nasa.gov/nmc/spacecraft/display.action?id=1971-049F>
- NASA. (2024). *Viking spacecraft and science*. Retrieved June 29, 2024, from <https://science.nasa.gov/mission/viking/spacecraft-and-science/>
- Nickling, W. (1988). The initiation of particle movement by wind. *Sedimentology*, 35(3), 499–511.
- Nickling, W., & McKenna Neuman, C. (2009). *Aeolian sediment transport* (2nd ed.) [pp 517-555]. Springer.
- NIH. (n.d.). *Nih image*. Retrieved February 12, 2024, from <https://imagej.net/ij/nih-image/>
- Nowiński, G. (2020). *Processing and analysis of digital microscopic images from the mars exploration rover mission*. Retrieved November 19, 2024, from https://github.com/novinxy/MER_particle_detection
- Otsu, N. (1979). A threshold selection method from gray-level histograms. *IEEE transactions on systems, man, and cybernetics*, 9(1), 62–66.
- Pähtz, T., Clark, A., Valyrakisand, M., & Durán, O. (2020). The physics of sediment transport initiation, cessation, and entrainment across aeolian and fluvial environments. [<https://doi.org/10.1029/2019RG000679>]. *Reviews of Geophysics*, 58(1), e2019RG000679.
- Pähtz, T., Valyrakis, M., Zhao, X., & Li, Z. (2018). The critical role of the boundary layer thickness for the initiation of aeolian sediment transport. *Geosciences*, 8(9), 314.
- Pettijohn, F. (1942). Quantitative and analytical sedimentation. *Nat. Res. Council Report of Committee on Sedimentation*, 1940–1941.
- Powers, M. (1953). A new roundness scale for sedimentary particles. *Journal of Sedimentary Research*, 23(2), 117–119.
- Prezzi, C., Llanos, M. P. I., Götze, H.-J., & Schmidt, S. (2014). Thermal and geodynamic contributions to the elevation of the altiplano–puna plateau. *Physics of the Earth and Planetary Interiors*, 237, 51–64.
- Rasmussen, K., Kok, J., & Merrison, J. (2009). Enhancement in wind-driven sand transport by electric fields. *Planetary and Space Science*, 57(7), 804–808.

- Rasmussen, K., & Sørensen, M. (1999). Aeolian mass transport near the saltation threshold. *Earth Surface Processes and Landforms: The Journal of the British Geomorphological Research Group*, 24(5), 413–422.
- Rasmussen, K., & Sørensen, M. (2008). Vertical variation of particle speed and flux density in aeolian saltation: Measurement and modeling. *Journal of geophysical research: earth surface*, 113(F2).
- Rasmussen, K., Valance, A., & Merrison, J. (2015). Laboratory studies of aeolian sediment transport processes on planetary surfaces. *Geomorphology*, 244, 74–94.
- Rice, M., Willetts, B., & McEwan, I. (1995). An experimental study of multiple grain-size ejecta produced by collisions of saltating grains with a flat bed. *Sedimentology*, 42(4), 695–706.
- Riley, M. (1953). A new roundness scale for sedimentary particles. *Journal of Sedimentary Petrology*, 11, 94–97.
- Rusnak, G. (1957). The orientation of sand grains under conditions of "unidirectional" fluid flow: 1. theory and experiment. *The Journal of Geology*, 65(4), 384–409.
- Russell, R., & Taylor, R. (1937). Roundness and shape of mississippi river sands. *The Journal of Geology*, 45(3), 225–267.
- Sagar, B., Cheng, Q., McKinley, J., & Agterberg, F. (2023). *Encyclopedia of mathematical geosciences* [pp 1008–1012]. Springer Nature. https://doi.org/https://doi.org/10.1007/978-3-030-85040-1_229
- Schneiderhöhn, P. (1954). Eine vergleichende studie über methoden zur quantitativen bestimmung von abrundung und form an sandkörnern (im hinblick auf die verwendbarkeit an dünnschliffen.) *Heidelberger Beiträge zur Mineralogie und Petrographie*, 4, 172–191.
- Schwan, J. (1989). Grain fabrics of natural and experimental low-angle aeolian sand deposits. *Geologie en Mijnbouw*, 68, 211–219.
- Shao, Y., & Lu, H. (2000). A simple expression for wind erosion threshold friction velocity. *Journal of Geophysical Research*, 105(17), 22123–22454.
- Shepard, F., Manar, R., & Young, R. (1961). Distinguishing between beach and dune sands. *Journal of Sedimentary Research*, 31(2), 196–214.
- Sneed, E., & Folk, R. (1958). Pebbles in the lower colorado river, texas a study in particle morphogenesis. *The Journal of Geology*, 66(2), 114–150.
- Soille, P. (1999). Morphological image analysis: Principles and applications.
- Staengel, M. (2021). *Multi-resolution segmentation*. Retrieved February 11, 2024, from <https://support.econognition.com/hc/en-us/articles/360016173600-Multi-resolution-Segmentation>
- Stott, A., Garcia, R., Murdoch, N., Mimoun, D., Drilleau, M., Newman, C., Spiga, A., Banfield, D., Lemmon, M., Navarro, S., Mora-Sotomayor, L., Charalambous, C., Pike, W., Lognonné, P., & Banerdt, W. (2025). WindSightNet: The inter-annual variability of martian winds retrieved from InSight's seismic data with machine learning. *Journal of Geophysical Research: Planets*, 130(2), e2024JE008695.
- Stryk, T. (2021). *Every picture from venus' surface, ever*. Retrieved June 29, 2024, from <https://www.planetary.org/articles/every-picture-from-venus-surface-ever>
- Sulaiman, M., Sinnakaudan, S., Ng, S., & Strom, K. (2014). Application of automated grain sizing technique (ags) for bed load samples at rasil river: A case study for supply limited channel. *Catena*, 121, 330–343.
- Sullivan, R., & Kok, J. (2017). Aeolian saltation on mars at low wind speeds. *Journal of Geophysical Research: Planets*, 122(10), 2111–2143.
- Swann, C., Sherman, D., & Ewing, R. (2020). Experimentally derived thresholds for windblown sand on mars. *Geophysical Research Letters*, 47(3), e2019GL084484.
- Swanson, F. (1972). Morphogenesis and shape sorting of coarse sediment in the elk river, southwestern oregon: Unpublished ph. D dissertation, University of Oregon (USA), OR.
- Sympatec GmbH. (2024a). *Qicpic*. Retrieved November 11, 2024, from <https://www.sympatec.com/en/particle-measurement/sensors/dynamic-image-analysis/qicpic>
- Sympatec GmbH. (2024b). *Sucell/l*. Retrieved November 11, 2024, from <https://www.sympatec.com/en/particle-measurement/dispersing-units/wet/sucell>
- Syvitski, J. (1991). *Principles, methods, and application of particle size analysis* (Vol. 388). Cambridge University Press Cambridge.
- The European Space Agency. (2023). *Facts about mars*. Retrieved November 24, 2023, from https://www.esa.int/Science_Exploration/Space_Science/Mars_Express/Facts_about_Mars
- The Martian Garden. (2023). *Mms-2 enhanced mars simulant*. Retrieved November 20, 2023, from <https://www.themartiangarden.com/mms2/mms2>

- The Planetary Society. (2025). *Bruce Murray Space Image Library: Tiny grains of Martian sand*. Retrieved February 2, 2025, from <https://www.planetary.org/space-images/tiny-grains-of-martian-sand>
- Trimble. (2019a). *Basic rule set editing*. Retrieved February 11, 2024, from https://docs.ecognition.com/v9.5.0/eCognition_documentation/User%20Guide%20Developer/4%20Basic%20Rule%20Set%20Editing.htm
- Trimble. (2019b). *The power of ecognition*. Retrieved June 24, 2024, from https://docs.ecognition.com/v9.5.0/eCognition_documentation/Modules/1%20eCognition%20at%20a%20glance/01%20Introduction%20to%20the%20Power%20of%20eCognition.htm#:~:text=eCognition%20is%20designed%20to%20improve,the%20interpretation%20of%20geospatial%20data.
- Trimble. (2024). *Trimble ecognition*. Retrieved February 11, 2024, from <https://geospatial.trimble.com/en/products/software/trimble-ecognition>
- Tsoar, H., & Pye, L. (1987). Dust transport and the question of desert loess formation. *Sedimentology*, 34(1), 139–153.
- Tyler, W. (1967). Testing sieves and their uses. *Tyler Industrial Products, Handbook*, 53.
- Van der Walt, S., Schönberger, J., Nunez-Iglesias, J., Boulogne, F., Warner, J., Yager, N., Gouillart, E., & Yu, T. (2014). Scikit-image: Image processing in python. *PeerJ*, 2, e453.
- Van Mourik, J., Seijmonsbergen, A., Slotboom, R., & Wallinga, J. (2012). Impact of human land use on soils and landforms in cultural landscapes on aeolian sandy substrates (maashorst, se-netherlands). *Quaternary International*, 265, 74–89.
- Ventola, A. (2022). *Development of lab, field, and in-situ image collection systems and analysis methods for soil characterization* [Doctoral dissertation].
- Viúdez-Moreiras, D., de la Torre, M., Gómez-Elvira, J., Lorenz, R., Apéstigue, V., Guzewich, S., Mischna, M., Sullivan, R., Herkenhoff, K., Toledo, D., Lemmon, M., Smith, M., Newman, C. E., Sánchez-Lavega, A., Rodríguez-Manfredi, J. A., Hueso, R., Harri, A., Tamppari, L., Arruego, I., & Bell, J. (2022). Winds at the mars 2020 landing site. 2. wind variability and turbulence. *Journal of Geophysical Research: Planets*, 127(12), e2022JE007523.
- Viúdez-Moreiras, D., Lemmon, M., Newman, C., Guzewich, S., Mischna, M., Gómez-Elvira, J., Sánchez-Lavega, A., Herkenhoff, K., De La Torre, M., Rodríguez-Manfredi, J., Lorenz, R., Navarro, S., Pla-García, J., Hueso, R., Richardson, M., Smith, M., Apéstigue, V., Toledo, D., & Bell, J. (2022). Winds at the mars 2020 landing site: 1. near-surface wind patterns at jezero crater. *Journal of Geophysical Research: Planets*, 127(12), e2022JE007522.
- Wadell, H. (1933). Sphericity and roundness of rock particles. *The Journal of Geology*, 41(3), 310–331.
- Wadell, H. (1935). Volume, shape, and roundness of quartz particles. *The Journal of Geology*, 43(3), 250–280.
- Wadell, H. (1932). Volume, shape, and roundness of rock particles. *The Journal of Geology*, 40(5), 443–451.
- Wallinga, J., Sevink, J., Van Mourik, J., & Reimann, T. (2019). Luminescence dating of soil archives. *Reading the soil archives: unraveling the geoecological code of palaeosols and sediment cores*, edited by: van Mourik, J. and van der Meer, J., *Developments in quaternary science*, Elsevier, Amsterdam, 115–162.
- Waza, A., Kjer, J., Peiteado, M., Jardiel, T., Iversen, J., Rasmussen, K., & Merrison, J. (2023). Aeolian dust resuspension on mars studied using a recirculating environmental wind tunnel. *Planetary and Space Science*, 227, 105638.
- Weitz, C., Sullivan, R., Lapotre, M., Rowland, S., Grant, J., Baker, M., & Yingst, R. (2018). Sand grain sizes and shapes in eolian bedforms at gale crater, mars. *Geophysical Research Letters*, 45(18), 9471–9479.
- Wentworth, C. (1922a). A scale of grade and class terms for clastic sediments. *The journal of geology*, 30(5), 377–392.
- Wentworth, C. (1922b). *The shapes of beach pebbles*. US Government Printing Office.
- White, B. (1979). Soil transport by winds on mars. *Journal of Geophysical Research: Solid Earth*, 84(B9), 4643–4651.
- White, F. (2006). *Viscous fluid flow* (3rd ed.). McGraw-Hill.
- Willets, B., Rice, M., & Swaine, S. (1982). Shape effects in aeolian grain transport. *Sedimentology*, 29(3), 409–417.
- Williams, D. (2024). *Mars fact sheet*. Retrieved January 31, 2025, from <https://nssdc.gsfc.nasa.gov/planetary/factsheet/marsfact.html>
- Williams, G. (1964). Some aspects of the eolian saltation load. *Sedimentology*, 3(4), 257–287.

- Wolff, R., & Benedict, P. (1964). *Sedimentology: General introduction and definitions: Fluvial sediment and channel morphology* (tech. rep.). US Geological Survey, Water Resources Division.
- Zheng, X., Huang, N., & Zhou, Y. (2006). The effect of electrostatic force on the evolution of sand saltation cloud. *The European Physical Journal E*, 19(1), 129–138.
- Zingg, T. (1935). *Beitrag zur schotteranalyse* [Doctoral dissertation, ETH Zurich].



Experiments supplementary information

Below in Table A.1, an overview is shown of the performed experiments in chronological order. Note that for the main research objectives of this thesis, experiments 1, 4, 7 and 14 were not taken into account. These experiments were the first pilot run, two runs with a pre-rippled sandbed and a run to obtain large ripples, respectively. The *grains sieved pre-experiment* indicates that a small quantity of sand grains sieved over the measurement locations shown in Figure A.1 to ensure initial randomization of the orientation of the sand grains and remove any orientation induced by the smoothing of the sandbed. Next, *pictures pre-experiment* indicates that pictures were taken at some of the measurement locations to determine the original orientation of grains in the sandbed and compare them to the orientation of the grains after saltation. It was decided not to pursue this comparison since the quantity of the transported sand was so large that any pre-existing orientation in the fabric would be completely overprinted by the signal due to saltation.

Table A.1: Overview of all performed experiments and their settings. "-" indicates it was not performed, "x" indicates that it was performed and "?" indicates that it was not documented.

Experiment	Pressure (mbar)	Velocity (% of u_{*t})	Fan speed (RPM)	Duration (s)	Smoothing	Grains sieved pre-experiment	Pictures Pre-experiment	Mass sand trap (gr)	Threshold determination
1	1000	150	135	100	All	-	-	-	x
2	1000	120	108	630	Last 1 m	x	x	-	-
3	1000	150	135	100	Last 1 m	-	x	13.63	-
4	1000	120	108	630	Last 1 m	?	-	5.59	-
5	14 (Mars)	120	660	100	All	x	x	16.38	x
6	14 (Mars)	150	825	100	All	x	x	?	-
7	14 (Mars)	120	660	100	Last 1 m	x	x	18.11	-
8	720	120	132	630	All	x	x	?	x
9	720	150	165	100	Last 1 m	x	x	18.71	-
10	240	120	228	630	All	x	x	2.99	x
11	240	150	282	100	All	x	x	30.91	-
12	480	120	167	420	All	x	x	16.48	x
13	480	150	209	100	All	x	x	26.8	-
14	14 (Mars)	120	660	1200	All	?	x	-	-



Figure A.1: In white, grid of images taken using the microscope. The images were taken at 2 *cm* intervals, with the size of each image encompassing approximately 1.1 by 0.8 *cm* of the sandbed. Top view, the flow direction is right to left. On the left, the imprint left in the sand is that of the sand trap.

B

Results settings optimization

Below the results of the settings optimization procedure are shown. For each of the three grain size classes, six comparisons of settings were performed. First, the effects of the opening and sharpening radii were compared in Figure B.1, Figure B.2 and Figure B.3, followed by the upper and lower thresholds for canny edge detection, shown in Figure B.4, Figure B.5 and Figure B.6. Next, the sigma of the Gaussian blurring prior to the canny edge detection and the aperture size used for the canny edge detection are shown in Figure B.7, Figure B.8 and Figure B.9. The binarization heatmaps are presented in Figure B.10, Figure B.11 and Figure B.12, followed by the kernel size and sigma for the Gaussian Filter in Figure B.13, Figure B.14 and Figure B.15. Lastly, the effects of the h-values for the extended maxima are shown in Figure B.16, Figure B.17 and Figure B.18.

The blue graphs shows the original optimization and the purple graphs show the verification performed on a different image.

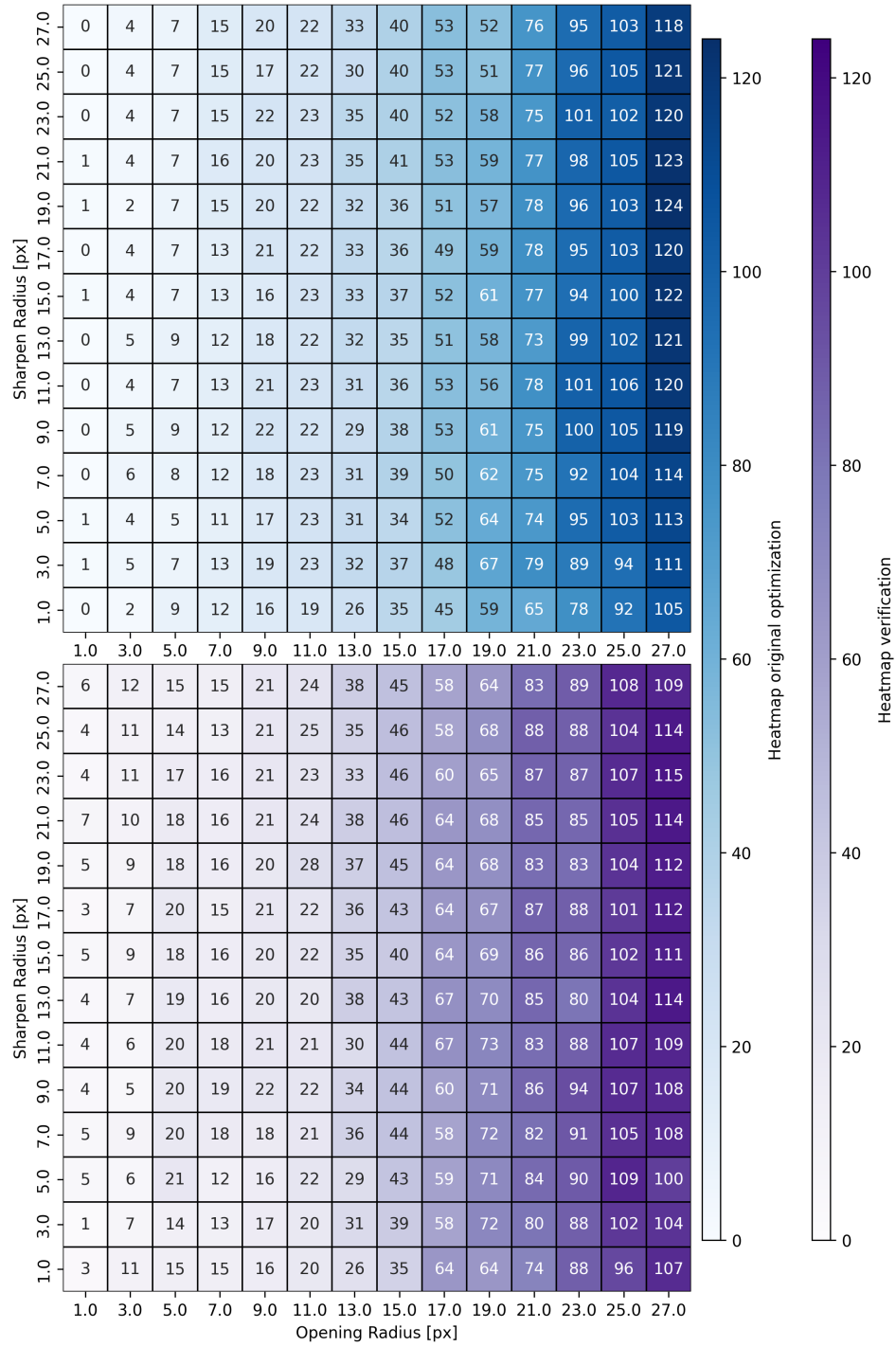


Figure B.1: Number of detected grains for different opening and sharpening radii combinations for large grains.

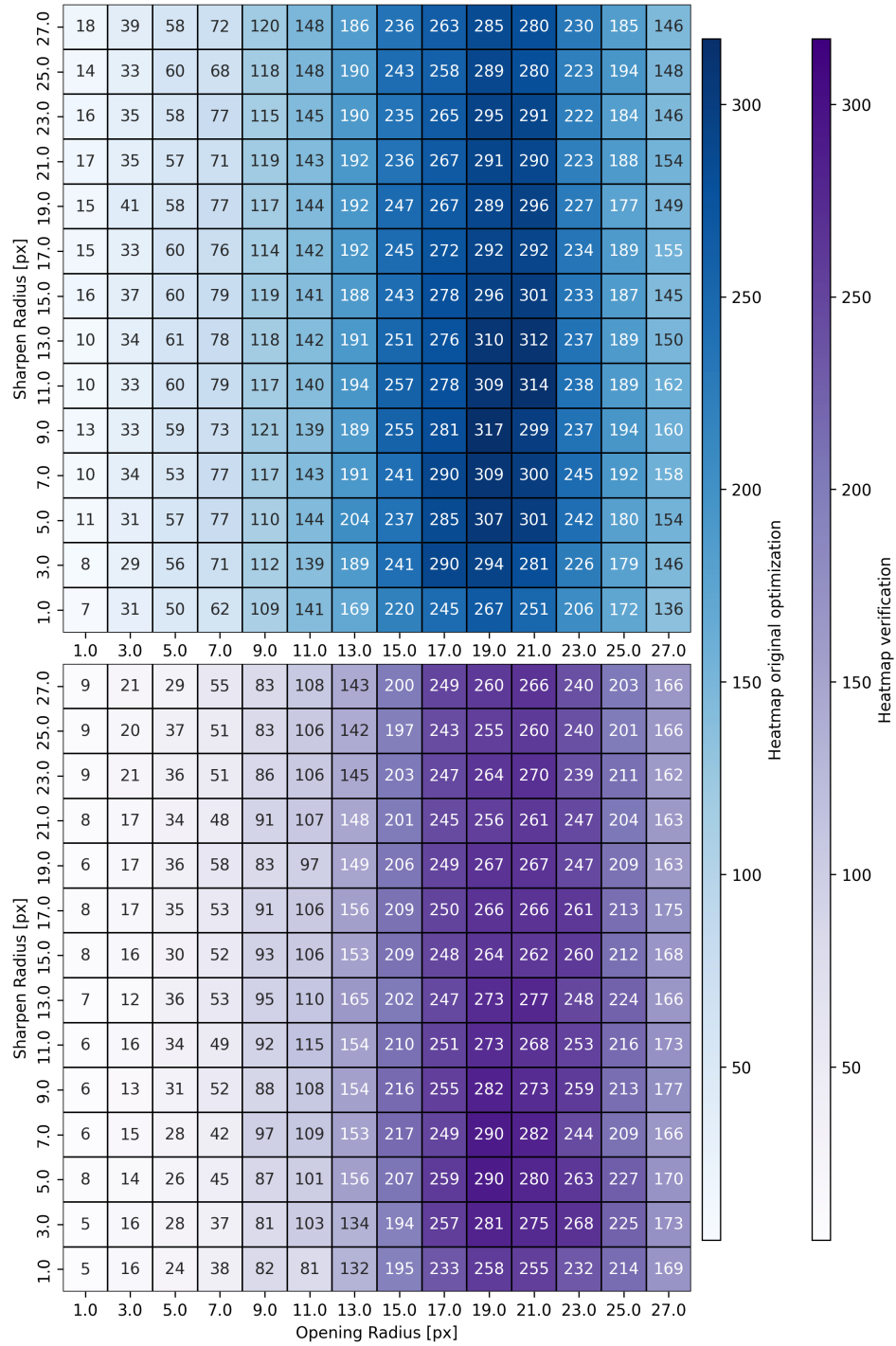


Figure B.2: Number of detected grains for different opening and sharpening radii combinations for medium grains.

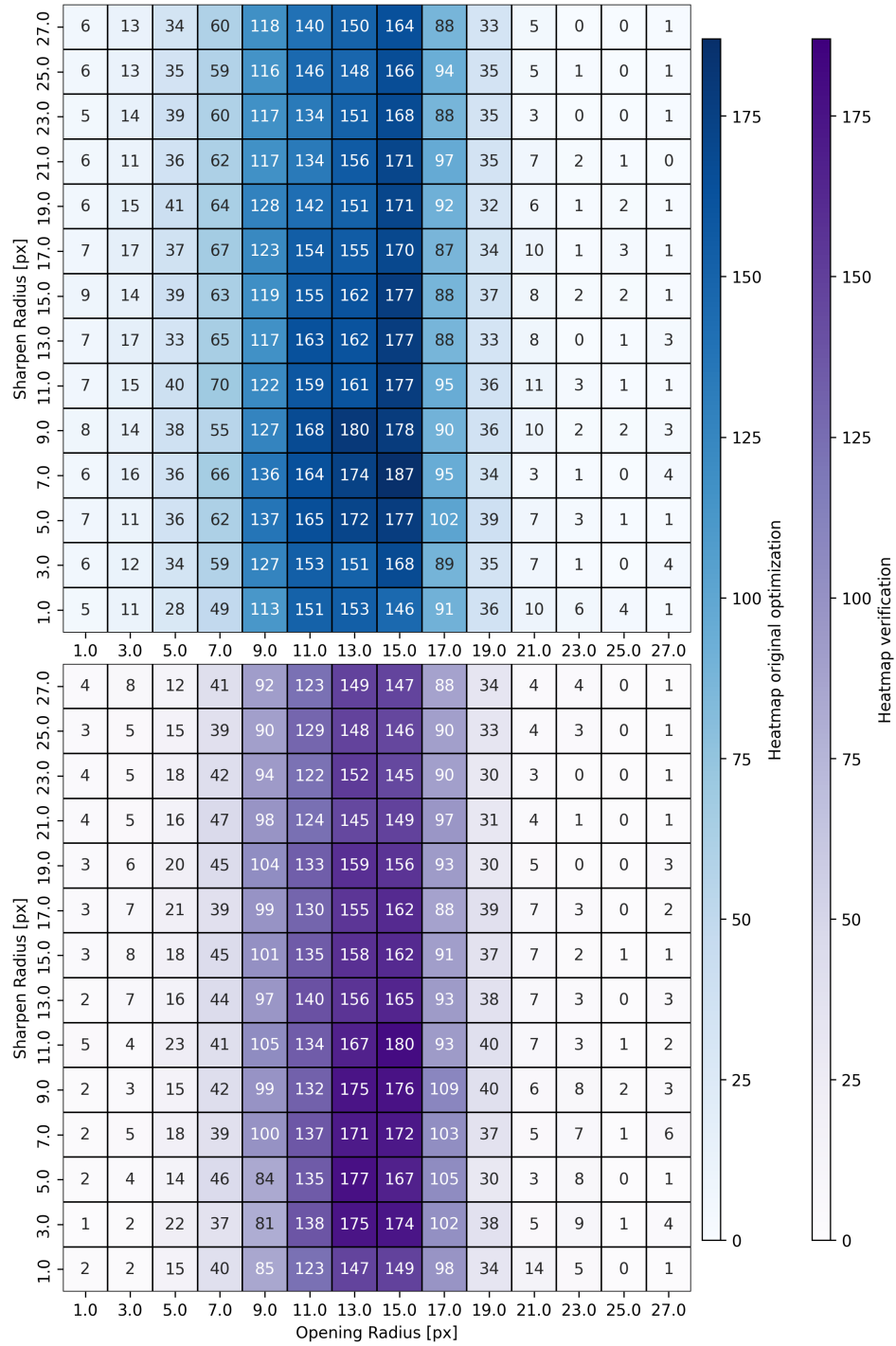


Figure B.3: Number of detected grains for different opening and sharpening radii combinations for small grains.

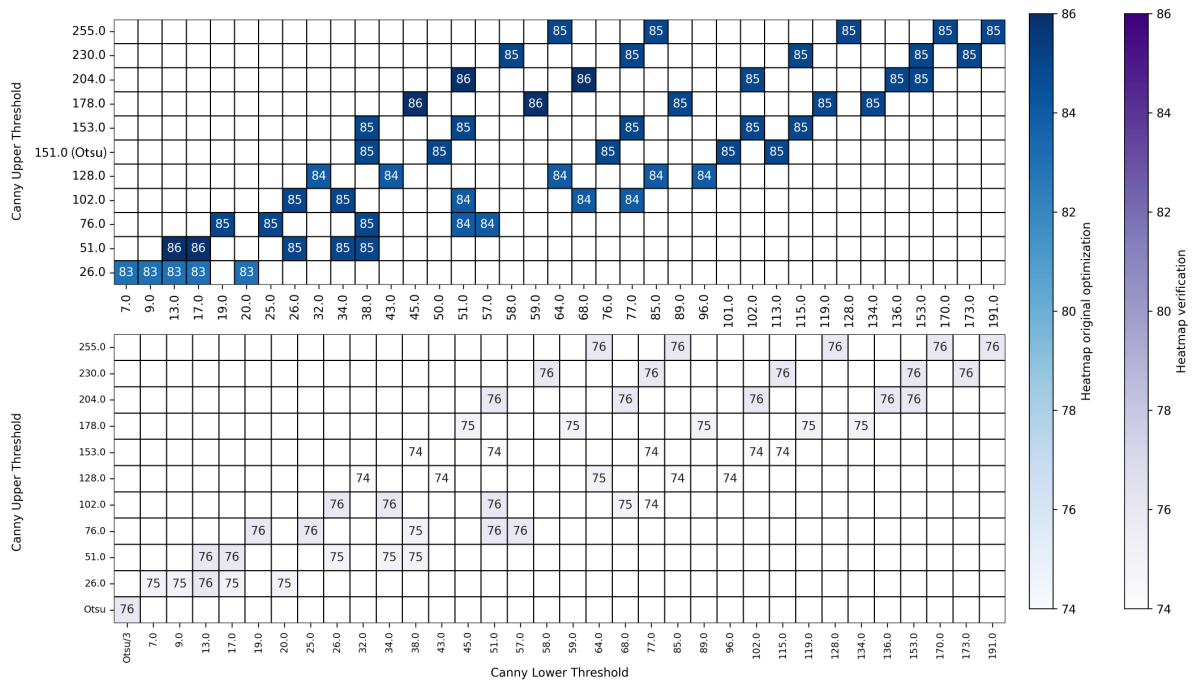


Figure B.4: Number of detected grains for different lower and upper thresholds of canny edge detection for large grains.

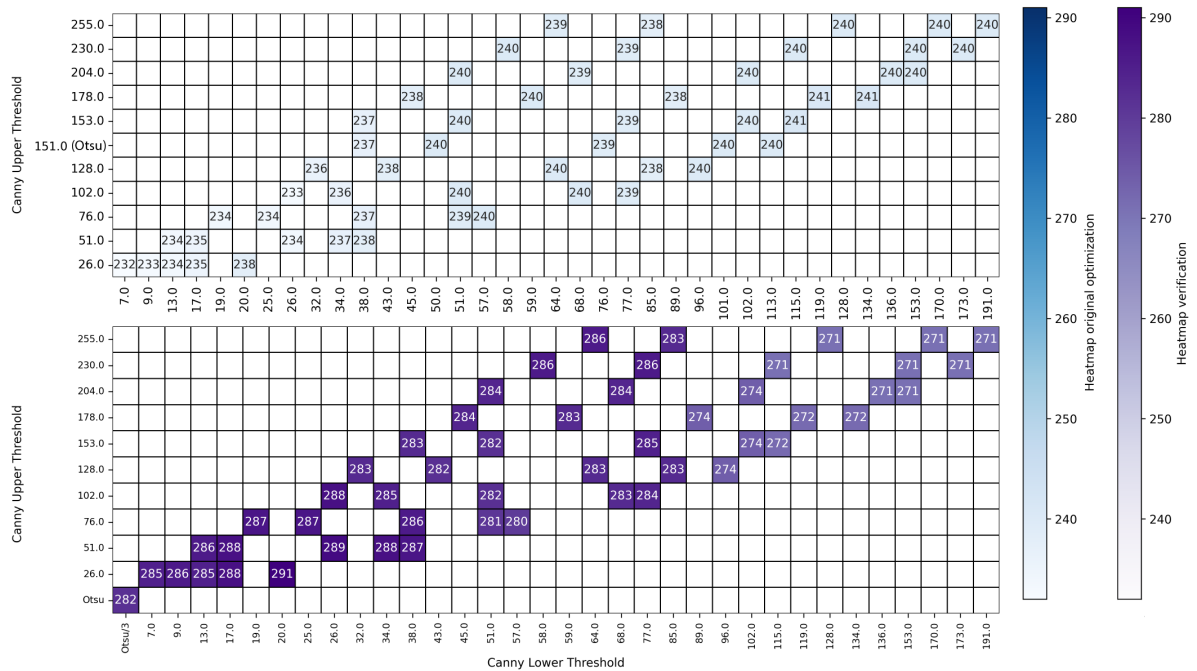


Figure B.5: Number of detected grains for different lower and upper thresholds of canny edge detection for medium grains.

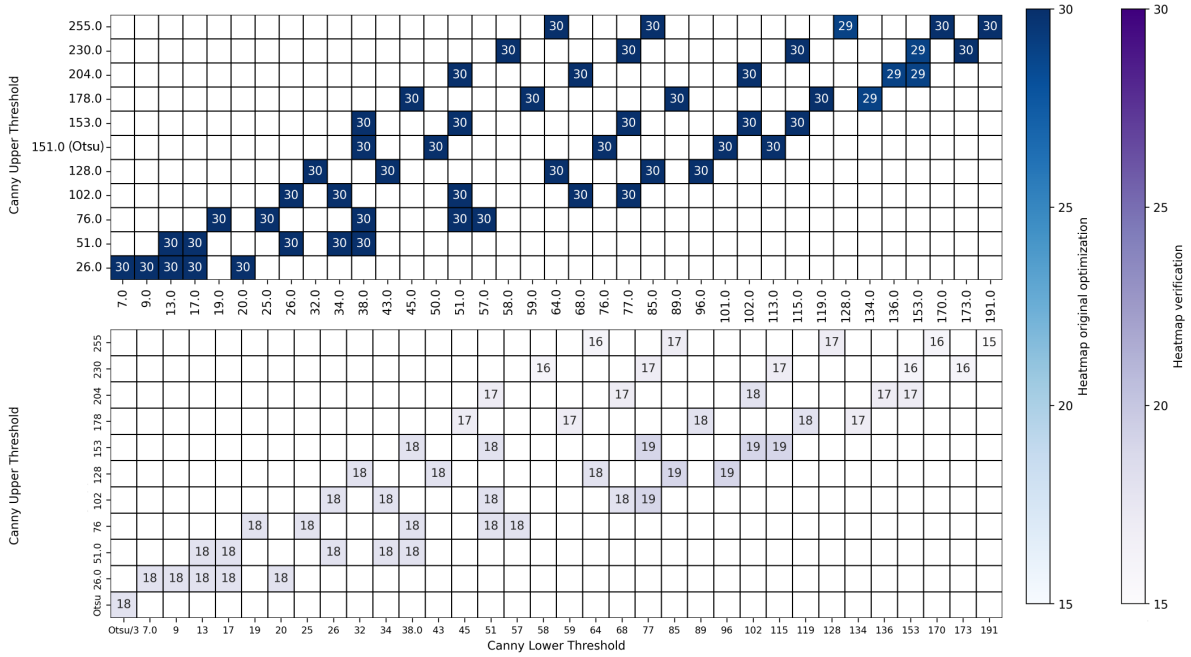


Figure B.6: Number of detected grains for different lower and upper thresholds of canny edge detection for small grains.

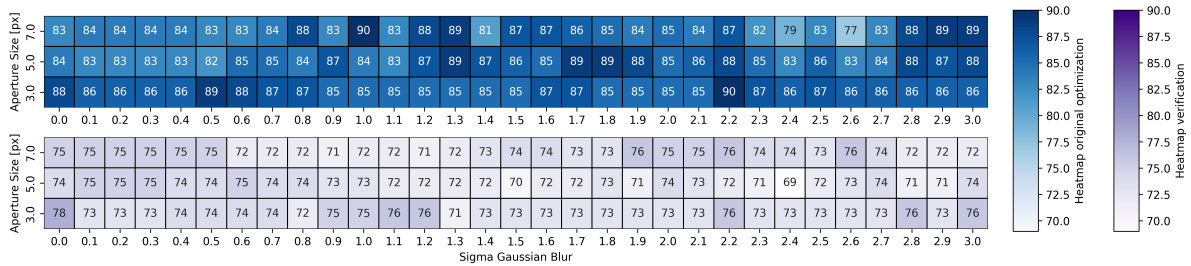


Figure B.7: Number of detected grains for different σ of Gaussian blur and aperture sizes of the Canny edge detection step for large grains.

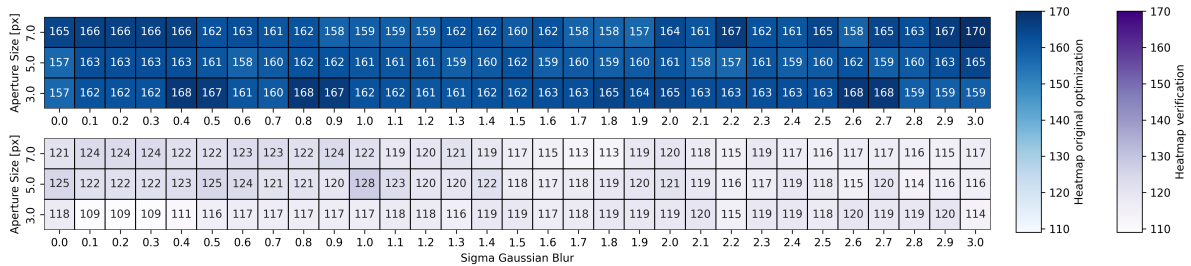


Figure B.8: Number of detected grains for different σ of Gaussian blur and aperture sizes of the Canny edge detection step for medium grains.

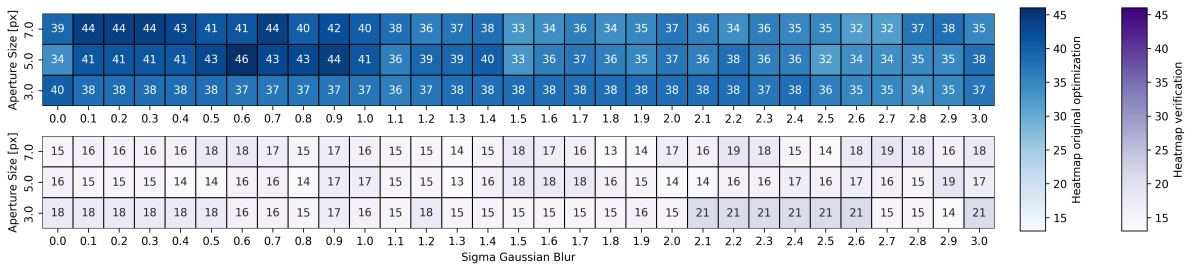


Figure B.9: Number of detected grains for different σ of Gaussian blur and aperture sizes of the Canny edge detection step for small grains.

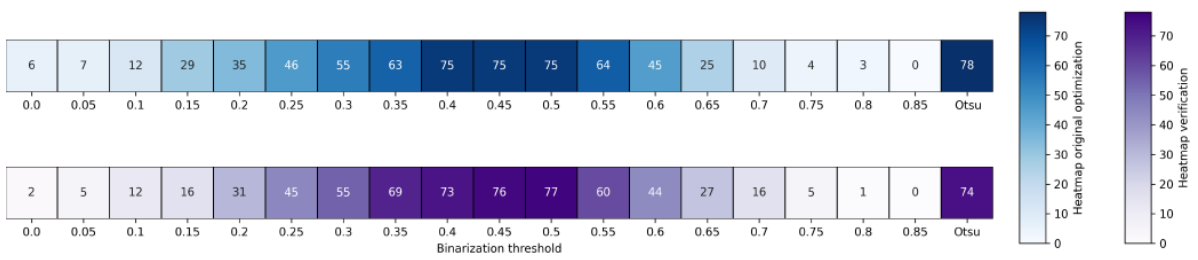


Figure B.10: Number of detected grains for Binarization thresholds for large grains.

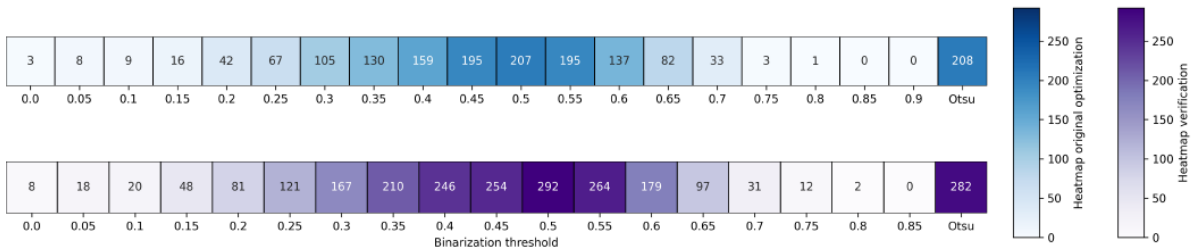


Figure B.11: Number of detected grains for Binarization thresholds for medium grains.

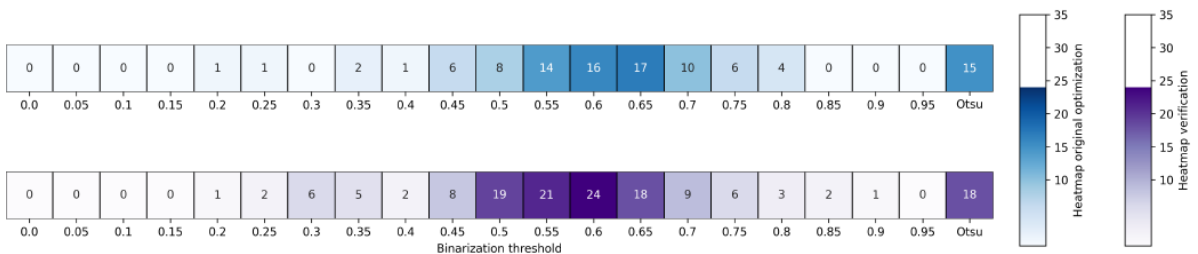


Figure B.12: Number of detected grains for Binarization thresholds for small grains.

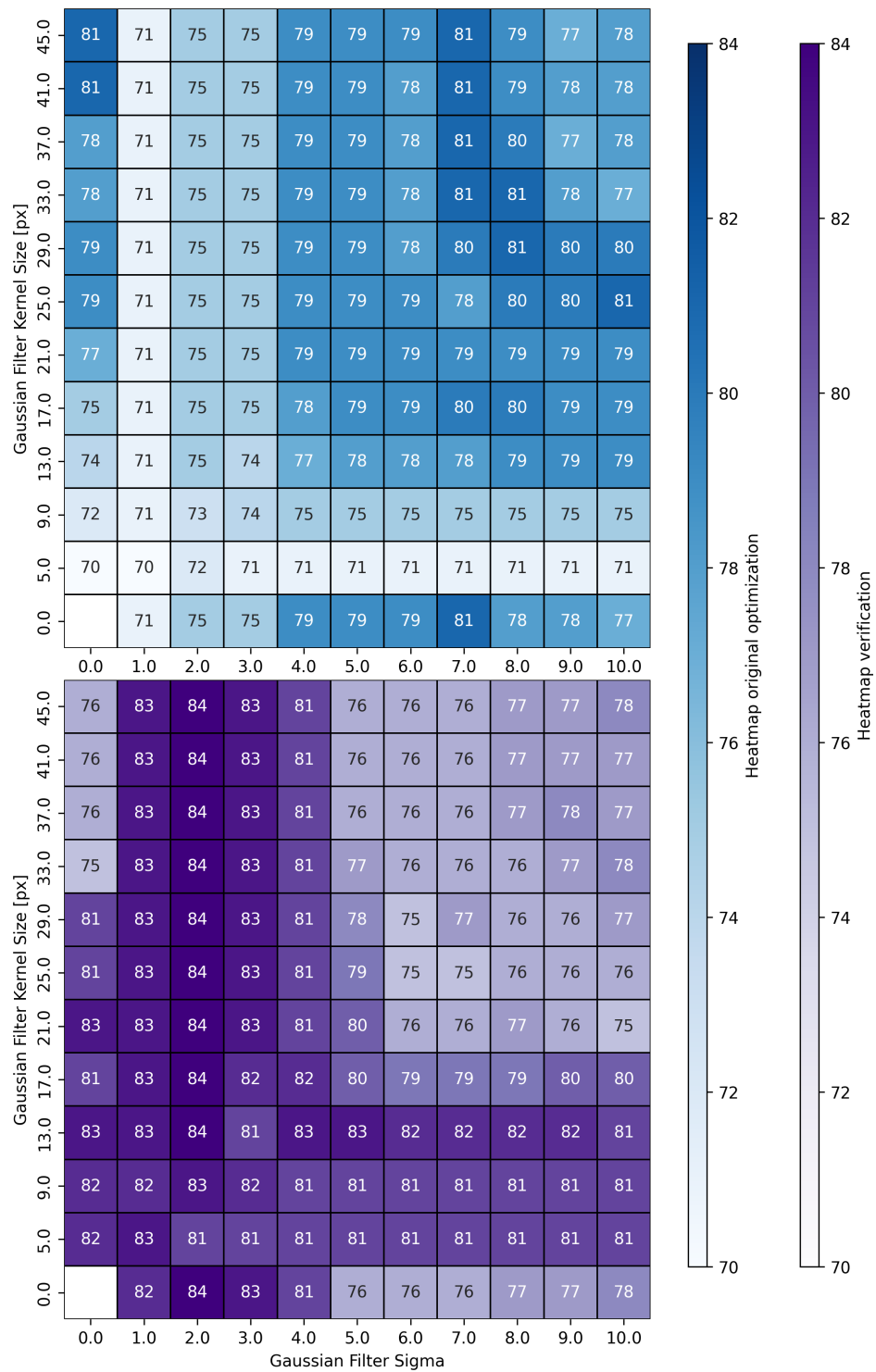


Figure B.13: Number of detected grains for different *kernel* sizes and σ of the Gaussian Filtering step for large grains.

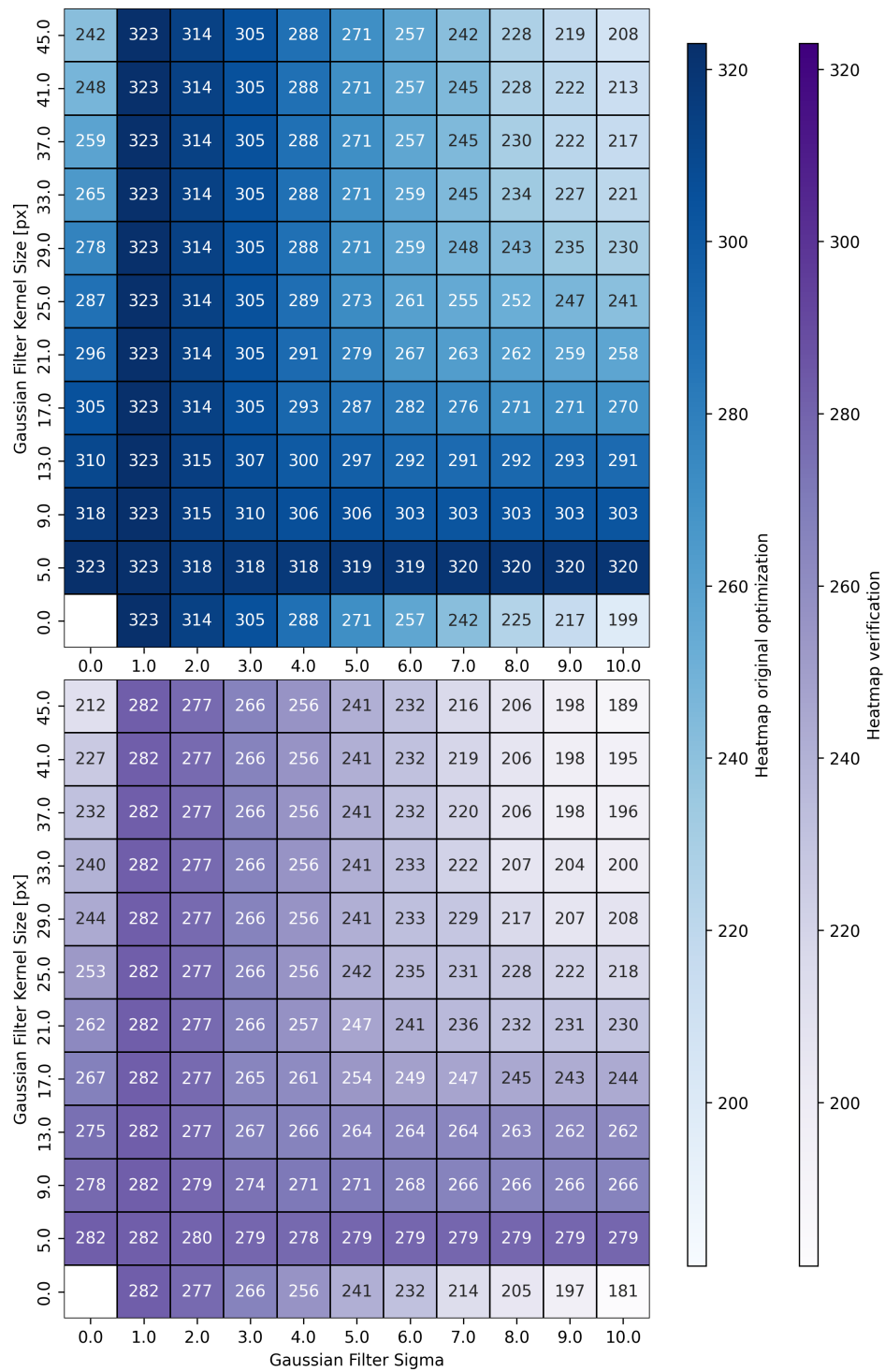


Figure B.14: Number of detected grains for different *kernel sizes* and σ of the Gaussian Filtering step for medium grains.

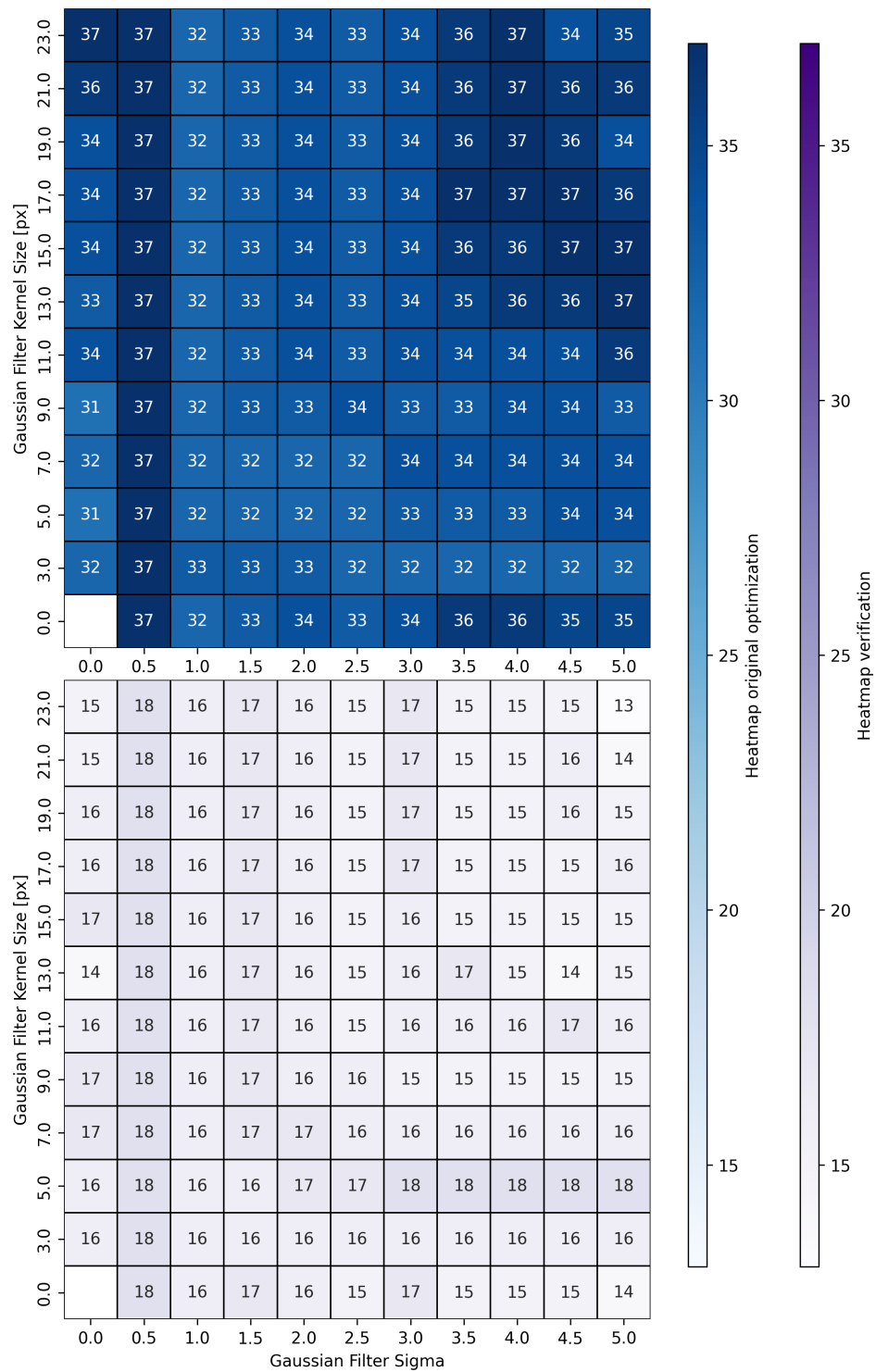


Figure B.15: Number of detected grains for different *kernel* sizes and σ of the Gaussian Filtering step for small grains.

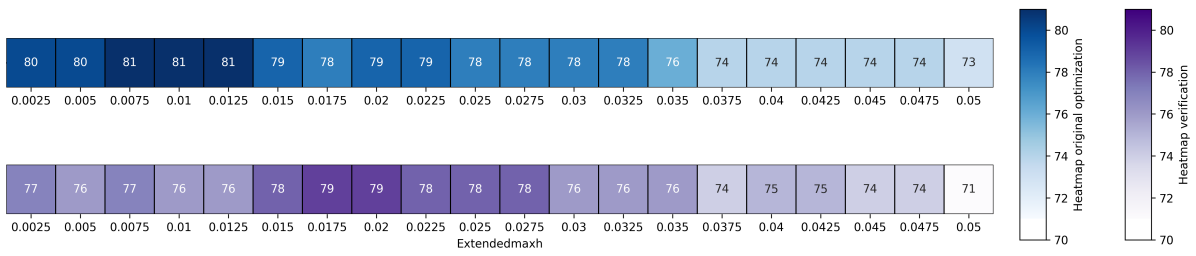


Figure B.16: Number of detected grains for different h-values of the extended maxima step for large grains

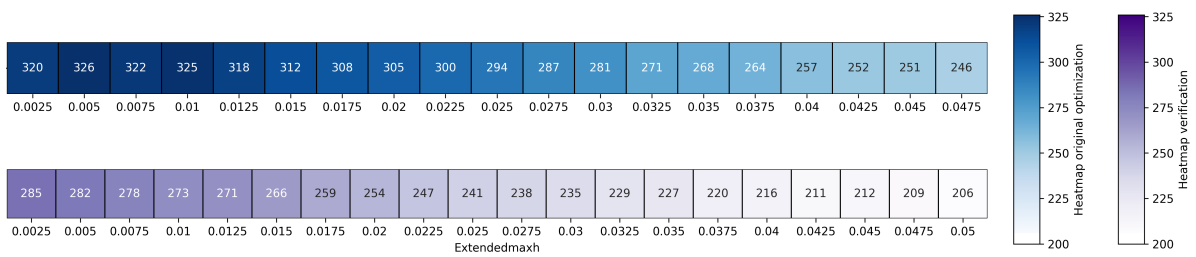


Figure B.17: Number of detected grains for different h-values of the extended maxima step for medium grains.

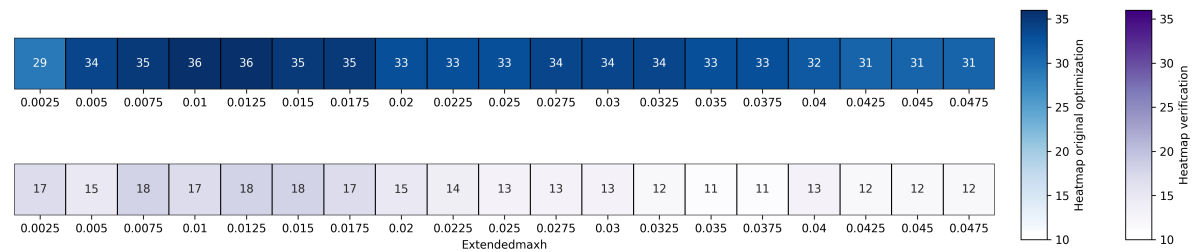
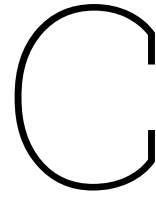


Figure B.18: Number of detected grains for different h-values of the extended maxima step for small grains



Duplicate detections removal procedure

Table C.1 shows the comparison of overlapping contours for four images. For each image, the three grain sizes were compared to each other and it was determined which of the two was correct. The number of correctly identified grains is shown in the table below. The tab *Inconclusive* refers to results that were either both wrong, both correct, or that it was not possible to clearly identify which contour was better, for example if the size of the grain was near the limit between two size classes, both contours would encompass the grain well. Below the table, image 4 is shown before and after removal of duplicates. The blue, red and green contours correspond to the large, medium and small grain classes, respectively.

Table C.1: Determination of correctness for overlapping contours.

Image	Comparison	Larger correct	Smaller correct	Inconclusive
1	Large - Medium	8	7	5
	Medium - Small	4	4	1
	Large - Small	0	0	0
2	Large - Medium	7	4	8
	Medium - Small	1	1	1
	Large - Small	0	0	0
3	Large - Medium	4	3	8
	Medium - Small	2	4	0
	Large - Small	0	1	0
4	Large - Medium	1	9	7
	Medium - Small	0	7	1
	Large - Small	0	0	0
Total	Large - Medium	20	23	28
	Medium - Small	7	16	3
	Large - Small	0	1	0

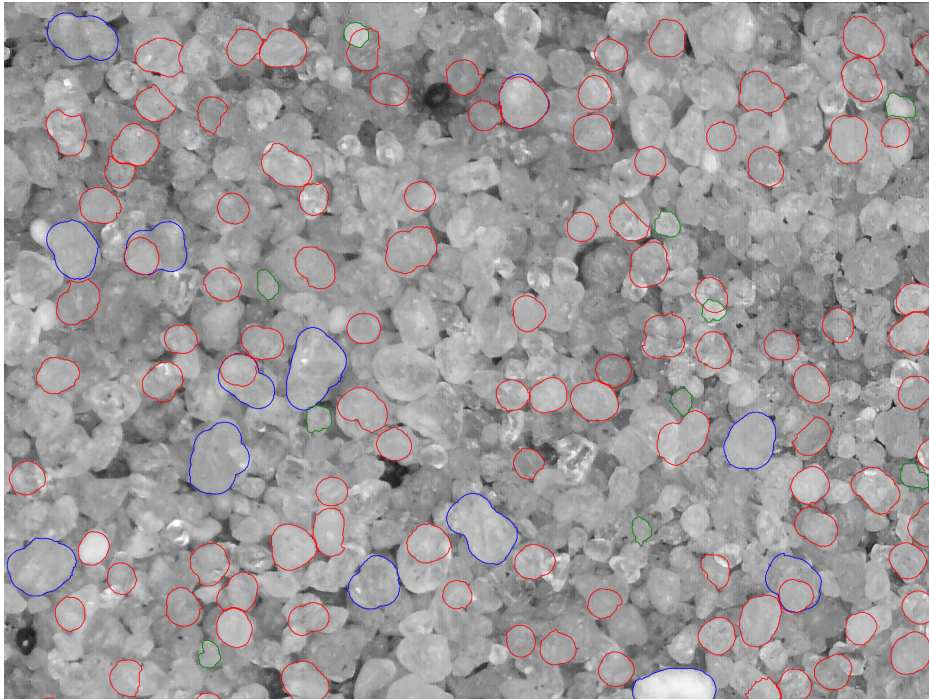


Figure C.1: Microscope image of experiment at Mars equivalent pressure (14 mbar) 120% threshold after reaching maximum rippling, row 2, position -3, before removing duplicates

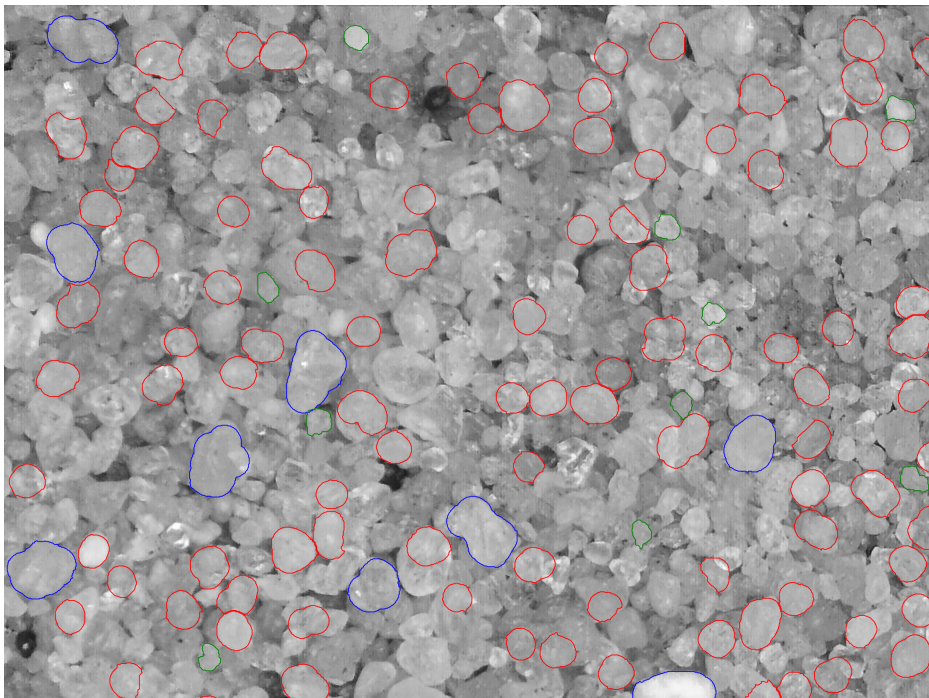


Figure C.2: Microscope image of experiment at Mars equivalent pressure (14 mbar) 120% threshold after reaching maximum rippling, row 2, position -3, after removal of 6 duplicates.

D

Windroses of each image

Below, for each of the ten experiments a grid of windroses is shown, for a lower elongation limit of 1.1. The windroses correspond to the grid of images taken of the sandbed. The flow direction is N-S, N indicates the number of grains and R the fabric strength.

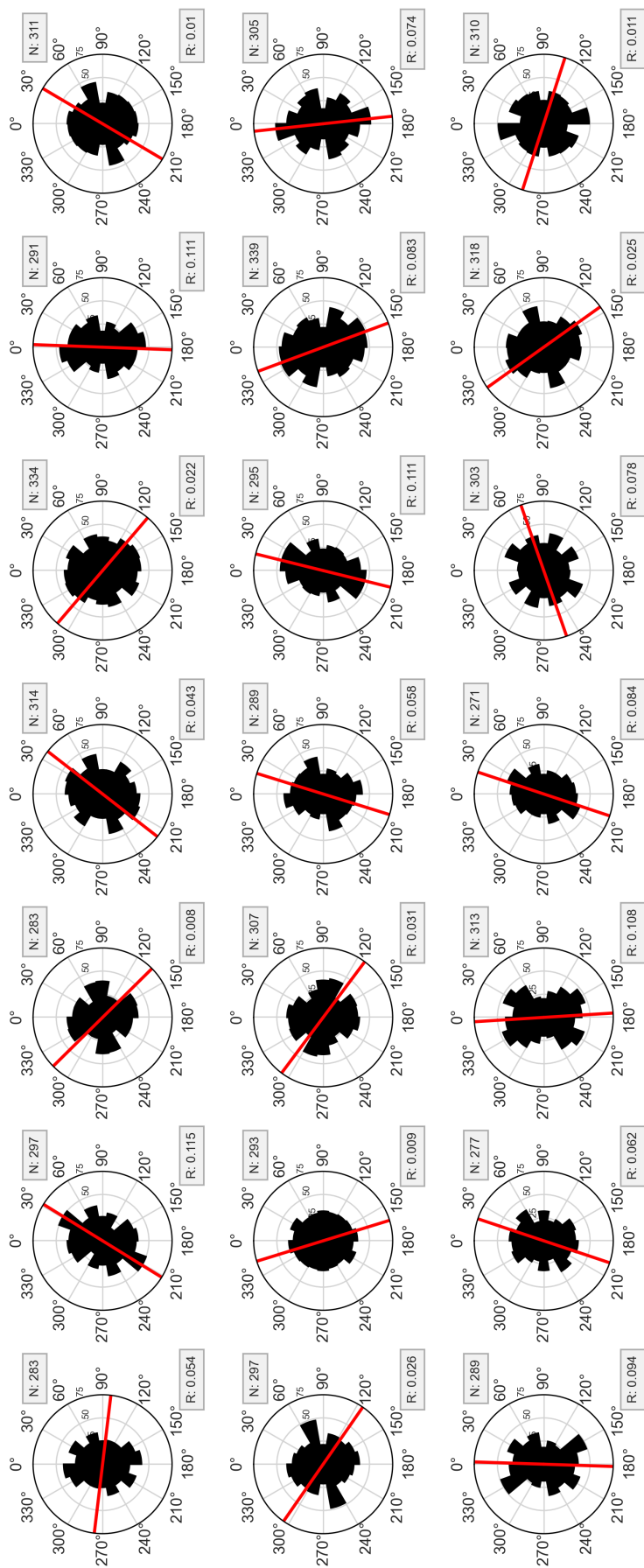


Figure D.1: Grid of windroses of the experiment at 1000 mbar and at 120% u_4 . Each windrose describes the orientations in one image, with the grid corresponding to the physical grid of images taken in the wind tunnel. The red line coincides with the determined preferred orientation. N and R are the number of grains and the fabric strength, respectively.

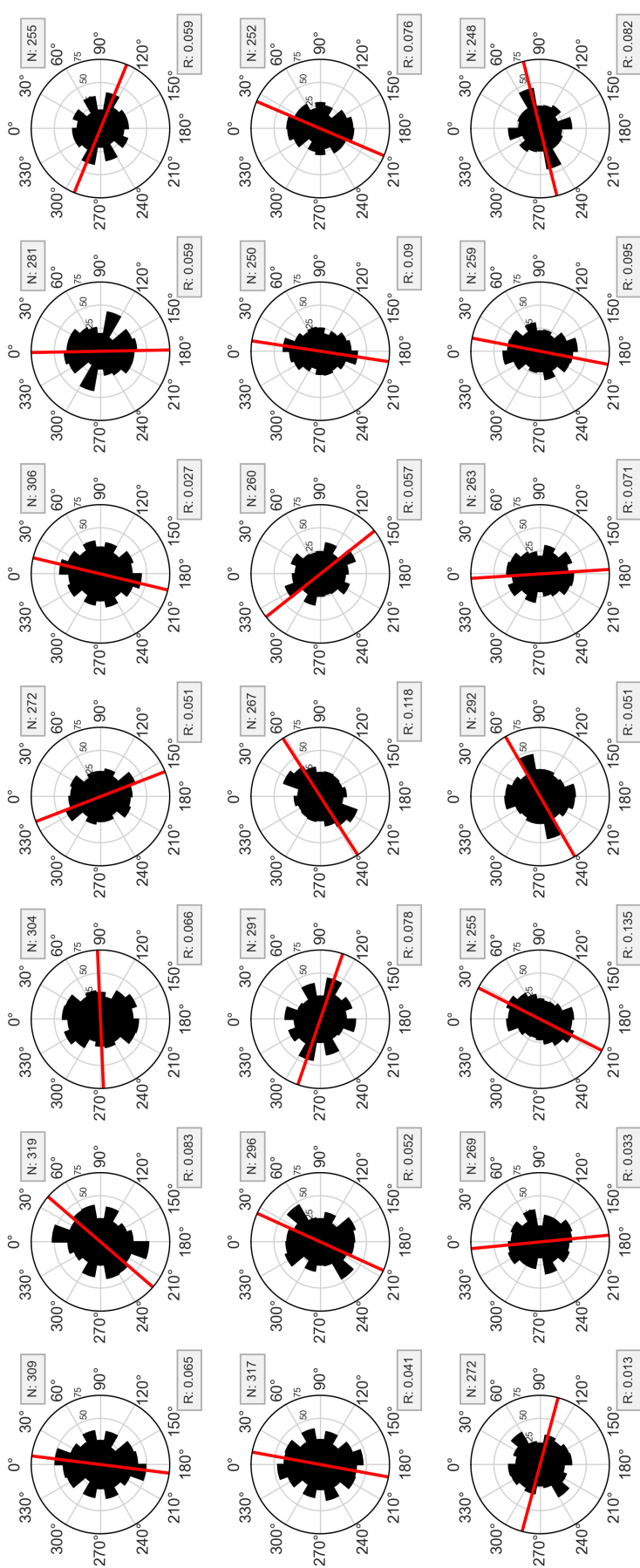


Figure D.2: Grid of windroses of the experiment at 1000 mbar and at 120% u_{4t} . Each windrose describes the orientations in one image, with the grid corresponding to the physical grid of images taken in the wind tunnel. The red line coincides with the determined preferred orientation. N and R are the number of grains and the fabric strength, respectively.

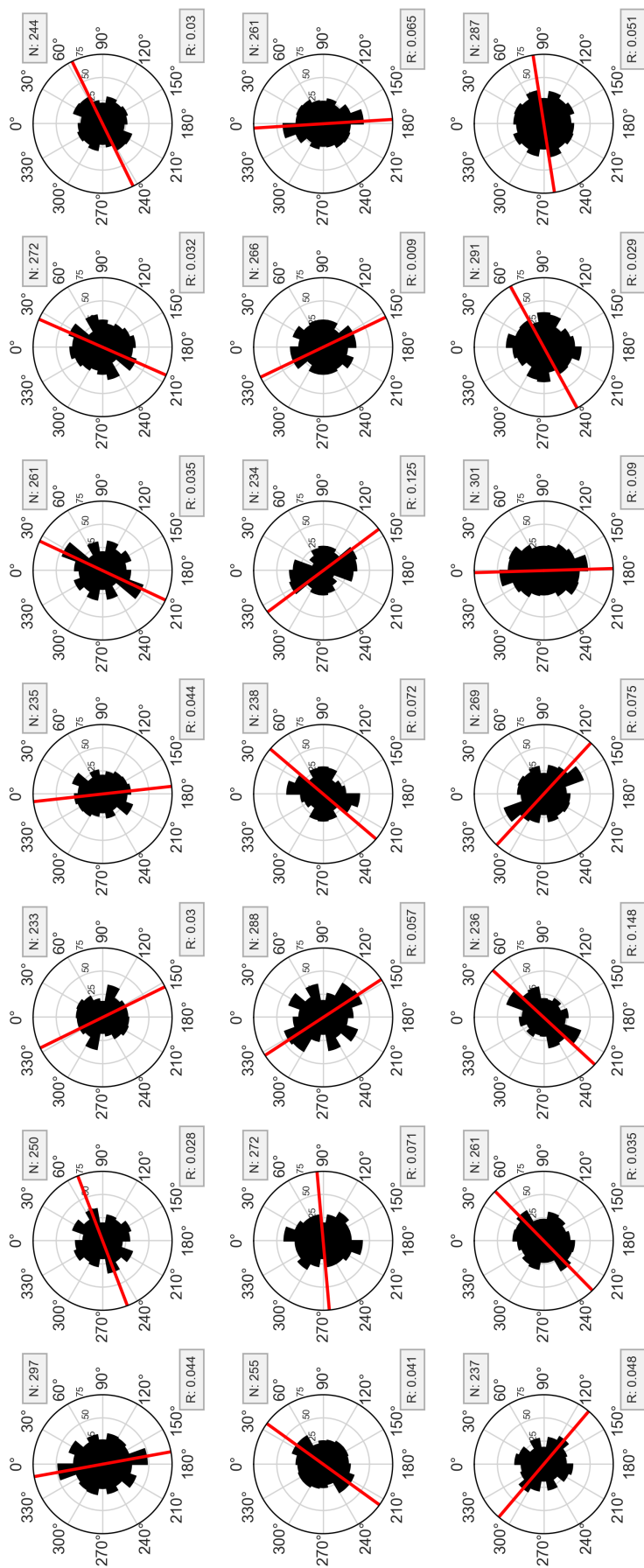


Figure D.3: Grid of windroses of the experiment at 720 mbar and 120% u_{*t} . Each windrose describes the orientations in one image, with the grid corresponding to the physical grid of images taken in the wind tunnel. The red line coincides with the determined preferred orientation. N and R are the number of grains and the fabric strength, respectively.

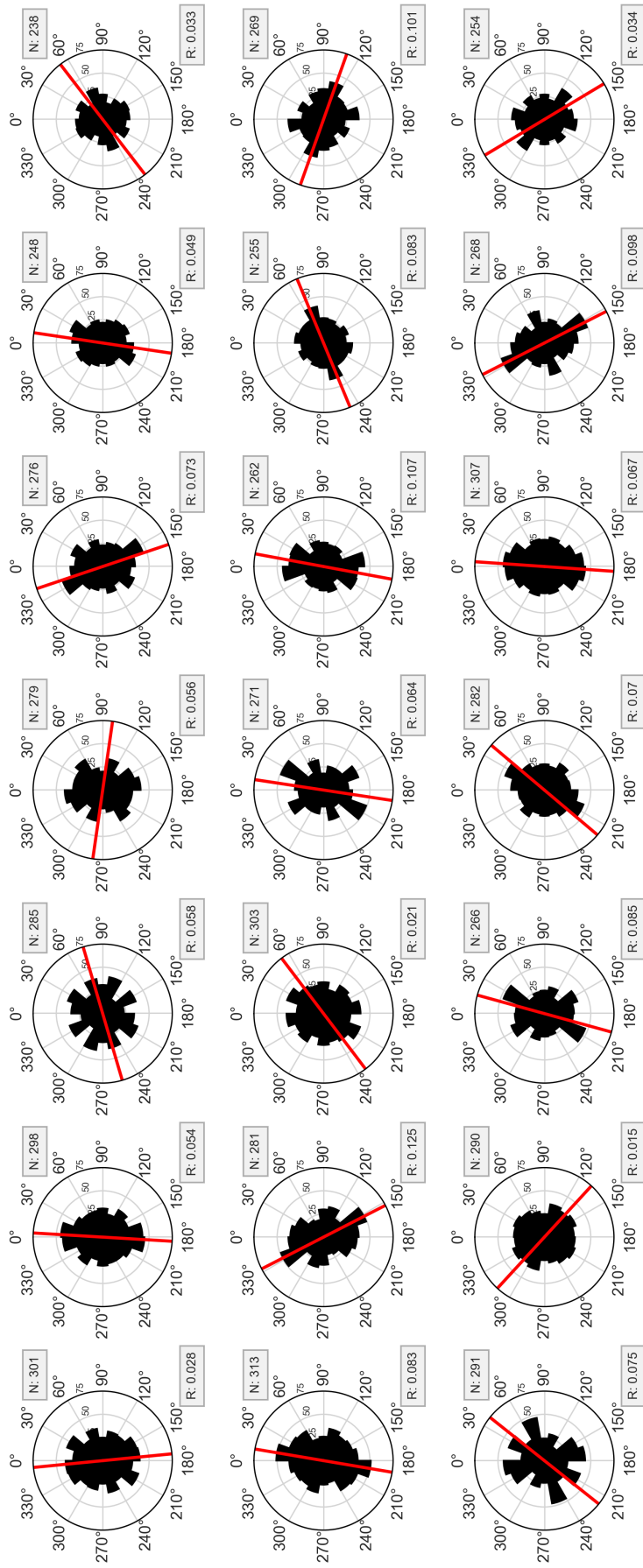


Figure D.4: Grid of windroses of the experiment at 720 mbar and 120% u_{*t} . Each windrose describes the orientations in one image, with the grid corresponding to the physical grid of images taken in the wind tunnel. The red line coincides with the determined preferred orientation. N and R are the number of grains and the fabric strength, respectively.

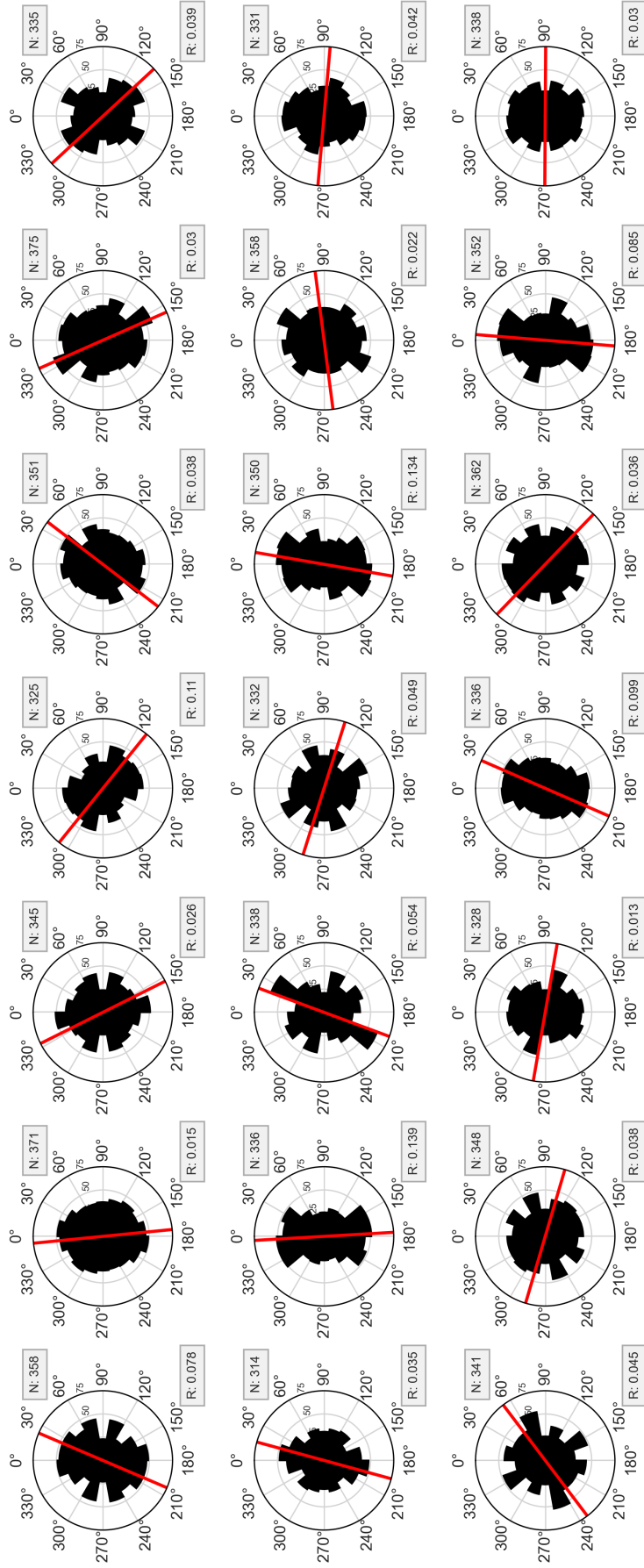


Figure D.5: Grid of windroses of the experiment at 480 mbar and 120% u_{*t} . Each windrose describes the orientations in one image, with the grid corresponding to the physical grid of images taken in the wind tunnel. The red line coincides with the determined preferred orientation. N and R are the number of grains and the fabric strength, respectively.

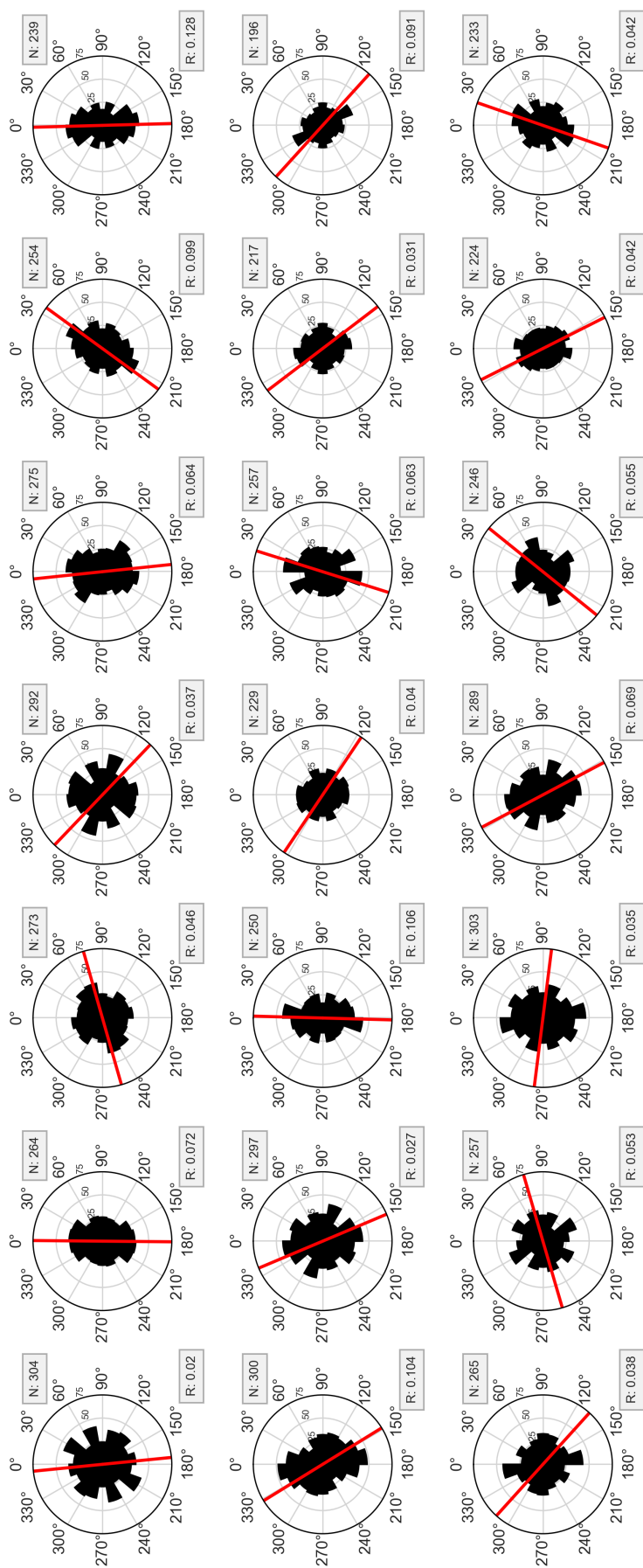


Figure D.6: Grid of windroses of the experiment at 480 mbar and 150% u_{*t} . Each windrose describes the orientations in one image, with the grid corresponding to the physical grid of images taken in the wind tunnel. The red line coincides with the determined preferred orientation. N and R are the number of grains and the fabric strength, respectively.

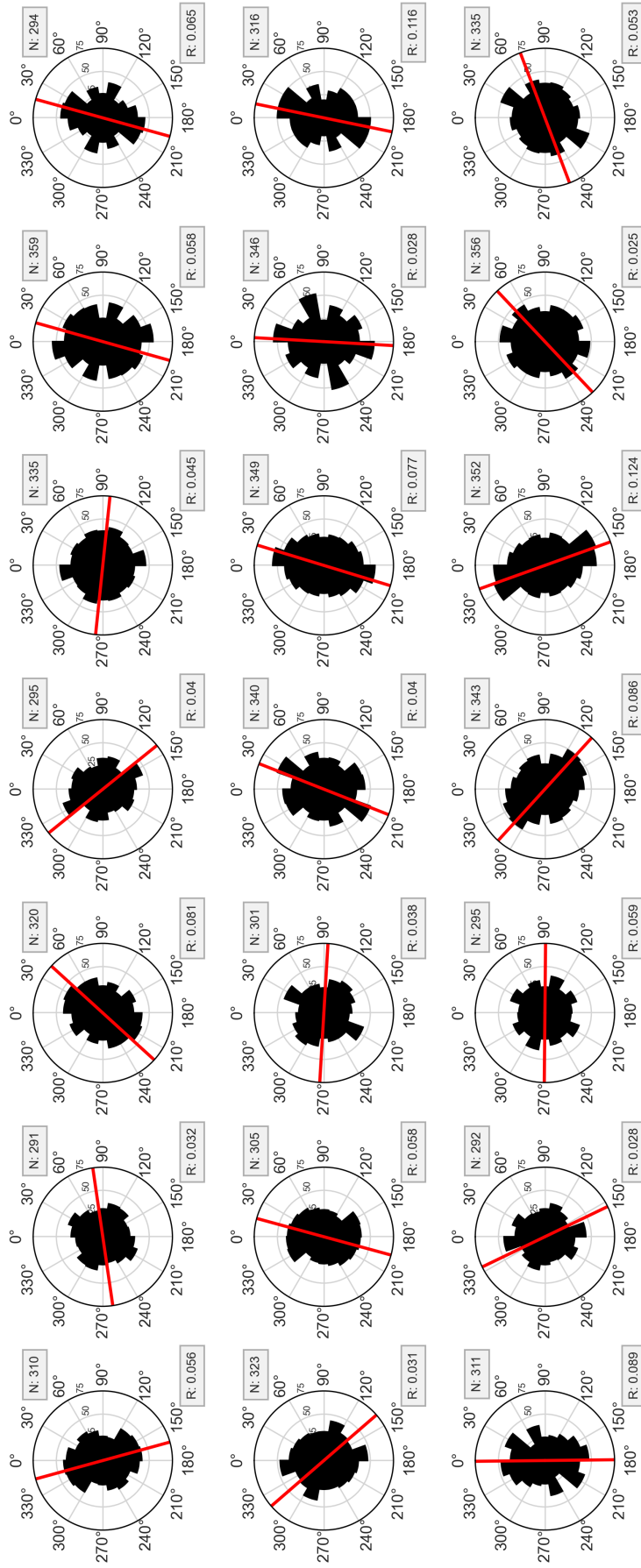


Figure D.7: Grid of windroses of the experiment at 240 mbar and at 120% u_{*t} . Each windrose describes the orientations in one image, with the grid corresponding to the physical grid of images taken in the wind tunnel. The red line coincides with the determined preferred orientation. N and R are the number of grains and the fabric strength, respectively.

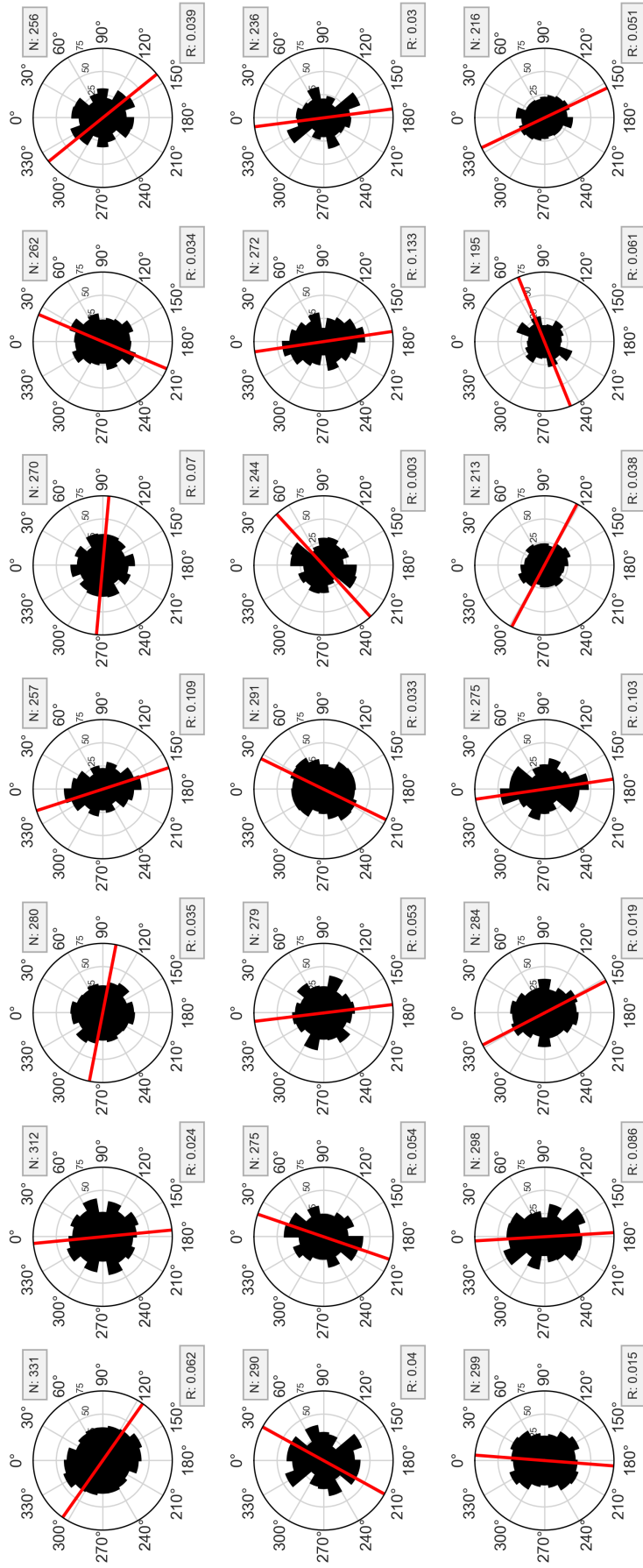


Figure D.8: Grid of windroses of the experiment at 240 mbar and 120% u_{*t} . Each windrose describes the orientations in one image, with the grid corresponding to the physical grid of images taken in the wind tunnel. The red line coincides with the determined preferred orientation. N and R are the number of grains and the fabric strength, respectively.

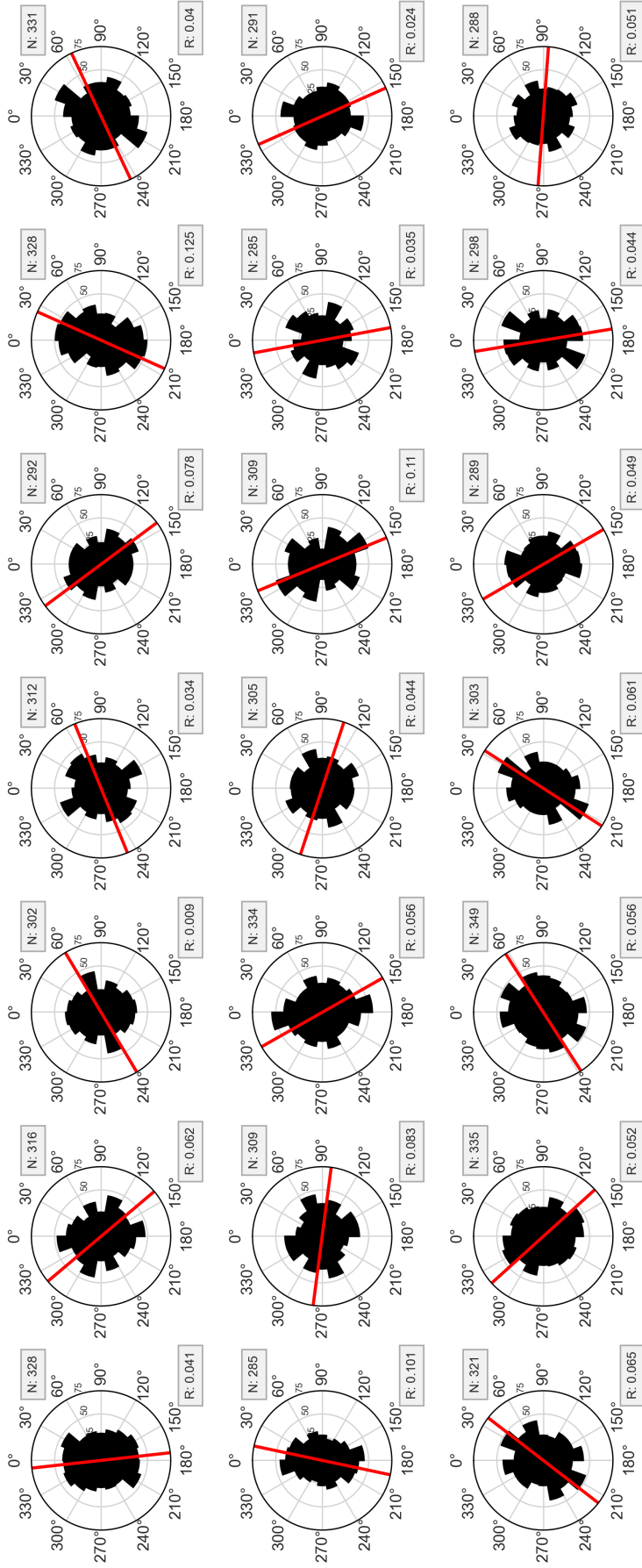


Figure D.9: Grid of windroses of the experiment under Martian pressure at $120\% u_{4f}$. Each windrose describes the orientations in one image, with the grid corresponding to the physical grid of images taken in the wind tunnel. The red line coincides with the determined preferred orientation. N and R are the number of grains and the fabric strength, respectively.

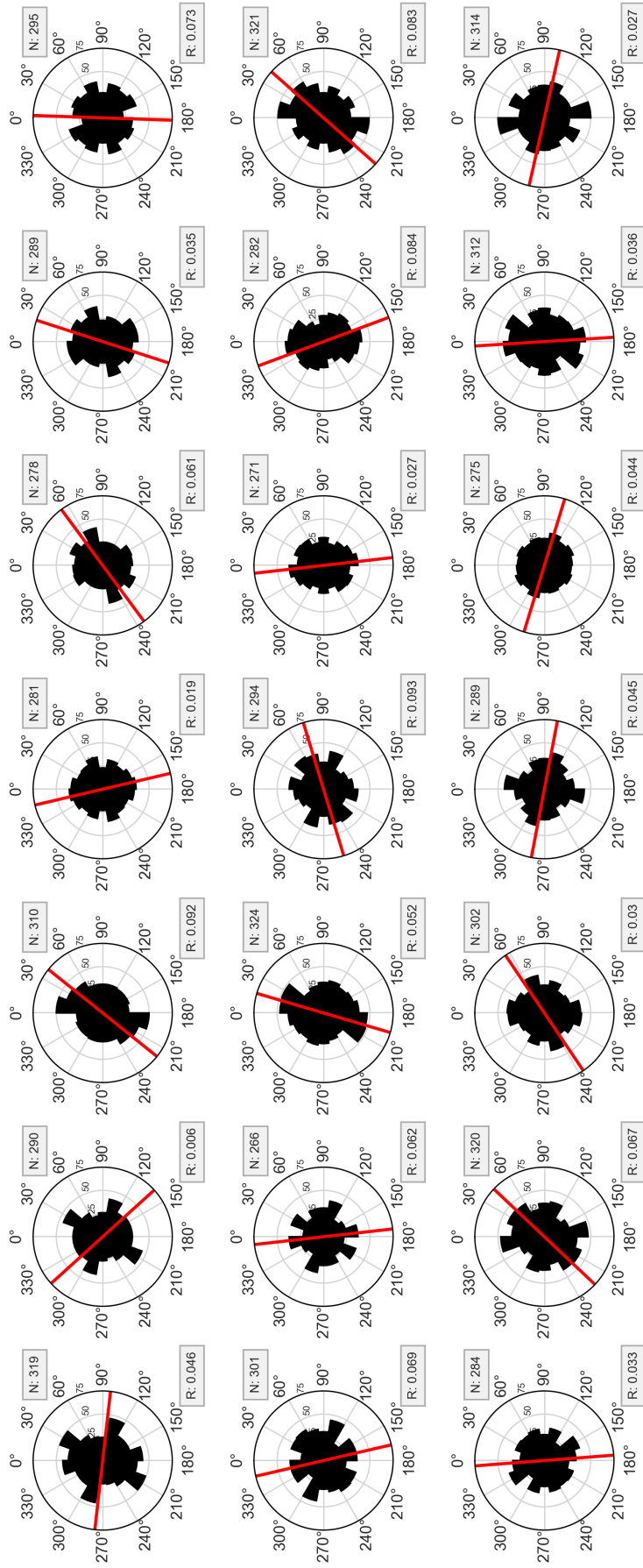


Figure D.10: Grid of windroses of the experiment under Martian pressure at 150% u_t . Each windrose describes the orientations in one image, with the grid corresponding to the physical grid of images taken in the wind tunnel. The red line coincides with the determined preferred orientation. N and R are the number of grains and the fabric strength, respectively.

E

Total windroses of each experiment

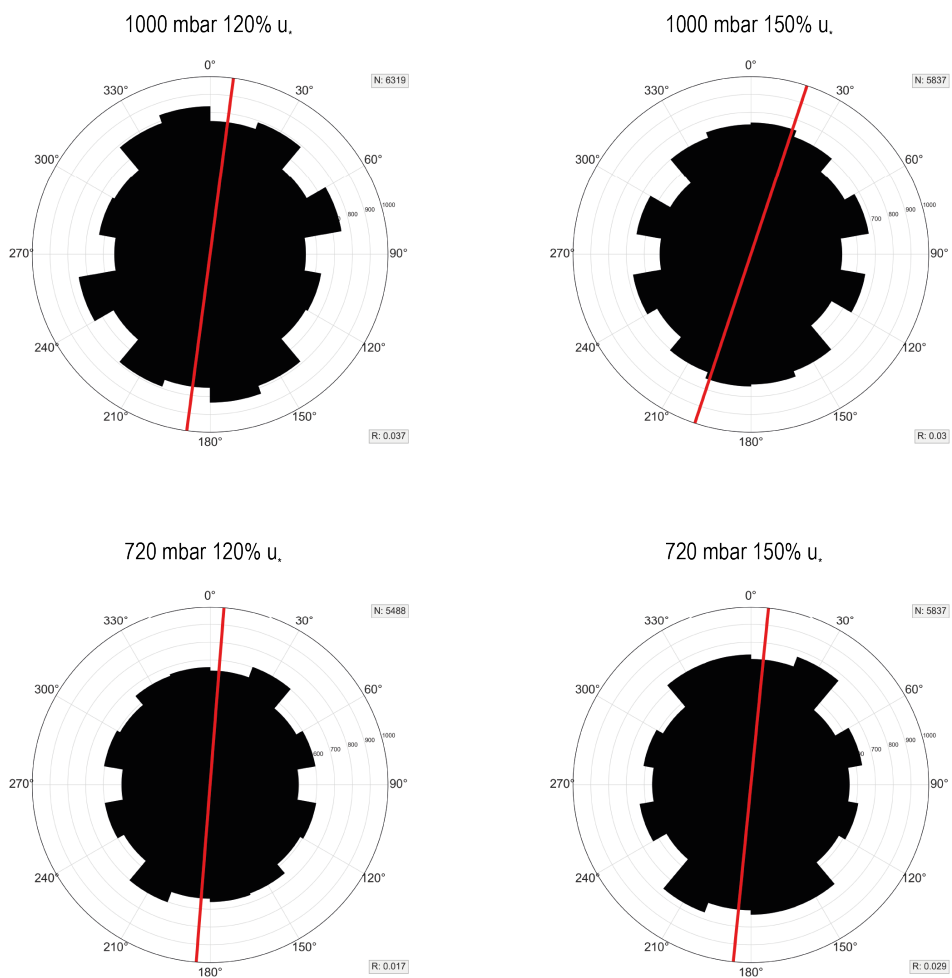


Figure E.1: Windroses of the experiment at 1000 and 720 *mbar*, combining 21 measurements. The red line coincides with the determined preferred orientation

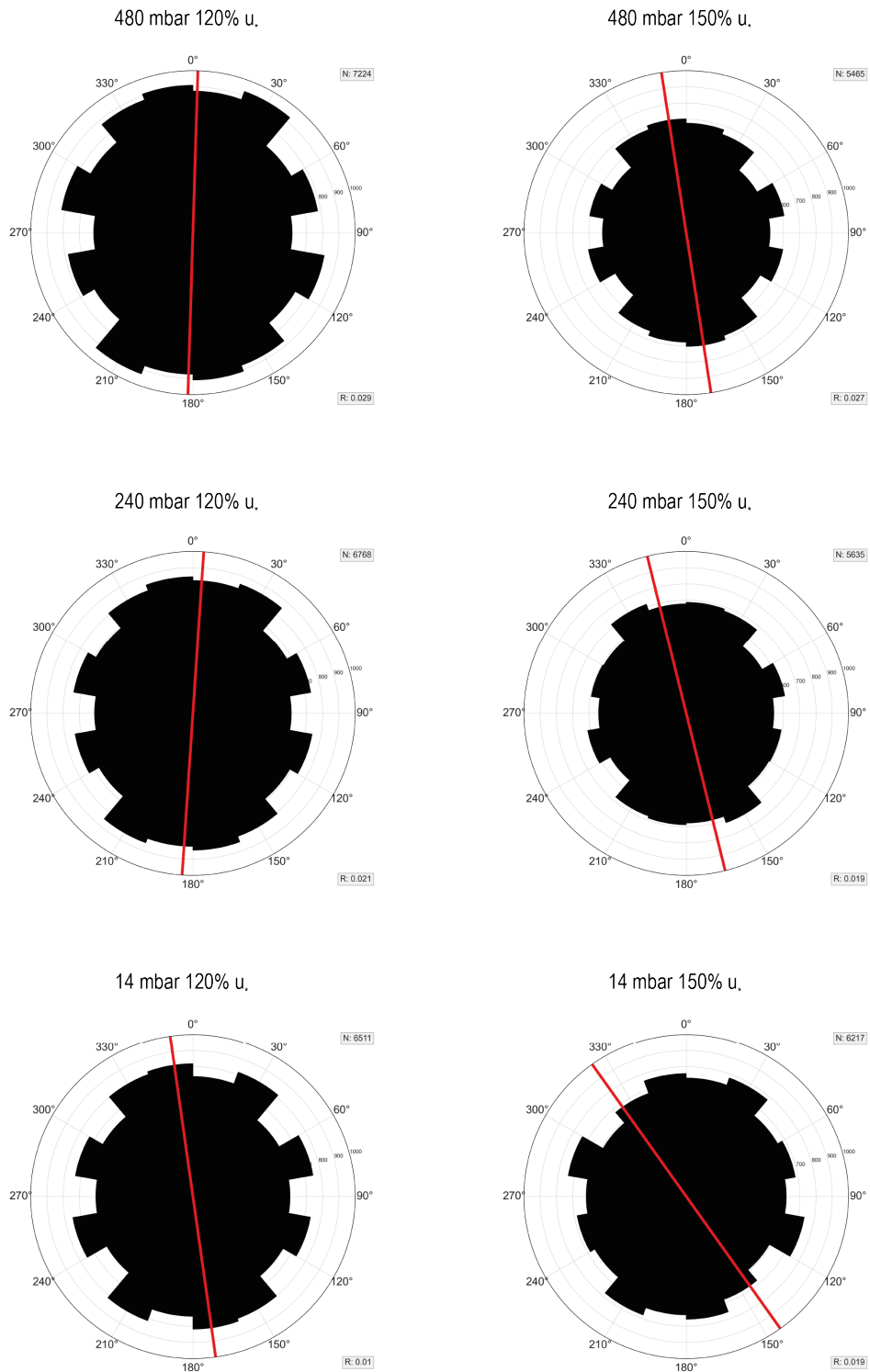


Figure E.2: Windroses of each experiment at 480, 240 and 14 *mbar*, combining 21 measurements. The red line coincides with the determined preferred orientation

F

Box plots of number of grains and
fabric strength

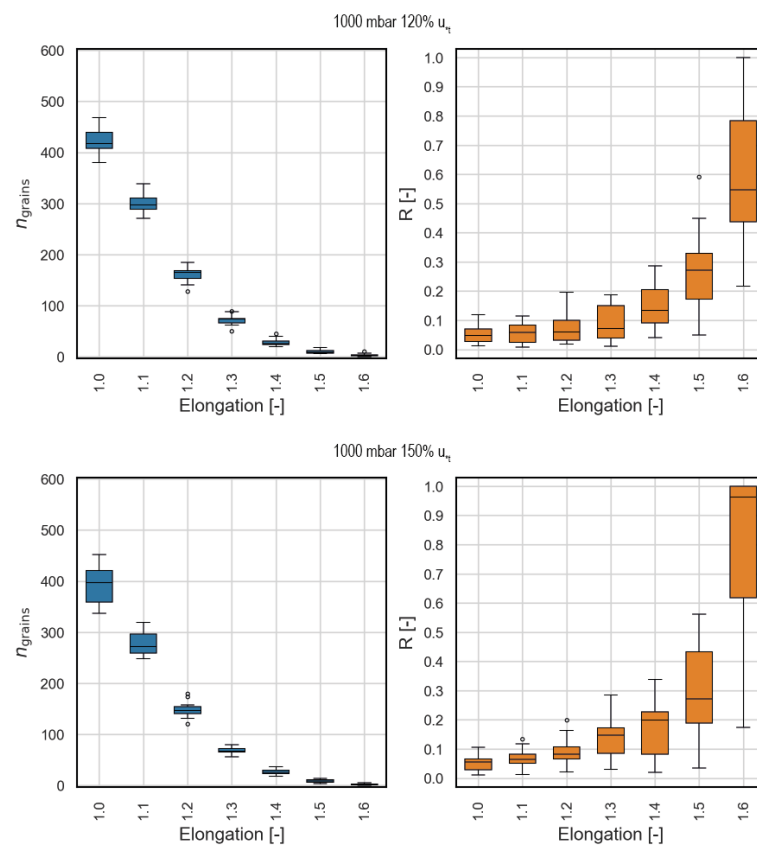


Figure F.1: Box plots of the number of grains and fabric strength for each lower limit on grain elongation for the experiments under ambient pressure.

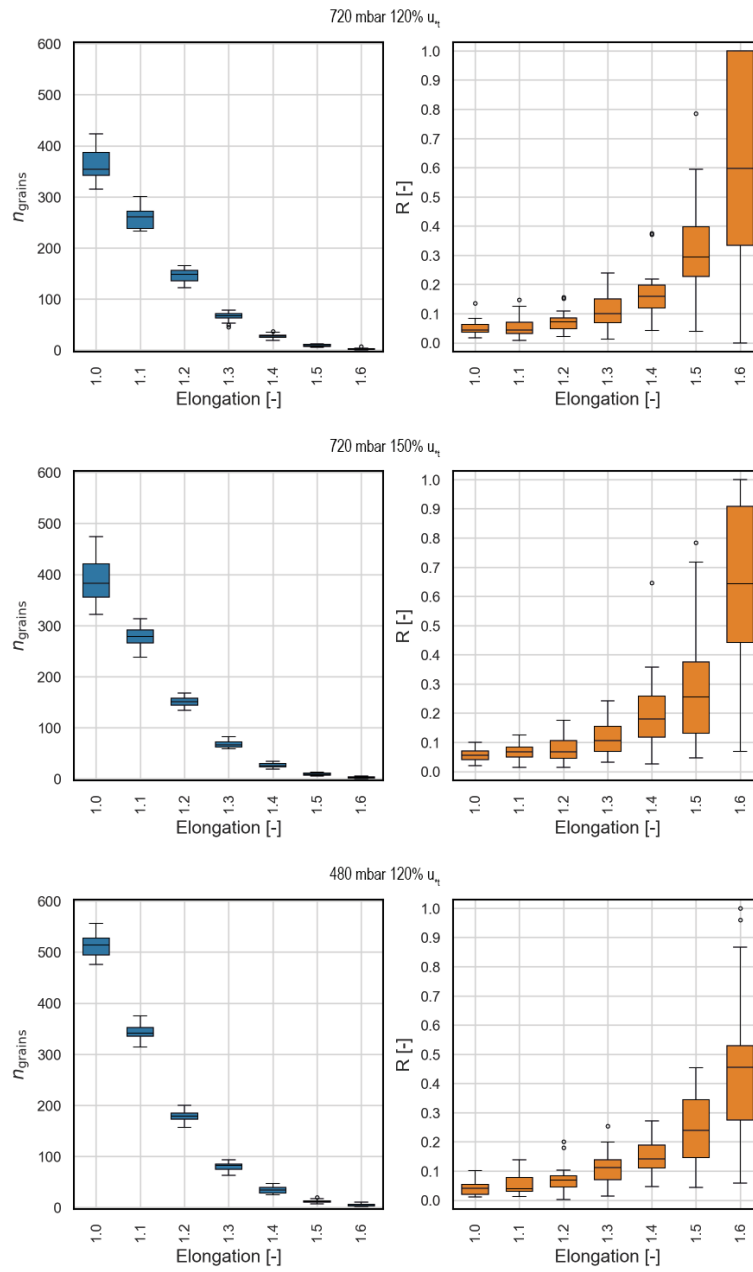


Figure F.2: Box plots of the number of grains and fabric strength for each lower limit on grain elongation for the experiments at 720 mbar and one at 480 mbar.

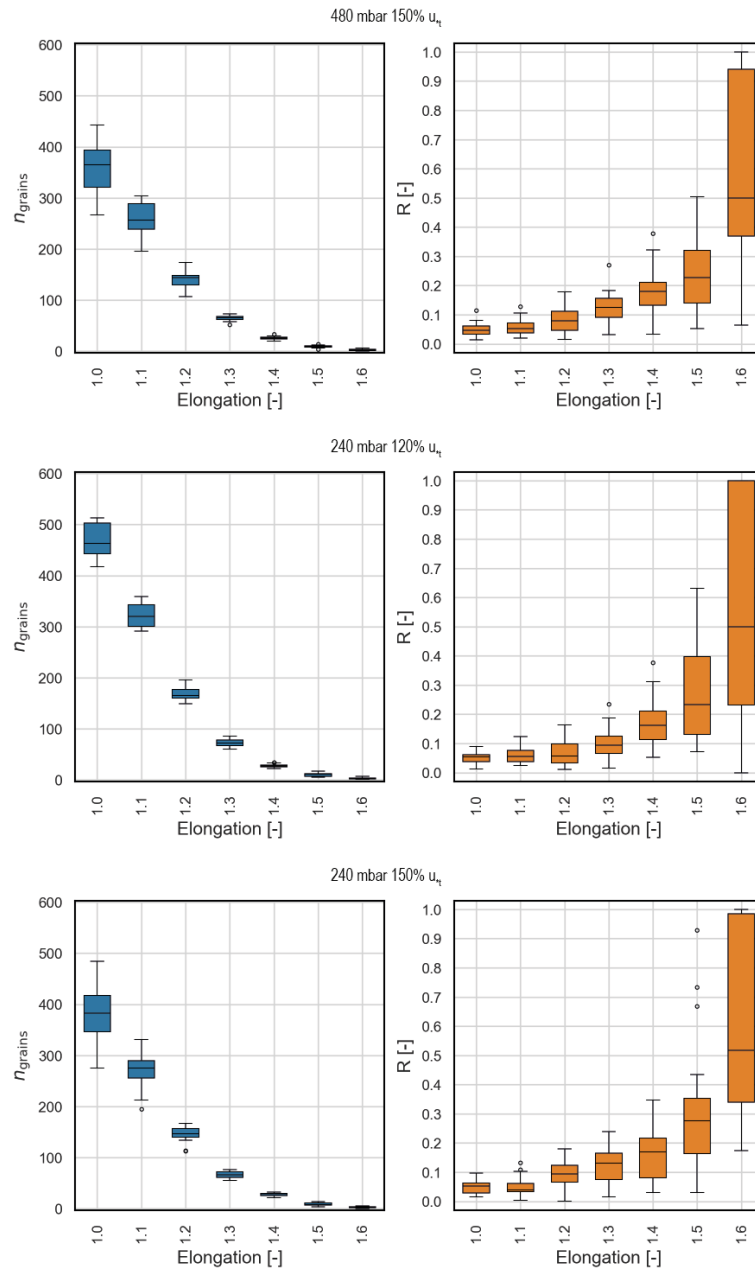


Figure F.3: Box plots of the number of grains and fabric strength for each lower limit on grain elongation for the experiments 240 mbar and one at 480 mbar.

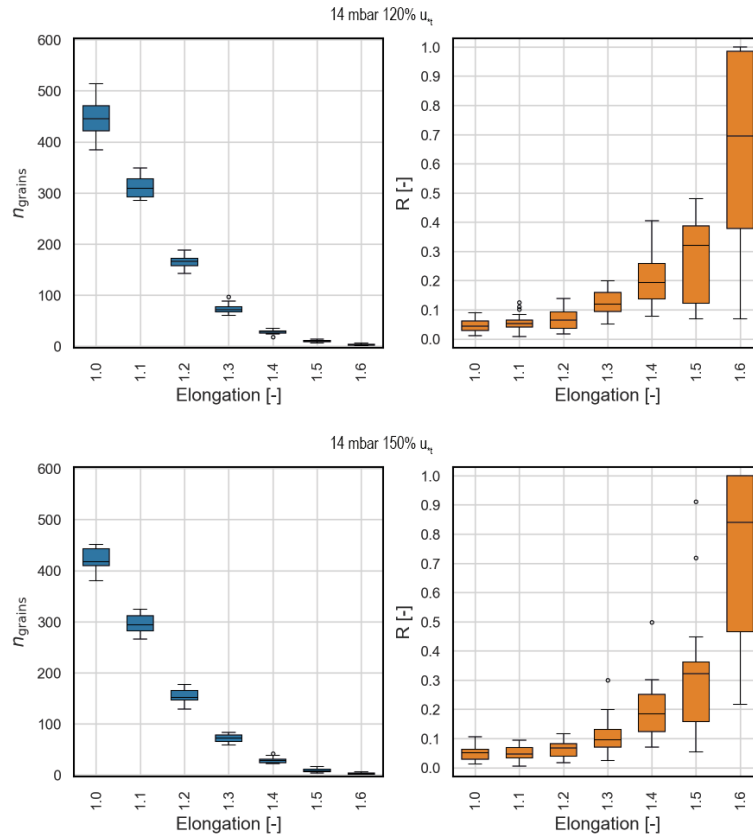


Figure F.4: Box plots of the number of grains and fabric strength for each lower limit on grain elongation for the experiments at 14 mbar.